Designing and testing the high-purity germanium gamma-ray spectrometer for the Dragonfly mission to Titan

by

Nathan Robert Hines

B.S., Kansas State University, 2016

AN ABSTRACT OF A DISSERTATION

submitted in partial fulfillment of the
requirements for the degree

DOCTOR OF PHILOSOPHY

Alan Levin Department of Mechanical and Nuclear Engineering
Carl R. Ice College of Engineering

KANSAS STATE UNIVERSITY
Manhattan, Kansas

2022

Abstract

The Dragonfly Mission will send a high-purity germanium gamma-ray spectrometer one billion miles from Earth to investigate the composition of the icy world Titan, Saturn's largest moon. The detector will be mounted on an autonomous rotorcraft and will travel over 100 miles across Titan's 94 K surface. A deuterium-tritium neutron generator will interrogate Titan's surface, producing gamma rays through neutron capture and inelastic scatter interactions. The gamma-ray spectrometer will measure these gamma-rays to determine the elemental composition of Titan's surface. The spectrometer was designed to operate in this unique environment, and was subjected to multiple tests to ensure design viability. The system was shown to be operable after being subjected to rocket-launch like vibration loads. A model was developed to simulate detector thermal performance and was shown to be accurate by comparison to experimental data. The model predicts that the detector will passively cool to an operating temperature of 100 K within seven days of the detector arriving on Titan's surface, meeting mission requirements. The ability to anneal, or heat, the germanium crystal to repair radiation damage under Titan-like thermal conditions was demonstrated. Annealing the detector for a low input power requires that vacuum be maintained inside the cryostat. Vacuum performance was thoroughly characterized, and long-duration vacuum maintenance was demonstrated using a non-evaporable getter. Additionally, sensitivity to neutron-induced gamma rays was demonstrated under Titan-like conditions. A radiation damage study was performed to investigate 1) the effects of neutron damage on germanium energy resolution and 2) the anneal time required to repair neutron damage. A correlation between neutron fluence and spectrometer energy resolution is presented and an anneal recipe is provided.

Designing and testing the high-purity germanium gamma-ray spectrometer for the Dragonfly mission to Titan

by

Nathan Robert Hines

B.S., Kansas State University, 2016

A DISSERTATION

submitted in partial fulfillment of the
requirements for the degree

DOCTOR OF PHILOSOPHY

Alan Levin Department of Mechanical and Nuclear Engineering
Carl R. Ice College of Engineering

KANSAS STATE UNIVERSITY
Manhattan, Kansas

2022

Approved by:

Major Professor
Walter McNeil

Copyright

Abstract

The Dragonfly Mission will send a high-purity germanium gamma-ray spectrometer one billion miles from Earth to investigate the composition of the icy world Titan, Saturn's largest moon. The detector will be mounted on an autonomous rotorcraft and will travel over 100 miles across Titan's 94 K surface. A deuterium-tritium neutron generator will interrogate Titan's surface, producing gamma rays through neutron capture and inelastic scatter interactions. The gamma-ray spectrometer will measure these gamma-rays to determine the elemental composition of Titan's surface. The spectrometer was designed to operate in this unique environment, and was subjected to multiple tests to ensure design viability. The system was shown to be operable after being subjected to rocket-launch like vibration loads. A model was developed to simulate detector thermal performance and was shown to be accurate by comparison to experimental data. The model predicts that the detector will passively cool to an operating temperature of 100 K within seven days of the detector arriving on Titan's surface, meeting mission requirements. The ability to anneal, or heat, the germanium crystal to repair radiation damage under Titan-like thermal conditions was demonstrated. Annealing the detector for a low input power requires that vacuum be maintained inside the cryostat. Vacuum performance was thoroughly characterized, and long-duration vacuum maintenance was demonstrated using a non-evaporable getter. Additionally, sensitivity to neutron-induced gamma rays was demonstrated under Titan-like conditions. A radiation damage study was performed to investigate 1) the effects of neutron damage on germanium energy resolution and 2) the anneal time required to repair neutron damage. A correlation between neutron fluence and spectrometer energy resolution is presented and an anneal recipe is provided.

Table of Contents

List of Figures

List of Tables

Chapter 1

Introduction

This work discusses development, design, and testing of a high-purity germanium (HPGe) gamma-ray spectrometer (GRS) for the Dragonfly space mission to Titan, Saturn's largest moon. Located roughly one billion miles from Earth, Titan is an icy world covered with a nitrogen and hydrocarbon rich atmosphere that is 4.4 times denser than that of Earth's.[14] Its 94 K surface is suspected to be covered with organic compounds, liquid hydrocarbon lakes, and water-ice rocks, as shown in Figure 1.1. A liquid-water ocean is suspected to be located beneath Titan's crust, which could interact with Titan's surface through cryovolcanism, creating the potential for liquid water to interact with Titan's organic-rich surface.[3] The Dragonfly mission is led by Johns Hopkins University Applied Physics Laboratory (APL) and is scheduled to launch in 2027. The spacecraft will travel approximately 7 years before reaching Titan in 2034. Upon reaching Titan, a $\sim$400 kg robotic rotorcraft will be deployed onto the moon. The rotorcraft will be powered by a multi-mission radioisotope thermal electric generator (MMRTG) and will contain an extensive scientific payload, including a mass spectrometer (DraMS), gamma-ray and neutron spectrometer (DraGNS), meteorology and geophysics instrumentation (DraGMet), and camera suite (DragonCam).[3] The Dragonfly rotorcraft will land in the Shangri-La sand dune region of Titan, shown in Figure 1.2. It will then travel more than 100 miles to the Selk impact crater through multiple short-distance

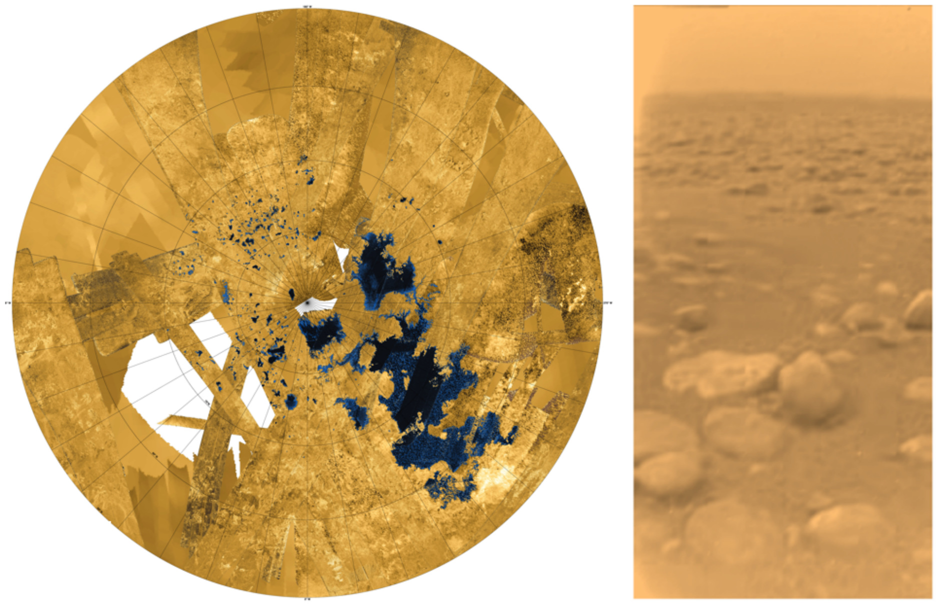

Figure 1.1: *Titan Surface Conditions.* ***Left***[1]*: Radar measurements from the Cassini mission indicate that liquid hydrocarbon lakes are present near the moon's poles.* ***Right***[2]*: A picture of Titan's surface was collected by the Huygens Probe, part of the Cassini mission. The rock-like objects shown here are approximately 10 cm across and are suspected to be water ice.*[3]

flights. The rotorcraft will spend most of the ∼3 year mission on the ground performing measurements or communicating data to Earth. It will relocate to new locations every 32 days, with flight times expected to be 30 minutes.[3]

One of the science questions that will be addressed by the Dragonfly mission is: "What chemical components and energy producing chemical pathways exist on Titan that could drive prebiotic chemistry?".[3] From this question the science requirement of measuring elemental abundances of C, N, O, H, Na, Mg, P, S, Cl, and K was created. The DraGNS instrument will utilize a deuterium-tritium (DT) neutron generator to interrogate Titan's surface with 14.1 MeV neutrons.[15] Neutron interactions with elements on Titan's surface will generate gamma rays through neutron capture and inelastic scatter interactions. These gamma-rays have energies characteristic of the element from which they were emitted. Some of these gamma-rays will travel to and be measured by the GRS, allowing for the elemental composition of Titan's surface to be determined. Table 1.1 lists some of the gamma-rays

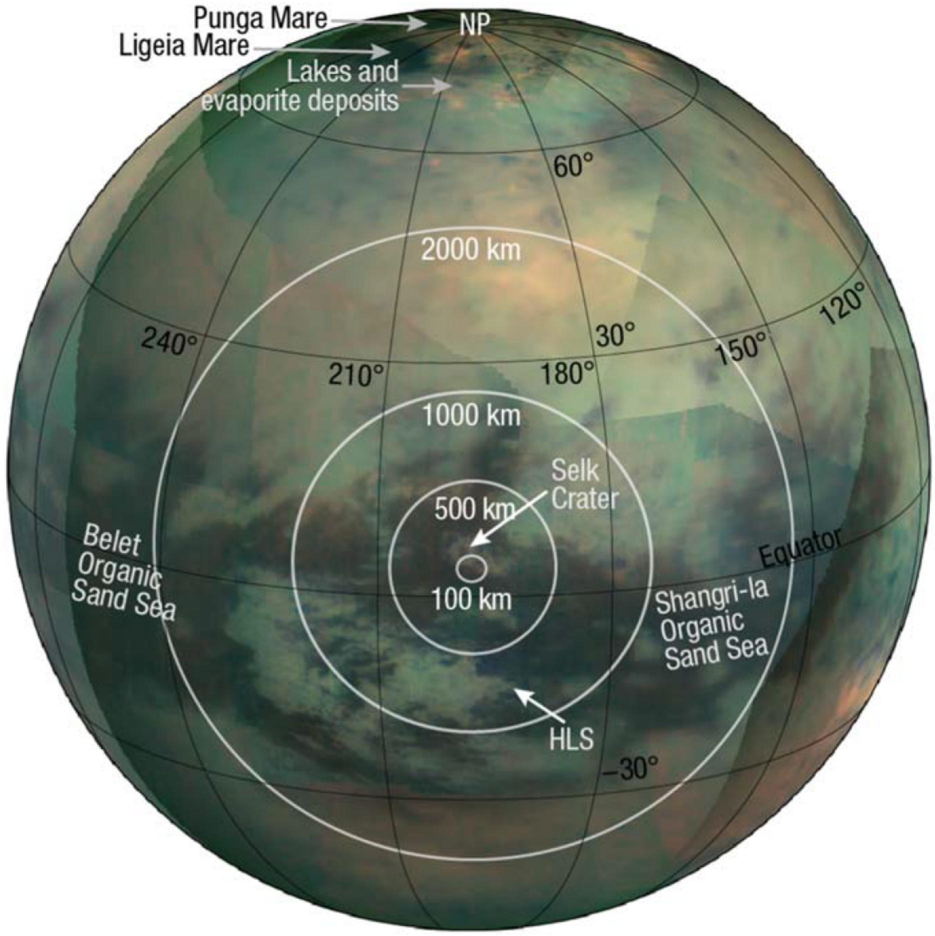

Figure 1.2: *Titan map.*[3] *The Dragonfly rotorcraft is intended to land in Titan's Shangri-La sand dunes. It will then make fly to the Selk Crater, stopping every few kilometers to perform measurements and recharge batteries.*

targeted for measurement by the GRS.

A HPGe GRS was chosen for this mission due to its excellent energy resolution performance. Energy resolution indicates statistical spread in gamma-ray energy measurements, and is specified by the metric Full Width at Half Maximum (FWHM) or the ratio of FWHM to the gamma-ray energy (reported as a percent value). Lower energy resolution is better for gamma-ray spectroscopy, as it reduces overlaps between gamma-ray measurements. It also reduces uncertainty in the number of gamma rays detected. As shown in Figure 1.3, individual gamma-ray peaks typically sit atop a continuum. Determining the number of gamma-rays events that fall within a peak requires that the continuum, or background, con-

Element	Gamma-ray Energy [keV]	Interaction
Carbon	4438 +/- 2[16]	Inelastic Scatter
Nitrogen	2313 +/- 0.3[16]	Inelastic Scatter
Oxygen	6129 +/- 0.4[16]	Inelastic Scatter
Hydrogen	2223.25[17]	Neutron Capture
Sodium	440 +/- 0.2[16]	Inelastic Scatter
Magnesium	1368 +/- 0.1[16]	Inelastic Scatter
Phosphorous	1266 +/- 0.1[16]	Inelastic Scatter
Sulphur	2230 +/- 0.1[16]	Inelastic Scatter
Chlorine	6110.842 +/- 0.020[17]	Neutron Capture
Potassium	1460.822 +/- 0.006[18]	Natural Background

Table 1.1: *Elements and their Characteristic Gamma Rays*

tribution be subtracted from the total peak area. Since background events are subject to statistical fluctuation, larger FWHM values correspond to larger uncertainties.

Germanium detectors can provide 0.2% or better energy resolution[19], while scintillator gamma-ray detectors, the primary alternative to HPGe detectors, have more than an order of magnitude poorer energy resolution.[4] This can make peak separation more difficult or impossible, as is illustrated by Figure 1.3.

The cost of the excellent energy resolution HPGe detectors provide is design complexity. They require cooling to ~100 K to minimize thermal electron-hole pair excitation and are typically operated in vacuum to keep the crystal surface free of contamination and to maintain thermal isolation between the germanium crystal and ambient conditions.[20] Thermally-generated electron-hole pairs and crystal surface contamination both increase charge noise and degrade energy resolution.[20]

Germanium GRSs have been successfully used in Earth[21;22] and solar[23] orbit, and explored Earth's moon[24], Mars[25;26], and Mercury[27]. Upcoming missions using HPGe detectors include Psyche[28], which is scheduled to launch in 2022 and will visit an asteroid located in the asteroid belt, and MMX[29], which will visit Mars' moons and has a planned launch date of 2024. The unique nature of the Dragonfly mission requires that a customized HPGe detector be used. The Dragonfly detector will be sent farther from Earth than any previous HPGe GRS and be the first HPGe detector to be inserted into a non-Earth planetary body with

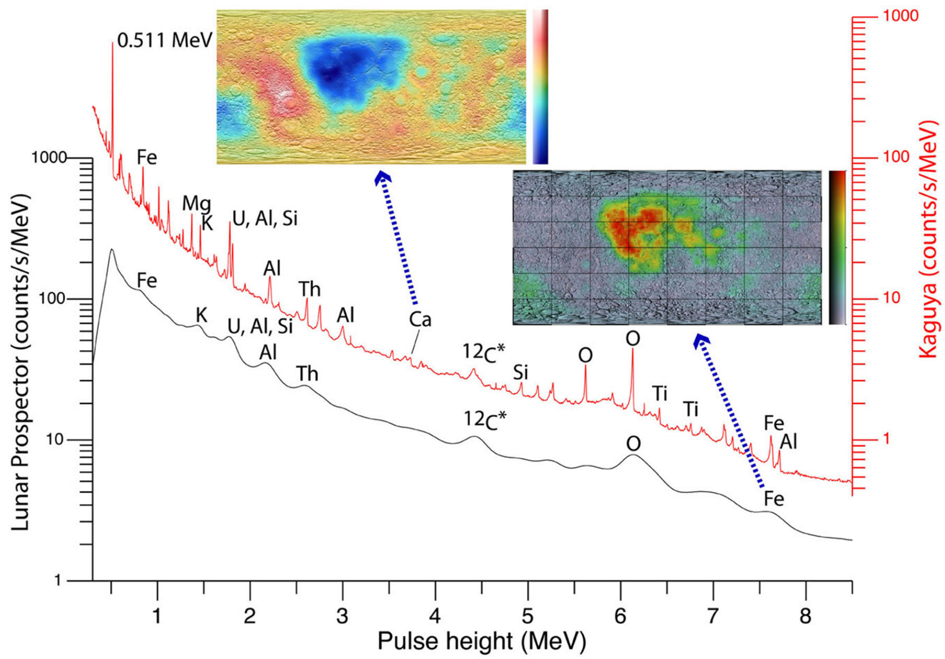

Figure 1.3: *HPGe and scintillator spectroscopic performance comparison.*[4] *The benefits of superior resolution are illustrated by comparing the gamma-ray spectra measured by the scintillator GRS onboard the Lunar Prospector*[5] *and the HPGe GRS onboard SELENE.*[6] *Note that some elements, such as silicon, are not visible in scintillator spectrum, but are apparent in the HPGe spectrum.*

an atmosphere.

Previous space HPGe GRSs cooled to operating temperature through mechanical cooling, radiative cooling to space, or solid cryogen cooling. However, the Dragonfly GRS will take the novel approach of convectively cooling to operating temperature using Titan's cold surface conditions. Another deviation from past missions is the mechanism for gamma-ray production. Previous space detectors utilized cosmic ray interactions with planetary bodies for gamma-ray production. However, Titan's thick atmosphere significantly attenuates these particles, preventing significant gamma-ray generation on its surface.[14;15;30] Dragonfly will instead utilize a DT neutron generator to interrogate Titan's surface with 14.1 MeV neutrons, which then excite gamma rays.

The Dragonfly GRS will be exposed to a damaging radiation environment over the course of the mission. During cruise it will be exposed to high-energy galactic cosmic rays and solar energetic particles[7] and high-energy neutrons from the MMRTG. After arriving on Titan's surface it will incur neutron radiation damage from both the MMRTG and DT neutron generator. Since HPGe detector energy resolution is significantly degraded when exposed to high-energy particles[20], the Dragonfly GRS is designed to be capable of heating the HPGe crystal to repair radiation damage. This process, referred to as annealing, will occur at the end of cruise and possibly during surface operations.

This work will discuss design and testing of the Dragonfly GRS Development Model, henceforth referred to as the "DM". The goal of the DM is to show that the GRS can meet operational requirements in a laboratory setting, and to inform design changes that will be integrated into subsequent GRS design iterations. This system will be shown to meet the following requirements:

1. Rocket-launch compatibility: The Dragonfly GRS must be able to survive the violent forces associated with rocket launch. This work will show that the DM remains operable and experienced no resolution degradation after being subjected 35 g and random vibration loads representative of rocket-launch.

2. Passive cooling and annealing on Titan's surface: Current mission plans are for the Dragonfly GRS to passively cool to an operating temperature of 100 K and perform a gamma-ray measurement within 1 Titan day (15.95 Earth days) of being deployed on Titan's surface. The GRS also must be able to heat the HPGe crystal to 378 K to repair radiation damage with input power of ∼5 Watts or less. A thermal model was developed to predict DM thermal performance on Titan, then benchmarked with measured data. The model indicates the system meets these both the passive cooling and anneal requirement.

3. Gamma-ray measurement: The DM must be able to measure gamma-rays from natural decay of radionuclides and from neutron interactions with elements on Titan's surface. The instrument is specified to provide 4.2 keV or better energy resolution for 1333 keV gamma rays. This work will show that the DM is sensitive to these gamma rays and

meets resolution requirements while operating in a Titan-like thermal environment.

Chapter 2

Background

The Dragonfly mission will utilize a HPGe GRS to measure the surface composition of Titan. HPGe technology has been successfully used in terrestrial and space applications for decades. However, use of a HPGe GRS on Titan will require novel detector design, as the journey to and operation on the icy world poses unique challenges. This chapter will discuss HPGe GRS operation principles and discuss Dragonfly GRS design.

2.1 HPGe Gamma-ray Spectrometer Overview

Germanium detectors utilize the properties of a p-n junction to detect ionizing radiation. HPGe detectors are fabricated from extremely pure germanium, typically with an impurity density of the order $\sim 10^{10}$ cm^{-3}. One side of the crystal is implanted with a electron accepting p-type material (boron) and electron donating n-type material (lithium) is drifted into the other. Diffusion occurs, in which electrons and holes migrate into the p and n-type regions, respectively. A net charge imbalance forms in the volume between the contacts and an electric field forms in this region. The electric field builds in strength until it offsets net charge carrier diffusion across the p-n junction. The region over which the electric field extends, called the depletion region, is highly resistive because it is depleted of charge carriers. Voltage bias, typically 1-4 kV, is placed across the crystal by holding the n-contact at a positive voltage with respect to the p-contact. This increases the strength of the electric field and grows the extent of the depletion region.

Gamma-rays interact with electrons in the depleted germanium through the photoelectric effect, Compton scattering, and pair production. The resulting energized electrons transfer energy to other electrons in the material, causing many electron-hole pairs to form. The electric field sweeps electrons and holes to the n and p-contacts, respectively, in a fraction of a microsecond for a Dragonfly-size HPGe detector. The motion of these charge carriers induces a charge response on the crystal contacts that is measured and amplified with very sensitive electronics. This induced charge is proportional to the gamma-ray energy deposited into the detector, which allows gamma-ray energy to be determined. Section 2.3 further discusses signal generation in HPGe detectors.

HPGe detector energy resolution performance can be degraded by charge trapping, a process by which impurity atoms introduce energy levels within germanium's forbidden gap, or the region between its conduction and valence bands.[20] These impurities can trap charge carriers before they complete their journey to the crystal contacts, causing variation in induced charge. In addition to impurities, structural defects can cause charge trapping.[20] One example is germanium lattice damage from high-energy particles. The Dragonfly HPGe crystals are specified to very pure to mitigate charge trapping from impurities, but charge trapping due to radiation damage is expected. This will be discussed in Section 2.3.

Electron-hole pair formation requires approximately 2.96 eV of energy deposition.[31] Hence, $\sim 3.4 \times 10^5$ charge carriers are generated per 1 MeV energy deposited by gamma-rays. This is over an order of magnitude more charge carriers than are produced by a similar energy deposition in high-performing scintillation detectors. This difference motivates the use of HPGe detectors in applications that require precise gamma-ray spectroscopy, as statistical variation in charge carrier production (proportional to the square-root of the number of charge carriers produced) limits energy resolution.

HPGe detectors have strict operational requirements that require careful design. Germa-

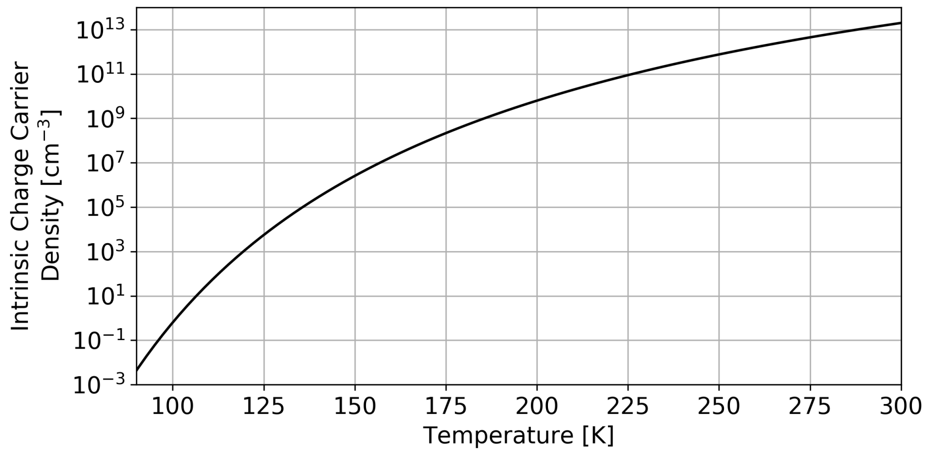

Figure 2.1: *Intrinsic germanium charge carrier density versus temperature. Charge carrier concentration increases exponentially with temperature. This prevents gamma-ray detection at room-temperature operation, as the number of charge carriers produced by MeV-energy gamma-rays (~10^5) are greatly outnumbered by those produced by thermally excitation.*

nium's bandgap, approximately 0.7 eV, prevents room-temperature operation, as thermal energy imparted electrons can excite them to the conduction band.[31] A corresponding hole is also left in the valence band. These thermally-excited charge carriers are swept to the crystal contact by the electric field placed across the crystal in a similar manner to charge carriers excited by radiation interactions.

Charge carrier density in intrinsic germanium can be estimated by Equation 2.1.[20]

$$N_i = C * T^{1.5} * e^{\frac{-E_g}{2*k_b*T}} \tag{2.1}$$

where N_i is the charge carrier concentration in intrinsic (pure) germanium, C is a material constant, T is absolute temperature, E_g is the bandgap for germanium, and k_b is the Boltzmann constant. Figure 2.1 shows intrinsic charge carrier concentration between 77 and 300 K. If a HPGe detector is operated at too high of a temperature, the number of thermally-excited charge carriers will greatly outnumber those generated by energy deposited from radiation. Random fluctuation in current flow between the n and p contacts due to thermally-generated charge carriers (leakage current) decreases detector sensitivity to radiation. Hence, leakage current must be minimized. Commercially-available germanium detectors are cooled by liquid nitrogen or utilize mechanical cryocoolers to cool the crystal to ∼120 K or less.[20;32]

HPGe detectors are typically housed in vacuum for two reasons. First, vacuum-isolation limits thermal conduction between cold crystal from ambient conditions, which reduces the amount of liquid nitrogen or cryocooler power needed to cool the system.[33] This is critical to portable systems, as they need to operate in situations in which liquid nitrogen is not readily available or utilize batteries to power their cryocoolers.

Second, crystals must be kept extremely clean to maintain resolution performance. Very small amounts of contamination on the crystal surface can cause surface current flow between the n and p contacts, contributing to leakage current.[20] Similar to thermally-generated electron-hole pairs, current from contamination can significantly degrade HPGe signal-to-noise performance. Housing the crystal under vacuum prevents gas molecules from condensing on the crystal's surface and degrading energy resolution.

While HPGe crystals are designed to have an extremely low impurity level, some impurities do remain. These impurities can make the bulk crystal slightly n or p-type. The Dragonfly GRS will utilize a n-type coaxial HPGe detector. Coaxial HPGe detectors make of n-type Ge have the n-contact in the inner well and the p-contact on the outer crystal surfaces. P-type crystals have the opposite configuration.

The n and p contacts must be electrically isolated to prevent surface current flow. This is done by ensuring that there is a region of intrinsic, high-resistivity Ge between the contacts. This region is sensitive to surface contamination, as gases can condense on this gap region and cause surface leakage current.

The Dragonfly GRS will utilize a n-type, coaxial detector with a blind well, as shown in Figure 2.2. It is rated to have 20% relative efficiency for detection of 1333 keV gamma-rays and its diameter and length are both 5 cm. Relative efficiency is frequently used for specifying the ability of HPGe detectors to measure gamma-rays. It refers to the ratio of the number of 1333 keV gamma-ray detections measured by a HPGe detector to that of a Ø7.62 cm x

7.62 cm cylindrical NaI(Tl) scintillator detector when source-detector distance is 25 cm.[20]

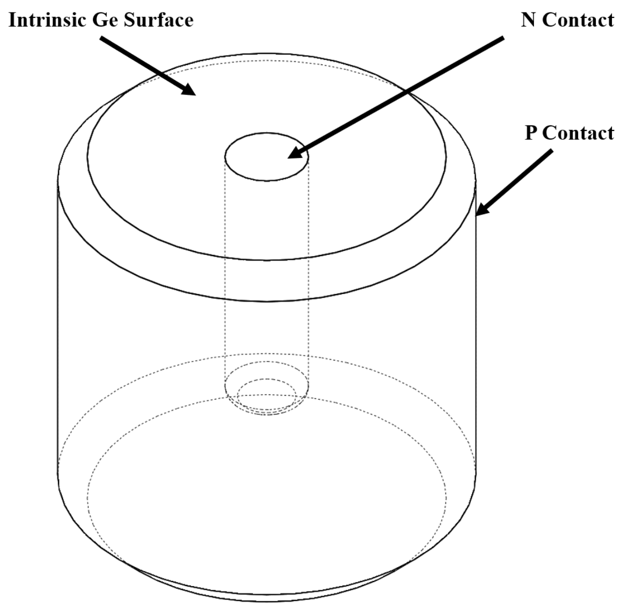

Figure 2.2: *The Dragonfly coaxial HPGe detector. The Dragonfly GRS will utilize a 20% relative efficiency, coaxial, n-type HPGe crystal. The n contact is constructed in the bore hole and the p contact is applied to the outer walls. Highly-resistive, intrinsic germanium separates the two contacts.*

The Dragonfly GRS will measure gamma rays produced through neutron interactions with Titan's surface. Neutrons can interact with elements through multiple processes, including elastic scattering, inelastic scattering, neutron capture, and fission interactions.[31] The probability of a neutron interacting with a material is quantified by the reaction cross section. The GRS will measure gamma rays produced by inelastic scatter and neutron capture interactions to identify elements that comprise Titan's surface. The Dragonfly DT neutron generator will generate 14.1 MeV neutrons at a rate of 10^8 s^{-1} that will interrogate Titan's surface within ~2 m of the Dragonfly rotorcraft.[3] The rate at which gamma-rays are produced from inelastic neutrons interacting with a material is a function of neutron flux, neutron energy, material volume, number density of target atoms, and the cross-section for the interaction, as shown Equation 2.2

$$R = V * N * \phi(E) * \sigma(E) \tag{2.2}$$

where R is the interaction rate, V is the volume of material, N is the number density of atoms, ϕ is the energy-dependent neutron flux, and σ is the energy-dependent neutron interaction cross section.

Equation 2.2 can be used to approximate the number of 440 keV inelastic gamma rays produced by a uniform flux of neutrons incident upon a thin, 1 cm^3 NaCl target. Assuming a 10^6 $[cm^{-2} * s^{-1}]$ monoenergetic flux of 14 MeV neutrons, the sodium inelastic scatter cross section for 440 keV gamma-ray produciton is approximately $4.63{\times}10^{-25}$ cm^2.[34] The number density of sodium in NaCl is $1.1{\times}10^{22}$ cm^{-3}. Hence, approximately 10^4, 440 keV gamma-rays would be produced per second.

The above calculation assumes that the target is thin, which implies that the target thickness is much shorter that the 14.1 MeV neutron mean free path. This allows one to estimate that each neutron interacts only once with the target. Calculating gamma ray generation from neutron interrogation of Titan is more difficult, as neutrons may interact multiple times with Titan's surface. As indicated in Equation 2.2, cross sections are dependent on neutron energy. This is especially true for neutron capture interactions, as neutrons must thermalize by loosing kinetic energy through other interactions (downscattering) prior to neutron capture occurring. While monoenergetic neutrons are emitted from the DT neutron generator, some neutrons will inevitably downscatter through interactions with Titan's surface. This both reduces their energy and changes the cross section for subsequent interactions. Neutron transport simulations using Monte Carlo methods offer a way to estimate gamma-ray production on Titan's surface. Simulation can also estimate the number of gamma-rays that arrive at and interact with the Dragonfly GRS. APL is developing a GEANT4 model to simulate neutron transport and gamma-ray interactions with the GRS. Simulation development is ongoing, but current estimates indicate that $\sim 10^4$ gamma-rays will interact with the GRS every second when the neutron generator is active.

2.2 Dragonfly Gamma-Ray Spectrometer Design

The Dragonfly HPGe crystal is encapsulated in a vacuum-evacuated aluminum canister. An encapsulated-crystal design was chosen to protect the crystal from gasses present during Earth-based testing and during operation on Titan's surface. The encapsulated crystal was provided by Mirion Technologies, Inc. and is based off encapsulated Ge detectors used for the EUROBALL cluster detector[35] and the Advanced Gamma Tracking Array (AGATA).[36] These encapsulated detectors were developed to increase the reliability of large HPGe detector assemblies, which were subject to failure due to condensable gasses collecting on crystal intrinsic surfaces. Housing individual HPGe detectors in vacuum-tight containers mitigated this issue.[37]

Vacuum inside the encapsulation is maintained with a non-evaporable getter (NEG) that is activated during assembly. The crystal is held rigidly inside the encapsulation to prevent the crystal from moving inside the encapsulation during rocket launch. The entire encapsulation has a mass of approximately 900 g. The crystal's outer, p-contact is electrically-connected to the encapsulation walls and held at ground potential. The n-contact inner-bore is connected to a high voltage feedthrough that is welded into the top of the encapsulation. The crystal encapsulation is also fitted with a temperature sensor and anneal heater.

The crystal encapsulation is suspended inside a custom outer cryostat via Kevlar, providing ruggedized, thermally-isolated containment for the crystal encapsulation. The Kevlar suspension system was inspired by previous space HPGe detectors (Psyche and MEGANE[33]) and utilizes multiple spring washers to maintain a constant preload on the encapsulation.

The cryostat has two conflat flanges attached to its lid. One houses a SAES D100 NEG that is used to maintain vacuum inside the cryostat. The other is used for attaching the DM to laboratory pumps. There are two electrical feedthroughs in the cryostat lid: one Teledyne-Reynolds Series 600 high-voltage connector[38] for supplying bias to and extracting signal from the crystal and one 9-pin Micro-D Metal (MDM) signal connector[39] for connecting to the temperature sensor and anneal heater. Figure 2.3 shows how the Ge crystal is integrated into the DM.

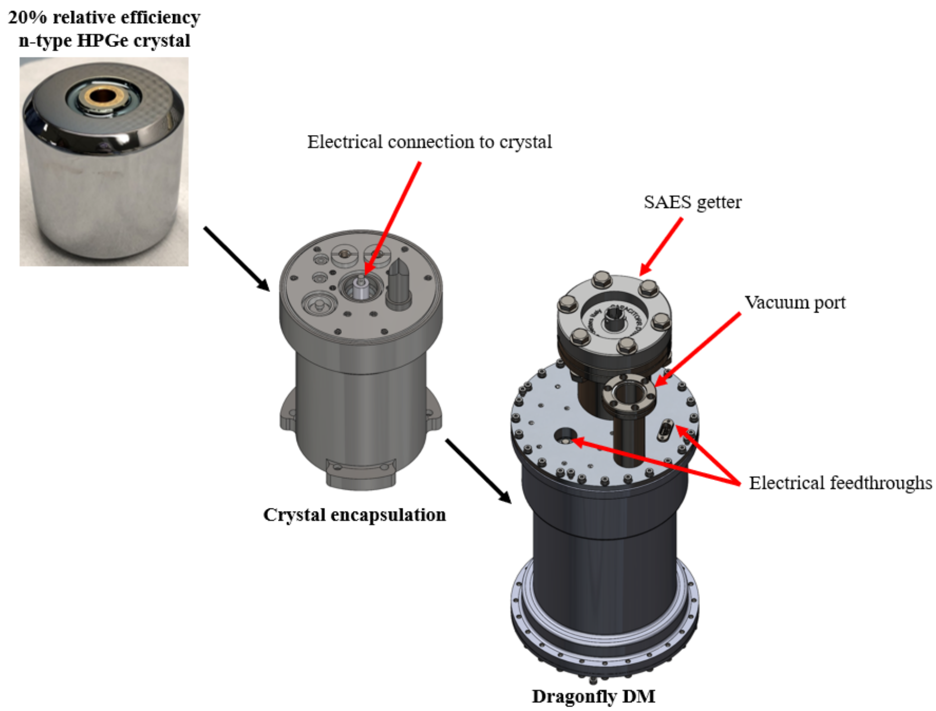

Figure 2.3: *The HPGe crystal is integrated into an aluminum encapsulation that is supplied by Mirion Technologies, Inc. The encapsulation is then installed into the DM cryostat.*

2.2.1 Rocket-launch Compatible Mechanical Design

The Dragonfly GRS must be compatible with vibration forces associated with rocket launch. The system was designed to survive 35 g vibration, a specification derived from Jet Propulsion Laboratory's (JPL) Mass Acceleration Curve (MAC).[40] This was achieved by packaging the crystal under force within its encapsulation and preloading the encapsulation within the cryostat.

2.2.1.1 Crystal Encapsulation

Although specific design details of the crystal encapsulation are proprietary to Mirion, Inc., the strategy for constraining crystal motion will be generally discussed. The encapsulation is designed to hold the crystal firmly and prevent relative motion when the system is subjected to rocket-launch forces. This is critical, as the fragile crystal can be easily damaged if allowed to interact with the encapsulation walls during vibration. Since vibration forces occur in all directions, a method was needed to preload the crystal along all axes. This was achieved by machining a 45° chamfer onto the crystals edges. Mounting jigs with matching chamfers were used on each end of the crystal. A 400-N preload was applied to one jig and a wave spring exerted a complementary force to the other. This method constrains crystal motion in the x, y, and z direction. Figure 2.4 shows the encapsulation preload method.

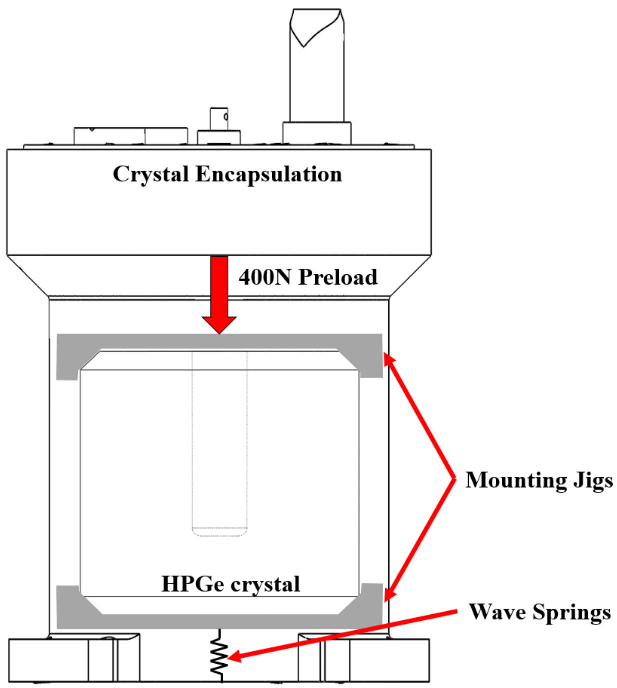

Figure 2.4: *Encapsulation preload. The Dragonfly GRS crystal has 45° chamfers that fit against mating mounting jigs. A 400 N preload is applied to one mounting jig and a spring washer (represented by a simple spring in this figure) applies an equal force to the other. This technique allows the crystal to be securely held within the encapsulation.*

2.2.1.2 Encapsulation Suspension

The crystal encapsulation needed to be mounted within the DM cryostat in a way that both constrained its motion during rocket launch and thermally-isolated it to facilitate low-power annealing. Meeting these two requirements was non-trivial, as many high-strength solutions result in a low-thermal resistance connection between the cryostat and encapsulation. While typical high-thermal resistance attachment techniques work well in laboratory environments, they are not suited for rocket launch.

The Dragonfly GRS utilizes a proprietary Kevlar suspension system to suspend the crystal encapsulation within the cryostat. The Kevlar suspension system is preloaded at 1150 N using 4 stainless steel wave springs.[41] This technique constrains encapsulation motion during vibration and thermally isolates the encapsulation. A similar method was used for previous LLNL-developed space GRSs used for the MESSENGER, Psyche, and MMX missions.[42–44]

2.2.2 Thermal Design for Passive Cooling and Annealing

The Dragonfly DM was designed to meet two thermal requirements:

1. Passive cooling to operational temperature within one Titan day after deployment on Titan's surface

2. Surface and cruise annealing for less than 5 Watts of input power

During cruise and prior to Entry, Descent, and Landing (EDL) operations, the GRS will be held at approximately 273 K using energy from the MMRTG. Once exposed to Titan's atmosphere, it will begin to convectively cool to Titan's surface temperature. Titan temperature was measured to be 94 K[14] at the Huygens Probe landing site, which is in close proximity to where the Dragonfly lander will operate, and diurnal temperature fluctuation is expected to be ± 1.5 K.[45] Passive cooling must allow the detector to cool to operational temperature ($\leq$100 K) within 16 days of landing to perform a planned gamma-ray measurement.

The annealing requirement involves heating the crystal encapsulation to 378 K[7] for many hours with $\leq$5 Watts of steady-state power input in two different scenarios: cruise and surface operations. The cruise anneal will repair radiation damage incurred during travel between Earth and Titan. Depending on the severity of radiation damage incurred during surface operations, another anneal may be required while the system is deployed on Titan. The GRS outer cryostat will be exposed to a 94 K, gaseous environment during surface operations (see Figure 2.5). The surface anneal case represents a worst-case scenario for anneal power due to the colder boundary condition. Hence, this scenario will be investigated in this work, as meeting this requirement indicates that the cruise anneal requirement is also met.

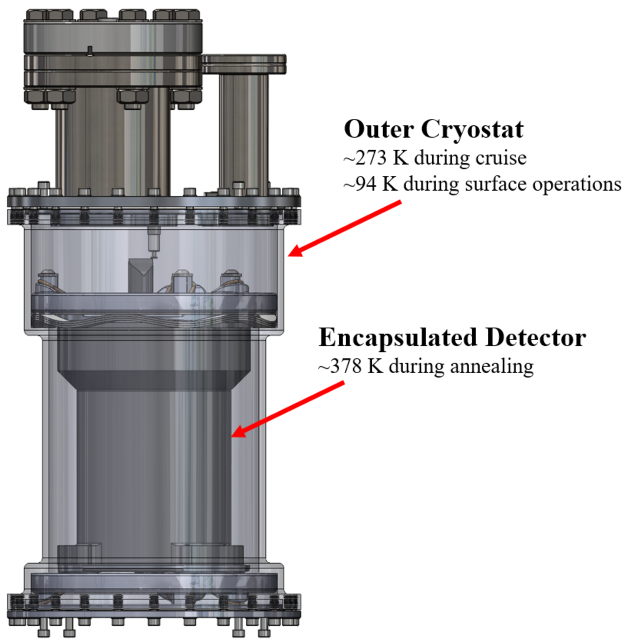

Figure 2.5: *Dragonfly DM annealing. The DM is designed to allow for the crystal to be annealed for less than 5 Watts of input power. Annealing will occur during cruise and surface operations, when the outer cryostat is held at 273 K and 94 K, respectively.*

Quick passive cooling and low-power annealing are conflicting requirements. Minimizing GRS cooling time is accomplished by increasing thermal conductance between Titan's atmosphere and the crystal. Conversely, anneal power is lowered by decreasing thermal conductance between the crystal and ambient conditions.

Understanding heat exchange between the GRS and Titan's environment is key to ensuring the system meets thermal requirements. Heat can be transferred via conduction, convection, and radiation. Conduction can occur through solid, liquid and gas media. Conduction between the crystal encapsulation and the outer cryostat includes contributions from signal wires and Kevlar cords and from gas molecules that are contained inside the cryostat.

Gaseous conduction between the crystal encapsulation and the cryostat can be reduced if the cryostat is vacuum evacuated, as is the case for the DM. If the internal gas is in the free molecular flow regime (i.e. molecular mean free path is larger than the gap between the encapsulation and the cryostat), thermal conduction is proportional to pressure.[13] Hence, reducing system pressure results in a linear decrease in gas conduction. The DM is designed to maintain internal pressure of $\leq 10^{-4}$ mbar, which will result in a negligible amount of heat transfer through the gas. This claim is discussed in Appendix B.6.

Convective heat transfer is caused by bulk movements of fluid that surrounds a surface. Convection is negligible for heat transfer between the crystal encapsulation and the cryostat due to the vacuum condition, but is critical for passively cooling the GRS on Titan's surface. Analysis is in progress to estimate a convective heat transfer coefficient for the Dragonfly mission. Since this study is ongoing at the time of this writing, subsequent thermal analysis will utilize an estimated Titan convective heat transfer coefficient published by Lorenz et al. using data from the Huygens Probe.[46] The heat transfer coefficient on Titan's surface was estimated to be between 1.4 and 4 $[W * m^{-2} * K^{-1}]$, hence an average value of 2.7 $[W * m^{-2} * K^{-1}]$ will be used for this work.

Radiative heat transfer occurs when photons are emitted from one surface and deposit energy on another. Radiative heat transfer between the DM and Titan's surface can be considered negligible in comparison to convection[46], but is a significant contributor to heat transfer between the crystal encapsulation and cryostat.

Heat transfer between the GRS and Titan's ambient can be modeled by an electrical analogy, where temperature, thermal resistance, and heat flow are represented similarly to voltage, resistance and current, respectively.[47] Figure 2.6 shows a simplified DM thermal model. Nodes represent component temperatures. The leftmost is Titan ambient, the middle is the cryostat, and the rightmost is the crystal encapsulation. The HPGe crystal is thermally connected to the crystal encapsulation with large-area metal contacts. Hence the two components are isothermal. Red arrows refer to heat that is injected into the system at various nodes. Heat power for annealing the crystal is represented by the rightmost arrow in Figure 2.6. This value will be zero during the cooldown and during typical operation on Titan's

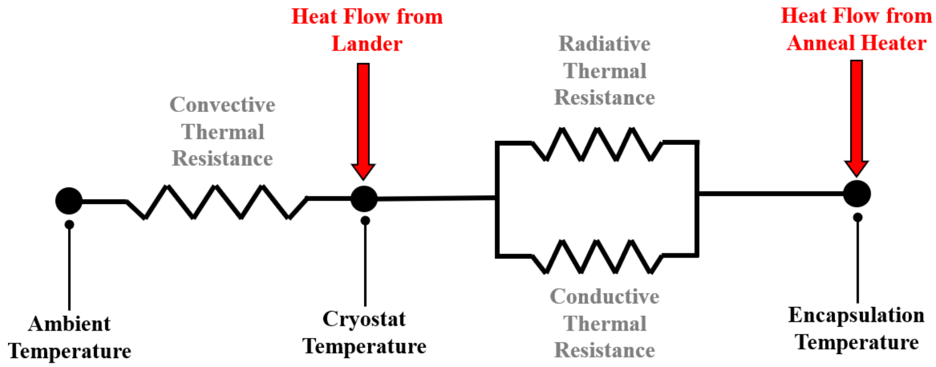

Figure 2.6: *Dragonfly DM thermal model. Nodes represent component temperatures, resistors indicate thermal resistances between components, and red arrows indicate heat being injected into the system.*

surface. It will be non zero only during GRS annealing.

The Dragonfly GRS will be attached to the lander by a bracket and a wiring harness, and some heat from inside the warm lander will be transmitted to the outer cryostat via these components. This heat flow, represented as the leftmost red arrow in Figure 2.6, has not yet been specified by mission planners because bracket and harness design have not been finalized. However, lander designers have estimated that the bracket will apply approximately 1 Watt of heat to the cryostat. This value will be used for calculations performed in this work.

Analysis of heat flow at the cryostat and crystal encapsulation allow for two coupled differential equations to be developed. Equations 2.3 and 2.4 represent heat flow at the crystal encapsulation and cryostat, respectively.

$$m_E c_E \frac{dT_E}{dt} = q_A - [\frac{T_E - T_C}{(R_{th,Rad}^{-1} + R_{th,Cond}^{-1})^{-1}}] \tag{2.3}$$

$$m_C c_C \frac{dT_C}{dt} = [\frac{T_E - T_C}{(R_{th,Rad}^{-1} + R_{th,Cond}^{-1})^{-1}} + q_L] - [\frac{T_C - T_{Amb}}{R_{th,Conv}}] \tag{2.4}$$

Table 2.1 overviews the variables used in Equations 2.3 and 2.4. Derivation of Equations 2.3 and 2.4 and calculations for the thermal resistances are shown in Appendix B.

Table 2.1: *Thermal Model Parameters*

Variable Name	Description
t	Time
T_{Amb}	Ambient temperature
T_C	Cryostat temperature
T_E	Crystal encapsulation temperature
$R_{th,Conv}$	Convective thermal resistance to Titan environment
$R_{th,Rad}$	Radiative thermal resistance
$R_{th,Cond}$	Conductive thermal resistance
q_L	Heat input from lander
q_A	Heat input from anneal heater
m_C	Cryostat mass
m_E	Encapsulation mass
c_C	Cryostat specific heat
c_E	Encapsulation specific heat

The thermal model allows for DM thermal performance on Titan to be simulated. However, it required benchmarking against experimental data to confirm it accurately captures DM heat transfer. An experiment is discussed in Section 3.2 in which the DM was passively-cooled in a Titan-like thermal environment. Data from this measurement were then used to validate the thermal model, allowing for prediction of thermal performance on Titan's surface.

2.2.3 Vacuum Design for Operation on Titan's Surface

The Dragonfly DM has two regions that are held under vacuum. The crystal encapsulation is vacuum evacuated and sealed during manufacturing. This keeps the crystal surface free of contaminants and prevents high voltage breakdown. This vacuum region does not thermally-isolate the crystal from the encapsulation, as the two are connected via soft metal contacts. The encapsulation is suspended inside the outer cryostat, which is also held at vacuum. The primary purpose of this vacuum stage is to thermally isolate the encapsulation from Titan conditions by preventing heat transfer via gas conduction.

Both regions utilize non-evaporable getters. This strategy was chosen because getters can collect gasses (i.e. maintain vacuum) without active power. This is a useful feature for space instrumentation, which typically have limited power budgets. Bulk getters are composed of chemically active materials that adsorb non-hydrogen molecules onto their surface. Eventually the getter surface will become saturated with collected gas molecules and the getter's effective pumping speed becomes negligible. Pumping performance can be restored by activation, or heating the getter material to several hundred degrees Celsius. This diffuses adsorbed gasses deep into the getter and enables surface adsorption to continue. Activation is required every time a getter is removed from vacuum or if the getter has reached its saturation capacity for any one gas. Hydrogen is captured through a bulk rather than a surface process, which allows for extremely high hydrogen pumping capacity.

It should be noted that getters are unable to capture some gasses, such as noble gasses. Additionally, the getter considered for the Dragonfly cryostat is unable to pump methane unless it is maintained at a temperature above 300°C[48], which is not practical for the Dragonfly mission. The inability to pump argon and methane is relevant for Dragonfly GRS, as the system will need to maintain vacuum on Earth ($\sim 1\%$ argon atmosphere[49]) and on Titan ($\sim 5\%$ methane atmosphere[14]). Hence, it is critical that the DM be leak tight.

2.2.3.1 Encapsulation Vacuum

The encapsulated crystal is held at vacuum to prevent volatile gasses from condensing on the germanium crystal surface and to avoid high-voltage discharges inside the encapsulation. The crystal encapsulation vacuum was designed, tested, and thoroughly characterized by Mirion Technologies, Inc. and SAES Group.[37] The basic method to maintain vacuum inside the crystal encapsulation is as follows: 1) Pump and bake encapsulation for many hours using laboratory pumps, 2) Activate getter, 3) Separate encapsulation from laboratory pumps via an aluminum pinch-off tube. Once separated from laboratory pumps, the portable crystal encapsulation maintains vacuum using only a model St 175 SAES non-evaporable getter.[50] Discussions with encapsulation developers indicate that it was designed to maintain a pressure below 10^{-4} mbar for 50 years[51], which is approximately five times longer than the Dragonfly mission duration. While characterization of the encapsulation getter is not considered in this work, the vacuum condition inside the encapsulation was monitored indirectly through GRS measurements. If the getter fails to maintain sufficient vacuum, energy resolution may degrade due to leakage current and/or high-voltage breakdown may occur. Both energy resolution and breakdown were monitored throughout DM development.

2.2.3.2 Cryostat Vacuum

The crystal encapsulation is suspended inside the cryostat. The region inside the cryostat and outside the crystal encapsulation is held at vacuum to ensure low-power annealing on Titan's surface. It should be noted that at the time of this writing a trade study is being performed to determine if a surface anneal will be required on Titan. If the results of this study indicate that a surface anneal is not necessary, future GRS iterations may not maintain a vacuum in the cryostat. However, this study will not conclude until after the DM is developed. Since vacuum design is a non-trivial task, it was decided that the DM be designed to have the cryostat vacuum evacuated. This allowed the design to mature throughout GRS development. If it is later determined that a surface anneal is not required, the outer vacuum region can be descoped with minimal impact to GRS development schedule. This work investigates use of SAES St 172[48] sintered getter material to maintain vacuum in the outer cryostat. An off-the-shelf option, SAES model D100[52], was chosen for several reasons:

- High Sorption Capacity: Sorption capacity refers to how much of a gas, typically indicated in units of mbar×liters, a getter can adsorb before requiring reactivation. This is a critical parameter, as it indicates how long the getter can maintain vacuum between activations.

- Ready-to-Use: The SAES getter is comprised of multiple sintered getter disks that are packaged into a stainless steel housing that is mounted onto a 2-3/4" Conflat (CF) flange. The D100 also includes integrated resistive heaters that are used for getter activation.[52] This packaged solution was ideal for GRS development as it could be integrated into the system with minimal customization. Future GRS versions can either utilize the D100, or repackage its disks to reduce size and mass.

- Off-Pump Activation: After activation, the getter will maintain vacuum until it absorbs sufficient gas to saturate its surface. It then requires reactivation to restore its ability to collect gas molecules. St-172 getters can be activated without being connected to laboratory pumps[48;53]. This is a good feature, as it allows the getter to be reactivated in cruise (without use of complicated valves for space venting) and on Titan's surface.

- Rocket Launch Compatibility: The D100 non-evaporable getter must be compatible with vibration loads associated with rocket launch. Past space GRSs have considered using a powdered SAES getter. However, first-hand experience indicates that this type of getter is incompatible with rocket launch, as the getter powder does not stay confined to packaging during vibration. Discussions with SAES and vibration testing conducted by for the PHEBUS instrument[54;55] indicate that sintered, St 172 getter material is well suited for space use.

Use of a getter does not guarantee that a system is able to maintain vacuum. Both gas load and gas type must be considered when determining if a getter is viable for vacuum maintenance.

Getters have finite pumping capacity, meaning they can pump only so many gas molecules before their pumping speed is diminished. Once pumping speed is negligible, the getter is considered saturated, and must be activated to restore pumping ability. Hence gas load, or the number of gas molecules entering a system due to leaks, permeation, and outgassing, directly affects how long a NEG can maintain vacuum between activations. The DM is designed for minimum gas load. Indium seals were chosen for the removable top and bottom flanges they have a low-leak rate, even at cryogenic temperatures.[56] Welded, ultra-high vacuum electrical feedthroughs were also chosen to minimize gas infiltration into the cryostat. Outgassing was minimized using the below techniques:

- Component Cleaning: Removing volatile material, such as machine oil and other organic compounds, from vacuum component surfaces is critical to reduce outgassing. All DM components were thoroughly cleaned prior to assembly. This procedure began with rinsing components with filtered distilled water, then ultasonic cleaning them with detergent. This was followed by a distilled water rinse and ultrasonic bath. The last cleaning step was to ultrasonically clean components in isopropanol.

- Handling: Components were always handled with gloves to reduce the chances of contamination by skin contact.

- Vacuum-baking. Once the DM was assembled, it was vacuum evacuated while being heated to 100°C for ∼1 week. This recipe was chosen to ensure the indium seals used to seal the cryostat would not fail, and was guided by previous publications that prepped components for ultra-high vacuum.[57] Vacuum baking served two purposes. First, it reduces total system outgassing. Second, in-situ vacuum baking changes the dominant gas species in a chamber. The primary gas type in a non-baked chamber that hasn't been pumped for a long time is water vapor.[57] However, the gas composition can be changed to approximately 90% H_2 and 10%: CO, CO_2, and CH_4 (in decreasing order) by a moderate-temperature vacuum baking cycle.[58] The getter investigated in this work has a large capacity for H_2, CO, CO_2, making vacuum-baking critical for the Dragonfly DM.

The types of gasses present inside a chamber are also critical to maintaining vacuum with a non-evaporable getter. The D100 getter used for the DM can pump the types and quantities of gasses listed in Table 2.2.[52] As noted earlier, the DM cryostat getter is unable to pump

Table 2.2: *SAES D100 Sorption Capacity*

Gas Type	Quantity captured per activation [mbar×liter]	Capture Method
CO	3.3×10^{-1}	Surface
CO_2	3.3×10^{-1}	Surface
O_2	2.7×10^{0}	Surface
H_2O	6.7×10^{0}	Surface
N_2	1.3×10^{-2}	Surface
H_2	1.8×10^{2}	Bulk

noble gasses and methane. These are of key interest to the Dragonfly Mission, as argon is present in Earth's atmosphere and Titan's atmosphere contains methane. Concerns over gas infiltration motivated the choice of indium seals and welded feedthroughs discussed earlier. DM gas load and type were characterized in this work. Additionally, ability to maintain vacuum using the D100 getter was investigated.

2.2.4 Readout Electronics

Dragonfly GRS amplifier development is being conducted by APL. Detailed discussion of amplifier design and testing is outside the scope of this work. However, a brief overview is provided as the DM will utilize an APL-developed amplifier to perform gamma-ray measurements discussed in Section 3.4.

Germanium gamma-ray detectors typically use charge-integrating amplifiers to measure charge induced by gamma-ray energy deposition. The amplifier contains a Junction Field Effect Transistor (JFET) and RC feedback loop that are typically mounted on or near the cryogenically-cooled detector to reduce thermal noise.[59] An operational amplifier (Op Amp), typically kept at room temperature, is connected to the JFET and feedback loop. These components integrate charge induced by gamma-ray energy deposition, and output a low-noise voltage signal that is shaped, amplified, and binned to produce gamma-ray spectra. Commercial systems typically position the JFET, feedback loop, and Op Amp close to the detector to reduce capacitance and pick-up noise.[60]

Dragonfly operating conditions pose a unique challenge to HPGe amplifier design. Since the GRS will be mounted outside the rotorcraft to facilitate passive cooling, it will be exposed to Titan's 94 K environment. Hence, it is difficult to both position the Op Amp close to the detector and keep it warm.

This work utilizes an prototype APL-developed charge-integrating amplifier. The JFET and feedback loop are mounted on the top flange of the DM and are connected to an Op Amp via ∼1-m long cables. This allows the Op Amp to be kept warm by positioning it inside the rotorcraft. It should be noted that at the time of this writing, internal lander temperature has not been specified. Current estimates indicate that locating the Op Amp inside the lander will allow it to be maintained at approximately 273 K. Figure 2.7 shows a simplified schematic of the amplifier used in this work.

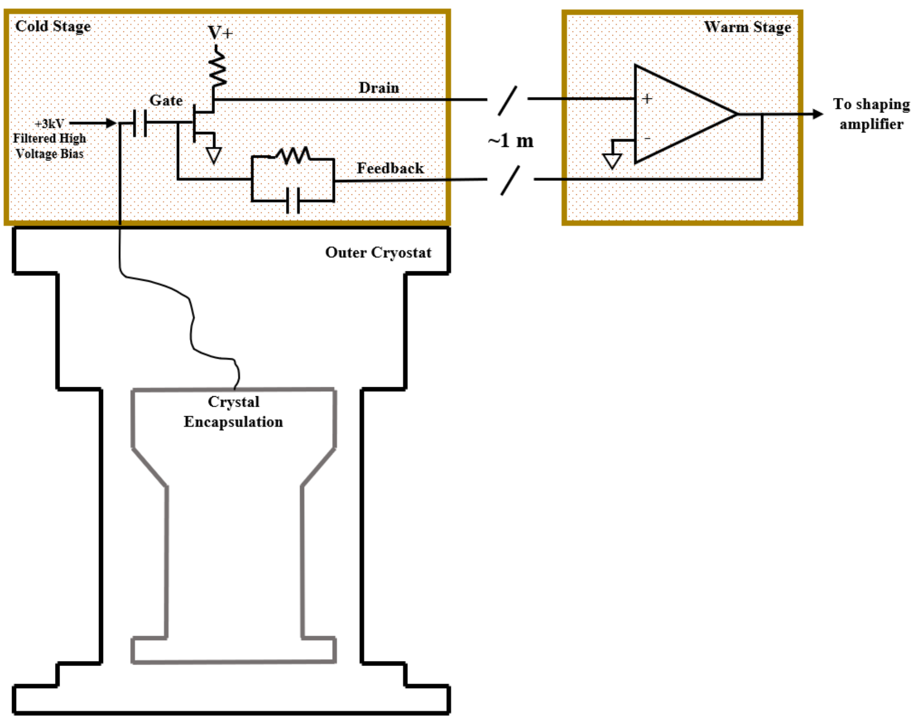

Figure 2.7: *Schematic of DM prototype amplifier. An APL-developed charge-sensitive amplifier was used in this work to perform gamma-ray spectroscopy with the DM. This custom amplifier separates cold components (JFET and feedback loop) from the warm Op Amp with ∼1 m long cables.*

One advantage of this design is that all preamplifier components are mounted outside the cryostat. External placement allows components, such as the JFET and coupling capacitor, to be replaced without breaching cryostat vacuum. Recall that prepping the cryostat vacuum after atmospheric exposure can take many days. Placing preamplifier components outside the cryostat is also beneficial for reducing system gas load. Even vacuum-rated insulators have orders of magnitude higher outgassing rates than metals.[57] This means that very small amounts of insulator material can significantly increase gas load. Additionally, electronics often require soldering, which is detrimental to vacuum quality. External preamplifier placement also minimizes the number of signal feedthroughs, which reduces leak rate. Hence, this design is ideal from a vacuum-maintenance perspective.

There are some concerns with this design. One issue is that the JFET source and drain cables are required to be long ($\sim$ 1 m), as they need to connect components located on the cryostat to components that are located inside the lander. This cable length is over an order of magnitude longer than previous space GRSs[33], which can increase noise pick up and sensitivity to microphonics. As of this writing, a trade study is underway at APL to finalize Dragonfly GRS preamplifier design.

2.3 HPGe Radiation Damage from MMRTG Neutrons

HPGe detectors are sensitive to radiation damage from high-energy particles, such as protons and neutrons. This work focuses on fast-neutron radiation damage, which results from neutrons imparting some of their energy to germanium atoms through elastic and inelastic neutron interactions.[61] The number of these interactions can be estimated by using Equation 2.2 with either the inelastic or the elastic cross sections for germanium. A portion of the energy transferred to the recoil Ge atom is available to create Frenkel defects in the germanium lattice.[62] Kraner et al. calculated that the average energy available to create lattice displacements from 5 MeV neutron interactions with germanium is 4.2×10^4 eV.[61] Since formation of a Ge lattice defect requires as little as $\sim$30 eV of energy, one neutron interaction could create many hundreds or even thousands of defects.[61;63] Similarly, energetic protons can also cause lattice defects in Ge. Lattice damage results in the production of acceptor sites in the bandgap structure that trap holes.[64] Hole trapping reduces charge collection efficiency and degrades energy resolution.

Recall from Section 2.1 that coaxial detectors made of n-type Ge have the n-contact on the inner well and the p-contact on the outer crystal surface. Since the n-contact is positively biased with respect to the p-contact, coaxial HPGe detectors made of n-type germanium collect holes on the outer contact and electrons in the inner well. This electrode configuration is referred to as "reverse electrode".[65] P-type coaxial HPGe detectors have an opposite, or "conventional electrode", configuration and collect holes and electrons on the inner well and outer crystal surface, respectively. Figure 2.8 shows the different configurations. By a volumetric argument, most interactions (and subsequent charge carrier generation) occur in the outer regions of a coaxial detector, and signal generation is dominated by charge carriers that travel to the inner well.[20;65] Therefore, electron collection dominates signal in reverse-electrode HPGe detectors and hole collection dominates signal in conventional-electrode HPGe detectors. This is illustrated in Figure 2.9. A reverse-electrode configured coaxial detector is shown and 3 gamma-ray interaction locations are identified. Resulting induced charge for each interaction location are also shown. Appendix A shows the method used to produce these pulse shapes.

Since radiation damage results in hole trapping and signal generation in reverse-electrode HPGe detectors is dominated by electrons rather than holes, it is logical to assume that reverse-electrode detectors would be more resilient to radiation damage than conventional-electrode detectors. Pehl et al. showed this experimentally by exposing two 7% relative efficiency coaxial HPGe detectors, one conventional and one reverse-electrode configured, to an unmoderated Cf-252 neutron source.[65] Energy resolution was measured intermittently, allowing for resolution degradation to be documented at several neutron fluences. This experiment indicated that reverse-electrode HPGe detectors experienced ∼28 times less res-

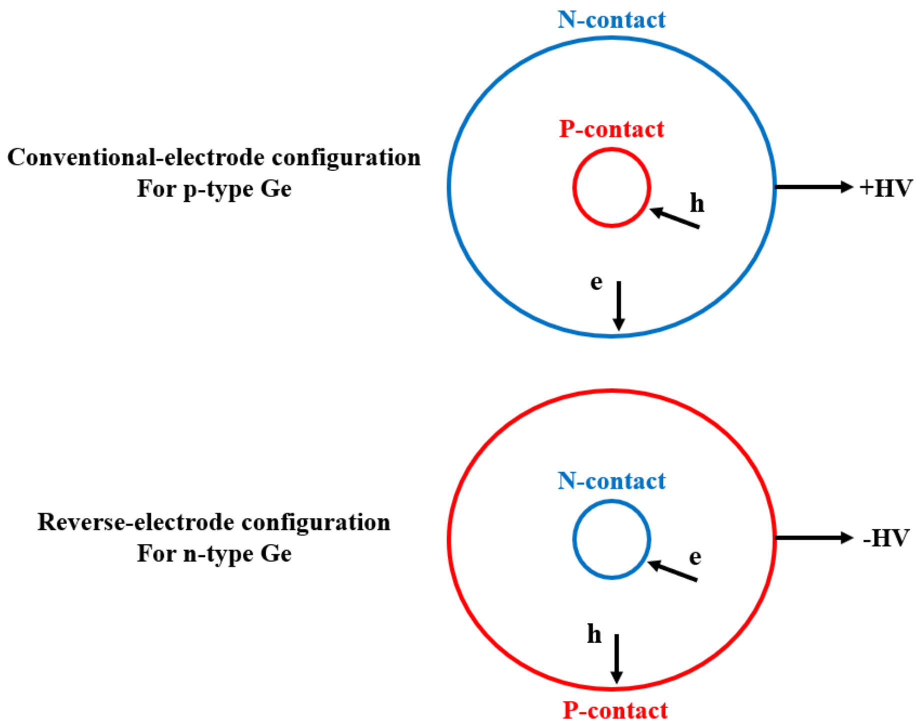

Figure 2.8: *HPGe coaxial crystal configurations. Coaxial detectors made with p-type Ge have the n contact on the outer crystal surface and p contact on the inner well. This is referred to as a conventional-electrode configuration and is shown in the top figure. N-type coaxial detectors have a reverse-electrode configuration, in which the n contact is on the inner well and the p contact is on the outer crystal surface, as shown in the bottom figure. Since the n contact is positively biased with respect to the p contact, coaxial detectors with conventional electrode configurations collect holes (indicated with the letter "h") on the inner contact and collect electrons (indicated with the letter "e") on the outer crystal surface. The opposite is true for detectors with reverse electrode configurations.*

olution degradation than p-type when exposed to the same neutron flux. This motivated the choice of a reverse-electrode coaxial detector for the Dragonfly mission, as it will experience significant radiation damage during its cruise to and operation on Titan.

The plots shown in Figure 2.9 correspond to a detector that exhibits no permanent charge trapping, as all of the charge is collected after ∼200 ns. This is not the case for HPGe detectors that are exposed to large fluences of fast neutrons. As mentioned earlier, radiation damage creates hole traps that can immobilize holes before they arrive at the p contact. Since the trapped hole is unable to complete its journey to the contact, it induces less charge than holes that do not experience trapping. This leads to spreading in gamma-ray energy

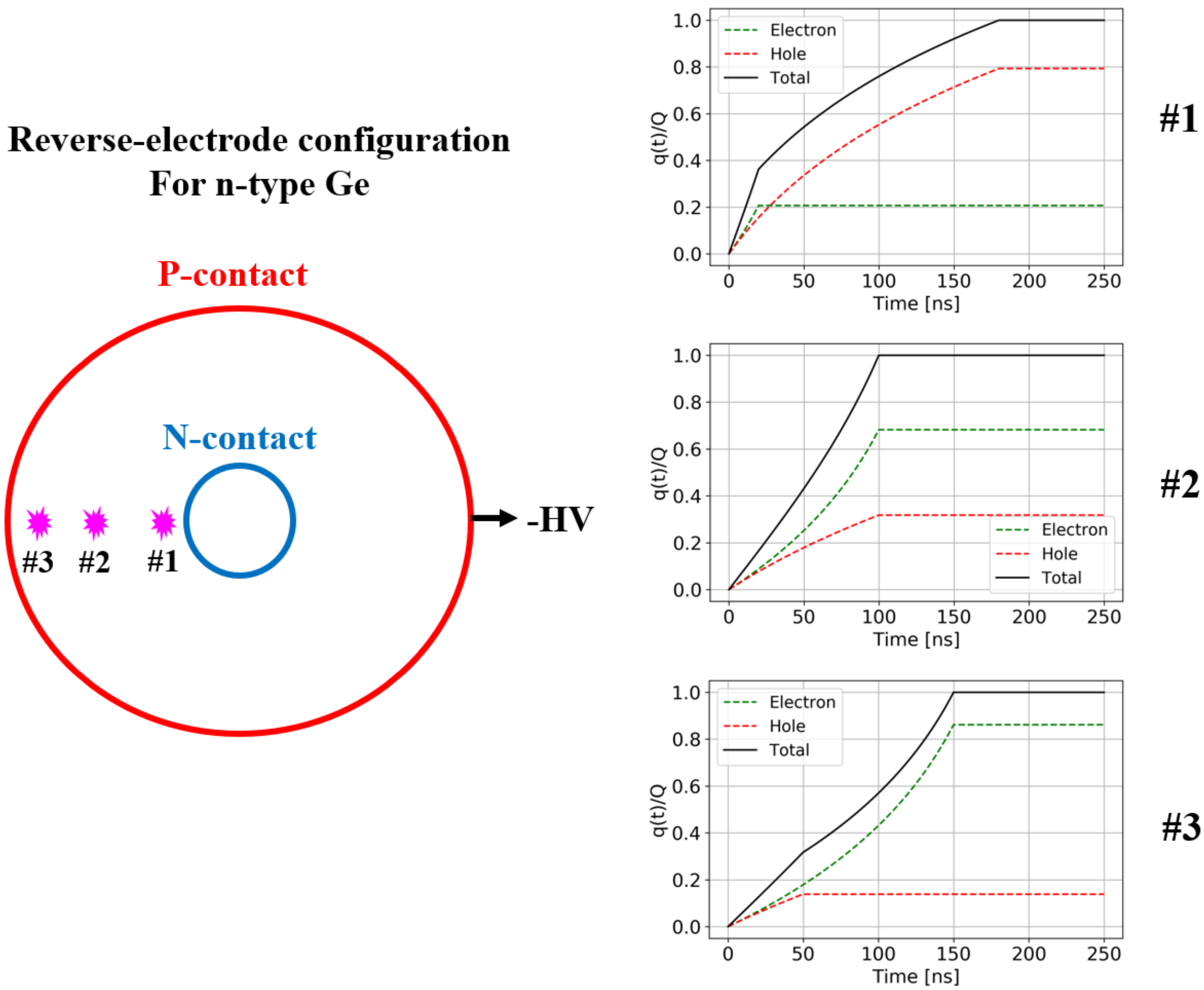

Figure 2.9: *Charge collection for reverse-electrode HPGe detectors. Gamma-ray interactions with germanium result in generation of electrons and holes. An electric field then sweeps these charge carriers to the n and p contacts, which induces charge. Shown on the left are 3 gamma-ray interaction locations in a reverse-electrode HPGe detector. The resulting induced charge from each of these interaction locations is shown on the right. Note that induced charge resulting from interactions in the outer region of the detector (#2 and #3) are dominated by electron collection. The method used to calculate induced charge is described in Appendix A.*

measurements, as two gamma rays of the same energy can induce a different amount of charge.

The probability of a hole successfully reaching the p contact without trapping was expressed by DeW et al.for a coaxial HPGe detector and is shown in Equation 2.5

$$p_q(r_o, r_p) = exp\left(-\left|\int_{r_o}^{r_p} \rho_t * \sigma_t(r)dr\right|\right) \tag{2.5}$$

where r_o is the radial position corresponding to where the hole was created, r_p is radial position of the p contact, ρ_t is the hole trap density, and $\sigma_t(r)$ is the hole trapping cross section.[66] This probability function allows one to simulate the effects of charge trapping in HPGe detectors. Using a method outlined in Appendix A.2, two simulations were performed. One considered an undamaged detector that has no significant charge trapping. The other corresponds to a detector that has been exposed to a fast neutron flux of approximately 10^{10} cm^{-2}. Detector dimensions were similar to the Dragonfly GRS. Ten thousand, 1333 keV gamma-ray interactions were simulated for each scenario and electron-hole pairs were produced in proportion to gamma-ray energy. Inherent statistical fluctuation in electron-hole pair production was considered. It was assumed that all electron-hole pairs were created at a fixed position corresponding to the gamma-ray interaction location, and interaction locations were randomly sampled from a uniform areal distribution that corresponded to the coaxial crystal cross section. Simulation results are shown in Figure 2.10. Data shown in black correspond to an undamaged detector. Statistical spread in this photopeak is due to statistical fluctuation in charge carrier production. Note that the peak is Gaussian and exhibits no significant low-energy tailing. Data shown in gray correspond a detector exposed to a large fluence of fast neutrons. The damaged detector exhibits both low-energy tailing and a decrease in photopeak centroid energy. Both of these observations indicate incomplete charge collection due to trapping. While this model is useful for illustrating the physics behind charge trapping, it is built upon simplifying assumptions that limit its ability to precisely predict spectral performance of HPGe detectors that are exposed to damaging radiation. Details about this simulation are discussed in Appendix A.2.

Broadening of the full-energy peak, or resolution degradation, has two significant implica-

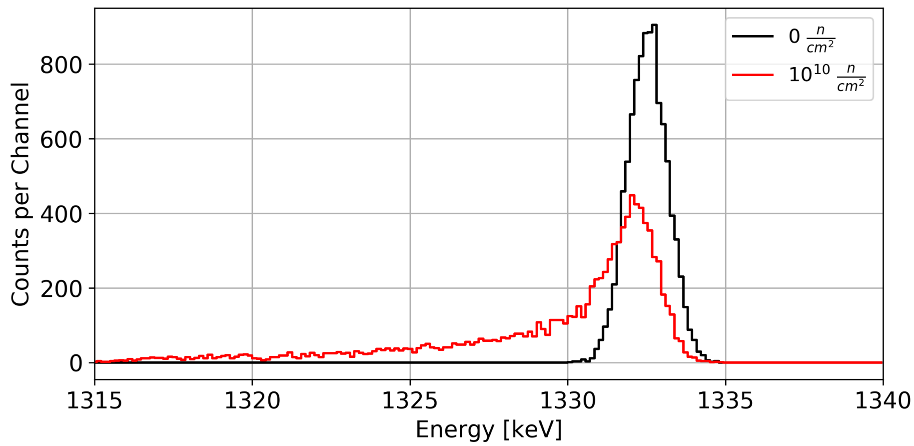

Figure 2.10: *Charge trapping simulation. Two simulations were performed to illustrate the effects of charge trapping in a reverse-electrode detector. Data shown in black represent a 1333 keV full-energy peak measured by a detector that has not been exposed to damaging radiation. Data shown in red correspond to the same gamma-ray peak measured with a detector that has been damaged by a large fluence of fast neutrons. Both simulations considered* 10^4 *gamma-ray interactions. The damaged detector exhibits two signs of charge carrier trapping: lowering of the peak centroid energy and low-energy tailing.*

tions for gamma-ray spectroscopy. First, as the peak width grows, the potential for two gamma-ray events to overlap increases. For example, neutron interrogation of Titan will result in neutron capture interactions with hydrogen and inelastic scatter interactions with sulphur that produce 2223 keV[17] and 2230 keV gamma rays[16], respectively. An undamaged detector providing ∼0.2% FWHM resolution, would be able to distinguish the two peaks with minimal overlap. However, if the detector is significantly damaged, the low-energy tail of the sulphur peak would overlap with the hydrogen peak. This decreases the ability to resolve individual gamma-ray measurements.

Second, peak broadening decreases overall detector sensitivity to gamma-ray events. Gamma-ray peaks typically sit atop a continuum, or background, that must be subtracted from the peak to determine how many events were measured. This can be considered in terms of signal and noise, where signal refers to the number of events recorded in the gamma-ray peak and noise indicates random fluctuation of the number of events in the peak and the continuum under the peak (square root of background events). If the peak area is large compared to the number of background events under it, the signal to noise ratio (SNR) is high and the number of events recorded in the peak can be known with high confidence. By the same argument, broadening of the gamma-ray peak results in a decrease of SNR and lower confidence in peak area.

Previous publications investigated neutron radiation damage in coaxial HPGe detectors. They indicate that operating temperature, crystal volume, neutron energy, and neutron fluence affects the severity of resolution degradation from radiation damage.[20;63;67;68] Table 2.3 shows the results from some of these studies. The column labeled "Neutron Environment" indicates the fluence and average energy of neutrons interacting with the HPGe detector. Initial and final FWHM refer to the 1333 keV photopeak energy resolution before and after the detector was irradiated with neutrons, respectively. Note that if relative efficiency was not provided in the publication, it was estimated using the detector volume.

Table 2.3: *Reverse-electrode HPGe neutron radiation damage experiments*

Study	Rel. Eff.	Neutron Environment	Init. FWHM	Final FWHM
Pehl et al.[65]	7%	1×10^{10} $\frac{n}{cm^2}$, 2 MeV Ave.	1.8 keV	2.7 keV
Raudorf et al.[69]	10%	4×10^{9} $\frac{n}{cm^2}$, 4.2 MeV Ave.	1.7 keV	3.0 keV
Thomas et al.[70]	23%	2.2×10^{9} $\frac{n}{cm^2}$, 1.3 MeV Ave.	1.9 keV	2.4 keV
Hull[63]	∼50%	3.2×10^{8} $\frac{n}{cm^2}$, 183 MeV Ave.	1.9 keV	2.4 keV
Borrel et al.[68]	∼40%	1.6×10^{9} $\frac{n}{cm^2}$, 5 MeV Ave.	∼2.1 keV	2.4 keV
Borrel et al.[68]	∼40%	5.0×10^{9} $\frac{n}{cm^2}$, 16 MeV Ave.	∼2.1 keV	5.75 keV
Borrel et al.[68]	∼40%	5.9×10^{8} $\frac{n}{cm^2}$, 27 MeV Ave.	∼2.1 keV	2.9 keV

Lattice defects from radiation damage in HPGe detectors can be repaired by high temperature annealing.[19] Repairing radiation-damaged n-type, cylindrical HPGe detectors has been investigated in the past.[7;63;69–72] These publications indicated that resolution degradation can be reversed if the crystal is heated for a sufficient amount of time. Table 2.4 summarizes some past HPGe annealing experiments. Note that the "Anneal Recipe" column refers to the anneal time and temperature required to achieve full energy resolution recovery. The studies shown in Table 2.4 indicate that the anneal recipe varies according to the radiation environment in which the HPGe detector is operated.

Table 2.4: *Reverse-electrode HPGe neutron radiation annealing*

Study	Rel. Eff.	Neutron Environment	Anneal Recipe
Darken et al.[71]	7%	$1 \times 10^{10} \frac{n}{cm^2}$, 2 MeV Ave.	346 hr @ 80 to 120°C
Raudorf et al.[69]	10%	$4 \times 10^{9} \frac{n}{cm^2}$, 4.2 MeV Ave.	72 hr @ 120°C
Kandel et al.[72]	40%	$1.2 \times 10^{9} \frac{n}{cm^2}$, 5 MeV Ave.	24 hr @ 105°C
Kandel et al.[72]	40%	$5.9 \times 10^{8} \frac{n}{cm^2}$, 27 MeV Ave.	216 hr @ 105°C

Annealing is not without consequences. First, HPGe detectors can not be operated during annealing due to elevated temperature (see Figure 2.1). Since annealing can take tens or even hundreds of hours, radiation damage repair significantly reduces the amount of time measurements can be performed. This downtime is especially significant for space missions, which have very tight measurement schedules and limited operation time. Second, increasing detector temperature for extended periods of time results in a loss in gamma-ray detection efficiency. This is due to thermal diffusion of the detector's lithium contact. Reverse-electrode HPGe detectors have lithium diffused into their inner bore hole. As the crystal is heated, the lithium thermally diffuses into the bulk of the crystal, reducing the volume sensitive to gamma-ray interactions. Peploski et al. investigated this effect and produced the plot shown in Figure 2.11.[7] These results indicate that annealing can significantly reduce detection efficiency.

The Dragonfly GRS will be exposed to multiple sources of radiation damage:

1. MMRTG neutrons: Dragonfly will utilize a MMRTG that converts heat energy from PuO_2 alpha decay to electrical power for the spacecraft and rotorcraft. High-energy neutrons capable of damaging the HPGe detector will continuously be emitted from the PuO_2 fuel during the ~7-year cruise and expected ~3-year surface operations. Hence, radiation damage will accrue throughout the mission.

   MMRTG neutrons are produced by three processes: spontaneous fission, (α, n) interactions with light elements, and induced fissions.[73] Photoneutron production is possible, but is negligible in comparison to the other neutron production processes.[8] Spontaneous fission neutron activity in a PuO_2 source is dominated by Pu-238, and have an

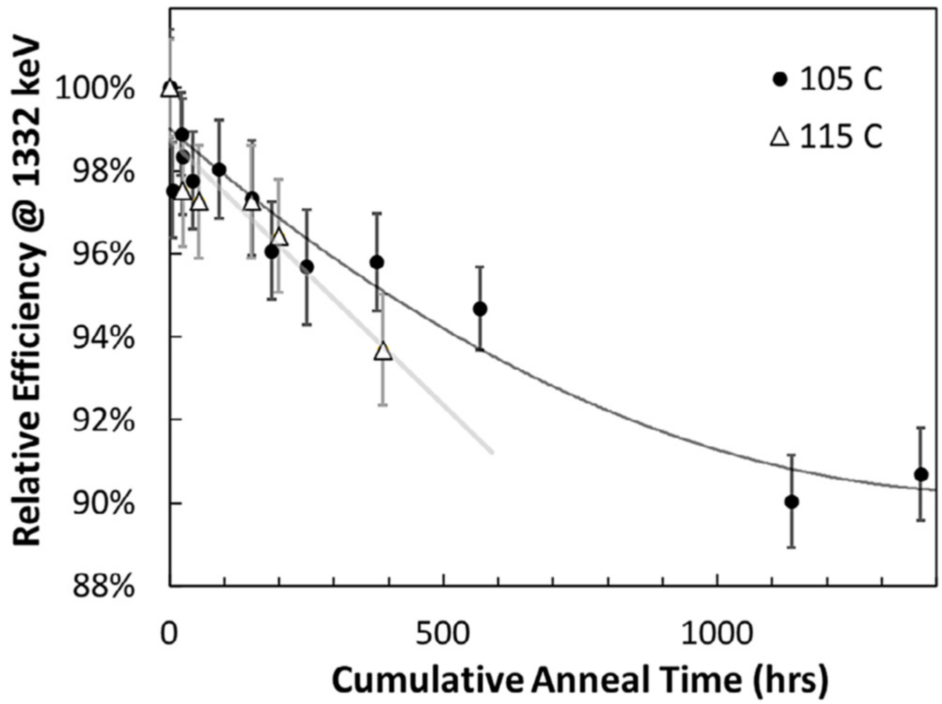

Figure 2.11: *HPGe efficiency loss from annealing.*[7] *High-temperature annealing causes efficiency loss in germanium detectors. This is due to lithium from the n-contact drifting into the crystal bulk and reducing the active volume. Peplowski et al. showed that efficiency loss was more severe at higher annealing temperatures.*

average energy of approximately 2 MeV.[8] Mass-normalized spontaneous fission neutron activity for Pu-238 and PuO_2 are 2.8×10^3 $[n * s^{-1} * g(Pu-238)^{-1}]$ and 2×10^3 $[n * s^{-1} * g(PuO_2)^{-1}]$, respectively.[8]

(α, n) activity is highly dependent on the isotopic composition of the oxygen in the PuO_2 fuel as well as light-element impurities.[8;9;73] Neutrons from from alpha interactions can dwarf those from spontaneous fission, as shown in Figure 2.12. Previous space-based MMRTGs have decreased neutron emission by significantly reducing O-17 and O-18 content in the PuO_2 fuel.[9]

Induced fission neutrons are produced when neutrons downscatter in the MMRTG fuel and packaging and cause fissions in plutonium. This process produces neutrons with energies similar to those of spontaneous fission, but their amount is dependent on MMRTG geometry. One estimate from Jet Propulsion Laboratory estimated that 45% of

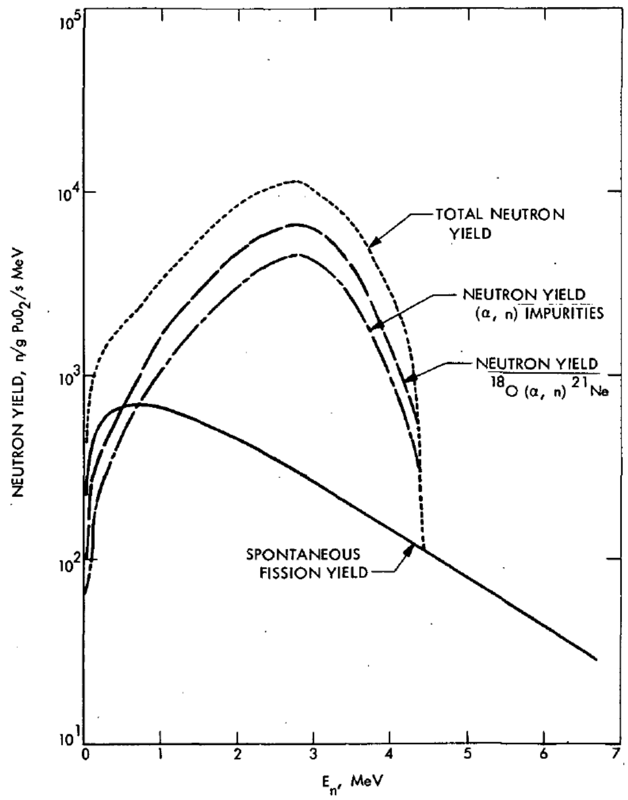

Figure 2.12: *PuO_2 fuel neutron emmission spectrum.*[8] *Neutrons are emitted from PuO_2 through spontaneous fission, (α, n) interactions, and induced fissions. Shown here is a calculated neutron emission spectrum from a MMRTG. It illustrates how low-z impurities and oxygen isotopes can contribute to PuO_2 neutron emission. Modern MMRTG fabrication reduces both components in order to lower neutron yield.*

all neutrons from a MMRTG fuel capsule were from induced fissions.[8] However, this result can not used for other MMRTGs due to differences in fuel geometry.

As of this writing, the Dragonfly MMRTG has not been fabricated. Current estimates indicate that it will contain 4.8 kg of PuO_2 and have a neutron activity of $\sim 5\times 10^3$ $[n * s^{-1} * g(PuO_2)^{-1}]$. This indicates it will emit approximately 2.4×10^7 neutrons per second. Average MMRTG neutron energy is estimated to be 2.3 MeV based on a previous publication of modern MMRTG fuel neutron emission[9] and conversations with Dragonfly MMRTG designers. A future study will characterize the Dragonfly MMRTG's neutron activity and energy distribution. It should be noted that the number and energy of neutrons interacting with the Dragonfly GRS also depends on separation distance and scattering from interactions with lander materials. While GRS-MMRTG separation distance has been estimated to be 200 cm, lander shielding effects have not been quantified as of this writing.

2. DT neutrons: A DT neutron generator producing 10^8 14.1 MeV neutrons per second will be used to interrogate Titan's surface. The DT generator will be inactive during cruise, and will perform an 8-hour interrogation at an estimated 33 landing locations during Dragonfly mission operations. Approximate GRS-neutron generator separation distance is 150 cm.

3. Galactic cosmic rays and solar energetic particles: The GRS will be exposed to high-energy particles from galactic and solar origin during its ~7 year cruise to Titan. These sources of radiation include protons and atomic nuclei that have energies ranging from sub-MeV to greater than 100 GeV, and have been shown to severely degrade deep-space HPGe GRSs.[7] Modeling Dragonfly mission cosmic ray fluence is necessary for determining expected GRS resolution degradation and the amount of annealing required to restore GRS performance.

The Dragonfly GRS will be damaged by MMRTG neutrons, galactic cosmic rays and solar energetic particles during cruise between Earth and Titan. Additionally, energetic particle interactions with the spacecraft will produce neutrons capable of damaging the GRS. During surface operations, the MMRTG and DT neutron generator will contribute to GRS resolution degradation. Cosmic rays will not be a factor during surface operations due to shielding from Titan's thick atmosphere.[14;30]

Radiation damage incurred by the GRS during cruise will be repaired via annealing when the spacecraft arrives at Titan. Note that only one "cruise anneal" is needed because the passively-cooled detector is unable to operate onboard the relatively warm spacecraft. Hence, the goal of the cruise anneal is to restore GRS energy resolution prior to measurements being performed on Titan's surface. Cruise anneal duration is being investigated by APL. Their study builds upon a past work that investigated galactic cosmic ray and solar energetic particle radiation damage and repair for the the Psyche and Martian Moons eXploration (MMX) deep-space HPGe detectors.[7]

Whether or not the Dragonlfly GRS will require annealing during surface operations has not been determined as of this writing. DM GRS thermal and vacuum design allows a surface anneal, but this is only needed if radiation damage during surface operations degrades energy resolution past the 4.2 keV FWHM specification. Eliminating the surface-anneal capability would allow GRS thermal and vacuum design to be simplified. This work investigates Dragonfly GRS energy resolution degradation during surface operations due to MMRTG neutrons. While DT generator neutrons will also damage the GRS, DT fluence will be less than 10% of MMRTG fluence at the GRS (assuming $distance^{-2}$ flux dependence and no shielding materials between the neutron sources and the GRS). Studies presented in Table 2.3 indicate that resolution degradation from neutron damage varies significantly depending on experimental conditions, including neutron energy, neutron fluence, and detector volume (indicated by its relative efficiency specification). Additionally, crystal temperature can affect the severity of radiation damage.[67] The many contributions to energy resolution degradation in HPGe detectors made it inadvisable to use previous radiation damage studies to predict Dragonfly GRS spectral performance on Titan. Hence an experiment was performed to investigate GRS resolution degradation due MMRTG neutron radiation damage. Annealing was also investigated, allowing for an anneal recipe to be formulated. Efficiency loss due to lithium diffusion was monitored throughout the annealing process.

Chapter 3

Dragonfly GRS Testing

The Dragonfly GRS DM is a functional HPGe detector designed for the Dragonfly mission. This system must survive rocket launch, be able to passively cool and anneal on Titan's surface, and be sensitive to neutron-induced gamma rays. The following chapter overviews experiments performed to ensure the system will achieve these goals. Additionally, GRS performance degradation from neutron radiation damage is documented and subsequent repair is presented.

3.1 Rocket-Launch Survivability

The DM's ability to survive rocket launch was evaluated through multiple laboratory tests. The methods, results, and implications of these experiments will be discussed in this section.

3.1.1 Vibration Testing Methods

At the time of this writing, Dragonfly launch loads are not yet determined. In lieu of mission-specific vibration loads, the DM was designed survive two generic spacecraft vibration environments. The first is a 35 g sine burst test between 5 and 50 Hz. This test is intended to determine if the system can survive high-g, quasi-static forces and investigate for workmanship issues.[74] The second is a random vibration test between the frequencies of 20 an 2 $\times 10^3$ Hz. Random testing evaluated if the GRS can survive acoustic forces associated with launch. Details of the random vibration testing performed on the DM can be found in Goddard Space Flight Center's (GSFC) General Environmental Verification Standard (GEVS).[74]

Forces associated with rocket-launch are three dimensional. However, only a one-axis vibration table was available during detector development. Specialized jigs were fabricated that allowed the DM to be oriented in multiple ways to allow for testing along each axes. Hence, three separate tests were performed to evaluate DM compatibility with rocket launch. Subsequent versions of the Dragonfly GRS will be evaluated using a three-dimensional vibration table.

The vibration table was fitted with a control accelerometer and programmed to produce a desired vibration profile. This accelerometer provided feedback for ensuring the vibration table was performing correctly. Another accelerometer was placed on the suspended encapsulated crystal, allowing for system response to be monitored. The experimental setup is shown in Figure 3.1. GRS resonance response to vibration testing was observed by compar-

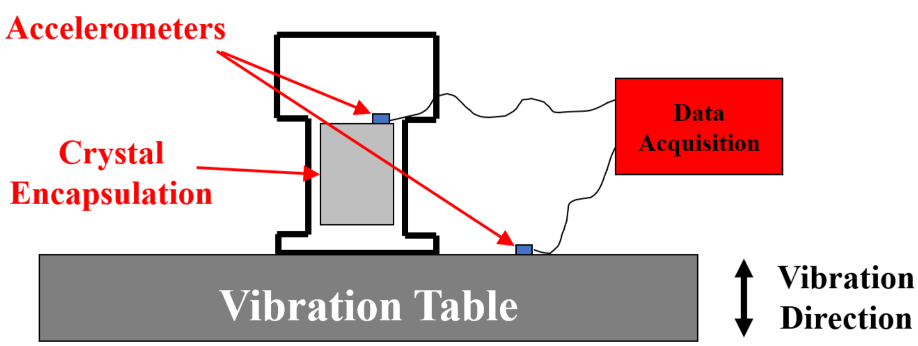

Figure 3.1: *Experimental configuration for DM vibration testing. DM vibration testing utilized two accelerometers: one was placed on the vibration table to measure the output vibration profile and another was placed on the encapsulated crystal to measure DM response. Data from both accelerometers were saved using a digital acquisition system.*

ing the control and encapsulation accelerometers. The ratio of the encapsulation acceleration to the control acceleration is the response ratio. A response ratio much greater than unity indicates the presence of a resonance. The DM resonates at several frequencies, as shown in Figure 3.2.

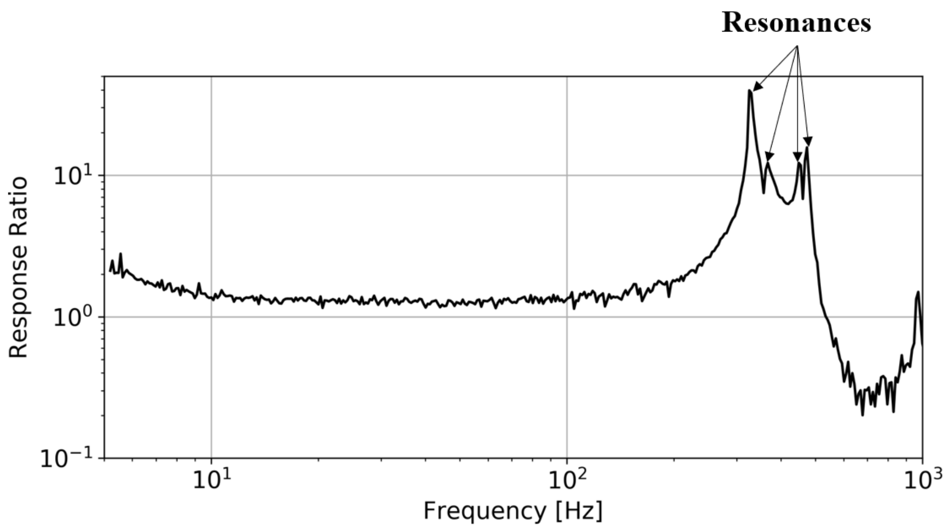

Figure 3.2: *DM resonance response. Use of accelerometers allowed DM resonance response to be measured. Resonances are indicated when the acceleration measured by the encapsulation accelerometer is much higher than the acceleration provided by the vibration table. The ratio of the encapsulation acceleration to the input vibration is reported as the response ratio in this plot. Resonance frequencies are indicated by peaks in the data. These frequencies were monitored before and after vibration testing to look for changes in DM structural properties.*

A procedure was developed to test the DM's ability to survive rocket launch. Testing began by determining the encapsulated crystal's baseline energy resolution. Commercially-available amplifier electronics and dipstick cryostat were used for this measurement. A Co-60 gamma-ray source was positioned $\sim$20 cm away from the side of the detector. The detector was biased at +3 kV, and pulse processing was performed using a trapezoidal filter with parameters 8 μs rise time and 0.8μs flat top width. This resulted in a dead time of approximately 2%. The measurement was performed until greater than 10^4 events were recorded in the 1332.5 keV photopeak.

Next, the encapsulation was removed from the commercial cryostat and installed into the DM cryostat for vibration testing. The system was initially vibrated at 0.5 g between 5 and 2×10^3 Hz. This test, referred to as a pre-vibration sine survey, indicates the frequencies at which the system resonates. The system was then subjected to GEVS random vibration, a

35 g sine burst measurement, and another sine survey. The vibration testing procedure is summarized below:

1. Pre-vibration 0.5 g sine survey
2. GEVS random vibration
3. Sine burst test
4. Post-vibration 0.5 g sine survey

The above measurements were performed on each GRS axis, resulting in 3 sets of 4 measurements. After the vibration campaign, the encapsulated detector was removed from the DM cryostat and reinstalled into the commercially-available cryostat. Another gamma-ray measurement was performed using similar conditions as the initial measurement.

The pre and post-vibration gamma-ray measurements were intended to determine if: 1) the detector became damaged during vibration in such a way that prevented operation and 2) if vibration testing affected detector spectral performance, specifically energy resolution. Monitoring system resonances before and after the vibration campaign indicated if the system sustained major structural damage. The frequencies at which the DM resonates are functions of the GRS's mechanical properties, such as material stiffness and detector preload. Hence, a post-vibration change in resonance frequencies would indicate that a structural change occurred. This would be interpreted as a failure, as the system is not designed to be mechanically changed by vibration.

3.1.2 Detector Performance Before & After Vibration Testing

Figure 3.3 shows DM resonance response after z-axis vibration, as indicated by the pre and post-vibration sine surveys. Table 3.1 summarizes results of the pre and post-vibration sine survey measurements that were performed on each axis. Gamma-ray measurements performed before and after vibration testing are shown Figure 3.4. FWHM energy resolution was 1.8 keV for both measurements.

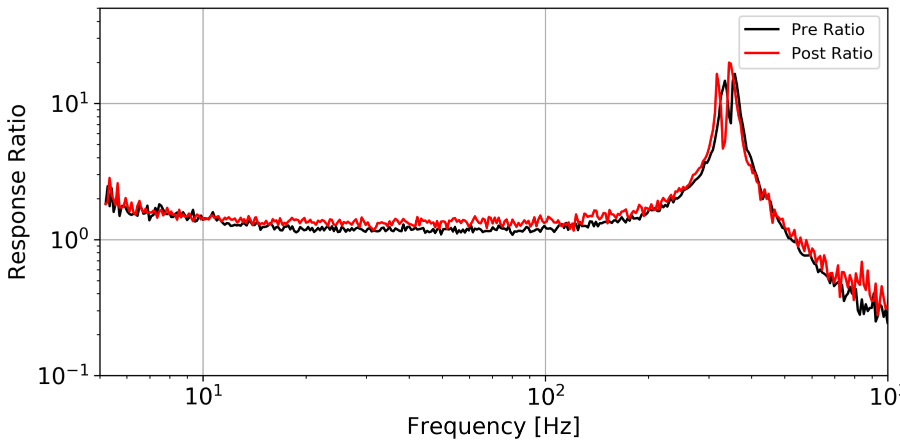

Figure 3.3: *Z-Axis Pre and Post-Vibration Resonance Response. Low-g sine survey measurements were performed before and after each DM axis was vibration tested. The y-axis indicates the ratio of the acceleration reported by the encapsulation and control accelerometers. Data shown in black and red data indicate system response before and after z-axis vibration testing, respectively. DM resonance frequencies are indicated by peaks in the spectrum.*

Table 3.1: *DM Resonance Analysis Before and After Vibration Testing*

Parameter	Peak 1	Peak 2	Peak 3	Peak 4
Z-Axis				
Pre-Vibe Frequency	334 Hz	358 Hz	N/A	N/A
Pre-Vibe Ratio	14.6	16.4	N/A	N/A
Post-Vibe Frequency	317 Hz	346 Hz	N/A	N/A
Post-Vibe Ratio	16.4	19.8	N/A	N/A
X-Axis				
Pre-Vibe Frequency	328 Hz	367 Hz	451 Hz	473 Hz
Pre-Vibe Ratio	38.9	12.2	12	15.5
Post-Vibe Frequency	321 Hz	367 Hz	449 Hz	473 Hz
Post-Vibe Ratio	34.3	11.2	11.5	16.3
Y-Axis				
Pre-Vibe Frequency	326 Hz	358 Hz	372 Hz	455 Hz
Pre-Vibe Ratio	11.9	19.7	32.7	31.5
Post-Vibe Frequency	311 Hz	339 Hz	366 Hz	455 Hz
Post-Vibe Ratio	15	20	11.9	25

3.1.3 Vibration Testing Discussion

The Dragonfly DM was subjected to spaceflight-like vibration loads to determine if it could survive rocket launch. Pass/fail criteria was determined by resonance analysis, spectral per-

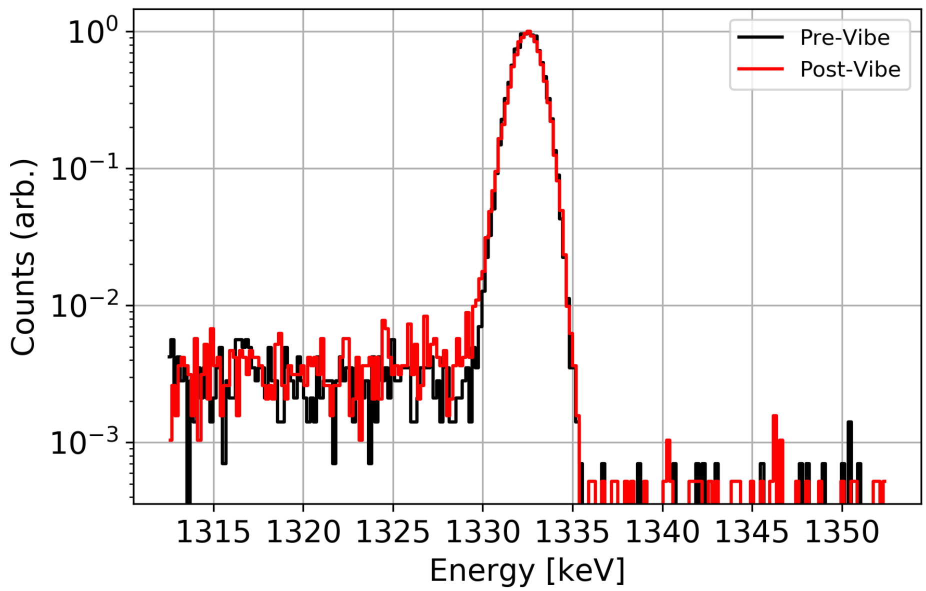

Figure 3.4: *Pre and post-vibration spectral measurements. Co-60 gamma-ray measurements were performed before and after the Dragonfly DM was vibration tested. The measurements shown in black and red were performed before and after the vibration campaign, respectively. FWHM resolution was 1.8 keV for both measurements. Note that the peaks were normalized to the same height for easy comparison of peak shapes.*

formance, and CT scans. Pre and post-vibration sine surveys indicated if major changes in resonance frequencies occurred. What constitutes a major change in resonance frequency varies according the type of component being tested. Experience developing spaceflight detectors[33] that utilized a similar mechanical design indicates that resonance shifts greater than ∼15% are of concern and may point to mechanical failure. Smaller changes are attributed to settling of the Kevlar suspension.

Table 3.1 shows the resonance peaks and amplitudes measured by the low-g sine surveys. Although some frequency shifts were observed, they were small do not indicate structural damage. No major amplitude increases were observed, however there were significant decreases in amplitude observed during y-axis testing. This is attributed to settling in the the Kevlar suspension system and is not of concern. Results from resonance analysis indicate that the DM did not experience major mechanical failures during vibration. Additionally, data from this measurement can be referenced and compared against when future Dragonfly

GRSs are vibration tested. Significant differences in resonance response may indicate workmanship problems or assembly issues.

Results from resonance analysis were supplemented by comparing detector spectral performance before and after the vibration campaign. This method indicated if the detector was operable after vibration and, if so, whether energy resolution was degraded. The spectral measurement shown in Figure 3.4 indicates that the GRS remained functional after vibration and that it did not exhibit resolution degradation. Additionally, the detector was used for gamma-ray measurements for the 6 months following vibration testing and showed consistent energy resolution. This indicates that vibration testing did not compromise the encapsulation vacuum, as a vacuum breach would allow contaminants to condense on the crystal surface and degrade resolution.

The encapsulated detector was also computational tomography (CT) scanned before and after vibration testing. These measurements were performed to determine if the crystal tilted or if the encapsulation components (such as the getter) were damaged after vibration testing. The pre and post-vibration CT scans indicated the crystal did not move during vibration and that internal structures were undamaged. CT scans are not shown in this work to protect intellectual property.

3.2 Dragonfly GRS Passive Cooling and Annealing Measurements

The Dragonfly DM's ability to passively cool to operating temperature and anneal for low input power was demonstrated experimentally. Data from this experiment was then used to tune a thermal model that can simulate DM thermal performance in various conditions. This section describes experimental methods and results, as well as thermal model benchmarking efforts.

3.2.1 Thermal Testing Techniques and Methods

DM thermal performance was measured in an environmental chamber in conditions similar to those expected on Titan: the chamber was purged with gaseous nitrogen and held at 93 +/- 1 K. Encapsulated HPGe crystals were unavailable at the time of this measurement. Instead, a representative aluminum cylinder was used. In order to make this measurement realistic, the detector proxy was designed to have the same heat capacity as an encapsulated crystal. It was constructed similarly to the crystal encapsulation, which allowed it to be suspended via the low-conductivity Kevlar suspension system and use a DM-style wiring scheme. Lastly, the cryostat was vacuum evacuated per the baseline DM design.

The detector proxy was outfitted with an anneal heater and a DT-470 Si diode temperature sensor. The heater was used to apply heat power to the encapsulation to facilitate annealing, and the temperature sensor reported encapsulation temperature throughout the experiment. A SAES D100 getter was used to maintain vacuum inside the DM. Temperature was recorded and monitored via a LakeShore 218E temperature controller, and anneal heater power was documented by hand. The cryostat was supported by its bottom flange using a thin metal grate that allowed cold, gaseous nitrogen to interact with all exterior cryostat surfaces. Figure 3.5 shows the system in the environmental chamber.

DM cooling began with the cryostat and crystal encapsulation at 290 K and 320 K, respectively. Environmental chamber temperature was initially 293 K, but cooled to 93 K within a few minutes of the start of the experiment. Once the system cooled below ∼100 K, the anneal heater was activated and the detector proxy was heated to anneal temperature.

3.2.2 Passive Cooling and Annealing Performance

The measured cooling curve is shown in Figure 3.6. Note that the latter five measurements have different temporal spacing than previous measurements. This is because automatic temperature logging software was not used after approximately 73 hours into the measurement. After that point, temperature and time were documented by hand.

Figure 3.5: *DM thermal experiment. Dragonfly DM thermal performance was measured under Titan-like conditions. It was passively cooled and annealed in a 93 K gaseous environment. Cooling time and anneal power were recorded throughout the experiment.*

After cooling, the DM was annealed. Steady-state detector proxy temperature was 370 K with 1.85 W of anneal power. Note that this temperature is slightly lower than the anneal temperature goal of 378 K (see Chapter 1). This is because the anneal heater was set to a constant output power rather than operated using a control loop. 370 K was the temperature at which the system equilibrated with a constant input power. Power could have been incremented up until a steady-state detector temperature of 378 K was achieved, however this was not possible in the time available to perform the experiment. .

3.2.3 Thermal Testing Discussion and GRS Performance on Titan

Thermal testing investigated the DM's ability to meet thermal performance requirements associated with the Dragonfly mission. As of this writing, the GRS is required to passively cool to operating temperature within the first 16 days of landing on Titan and be able to be annealed on Titan's surface using less than 5 W of heater power. Results shown in Section 3.2.2 show that the DM can passively cool to operating temperature in a Titan-like environment within 6 days and be annealed with less than 2 W input power.

Experimental results were used to benchmark and tune the thermal model presented earlier in this work. Model parameters were updated to be consistent with experimental conditions: a solid aluminum cylinder rather than a germanium/aluminum detector encapsulation was modeled, no heat from the lander bracket was included in the model, and the starting temperature was set to be consistent with experimental conditions. Next, the assumed surface emissivity used for modeling infrared heat transfer was adjusted slightly to achieve good agreement between measured and modeled data. As discussed in Appendix B, an emissivity value of 0.05 was chosen, which is consistent with the process used to machine infrared transmitting surfaces in the DM. Figure 3.6 shows that modeled and measured cooling curves. Comparison of measured and simulated DM cooling and annealing indicates the thermal model accurately simulates DM thermal performance. The maximum difference between measured and simulated detector temperature during passive cooling is less than 1%, which is sufficiently accurate for predicting DM thermal performance. Modeled and measured annealing power were also compared. Measurements indicate that 1.85 W of input power results in a detector temperature of 370 K. The thermal model predicts the detector will reach 372 K with the same amount of annealing power.

The validated thermal model was then used to predict DM thermal performance on Titan.

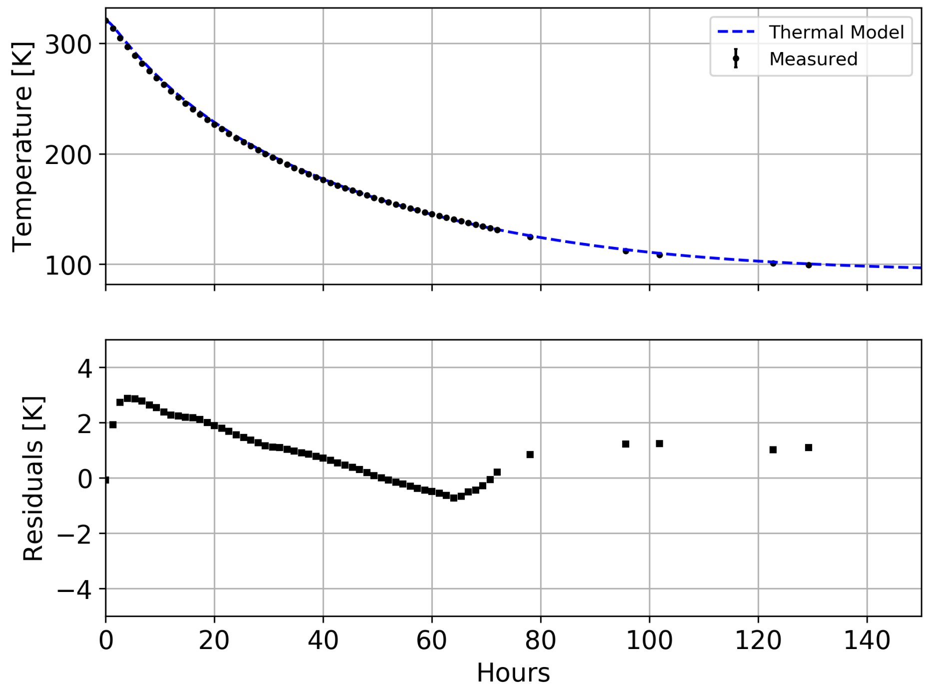

Figure 3.6: *DM passive cooling and thermal model.* ***Top:*** *Black markers show measured data from the passive cooling experiment. At time = 0, the DM was placed in a 93 K, gaseous nitrogen environment and passively cooling began. Detector temperature vs cooling time is shown here. Automated temperature and time logging software was used for measurements before time = 73 hours. Subsequent measurements were documented by hand. The dashed blue line shows predicted cooling from the thermal model.* ***Bottom:*** *Black squares indicate the difference between the measured and modeled temperature. All deviations between measured and simulated temperature were <1%.*

It was assumed that the cryostat and crystal encapsulation were held at 273 K during cruise, then exposed to Titan's atmosphere (94 K, 2.7 $[\frac{W}{m^2 * K}]$ convection coefficient) at time = 0. Heat input from the lander (q_L in Figure 2.6) was assumed to be 1 W, which is consistent with current estimates provided by mission planners. Figure 3.7 shows the predicted encapsulation and cryostat temperature versus time. The thermal model predicts that the DM will cool to operating temperature within 6.5 days of landing on Titan, and is capable of annealing for 1.9 W of input power. This indicates that the design will meet thermal requirements.

It should be noted that there are uncertainties remaining regarding DM thermal performance on Titan. One example is the way in which the GRS will be mounted onto the rotorcraft. At the time of this writing, the attachment method and location has not been determined. Two

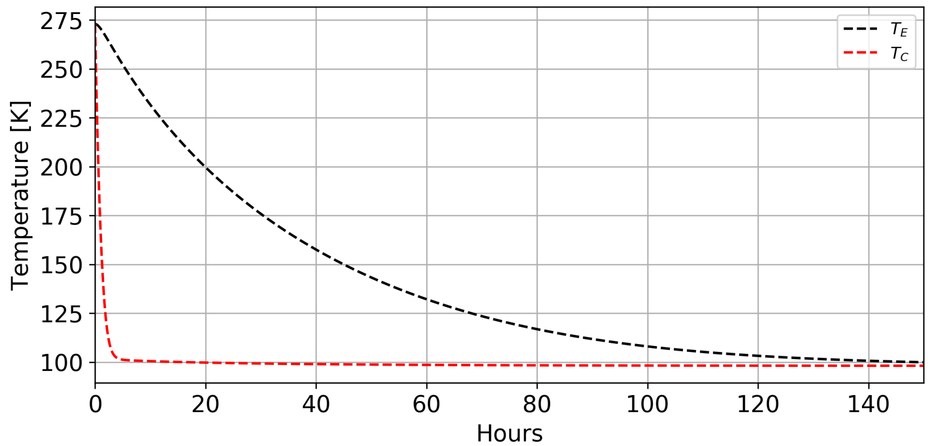

Figure 3.7: *Simulated Dragonfly DM passive cooling on Titan's surface.The thermal model was used to estimate the crystal encapsulation temperature (T_E, shown in black) and the cryostat temperature (T_C, shown in red) during passive cooling on Titan's surface. The model predicts that crystal will cool to operating temperature within ∼6.5 days of landing on Titan's surface.*

possible locations are shown in Figure 3.8. If the GRS is mounted near the body of the lander,

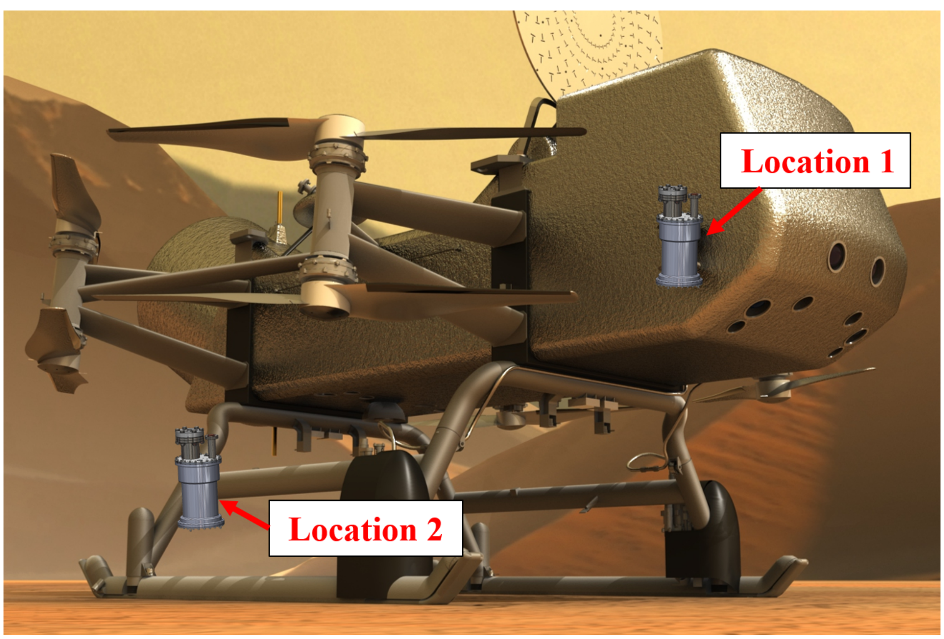

Figure 3.8: *Potential GRS mounting locations. At the time of this writing, GRS mounting location on the lander has not been finalized. Two potential locations are shown here. If the GRS is mounted on the lander shell, a significant amount of heat could be transferred to the cryostat, which would increase crystal temperature. If mounted on the lander skids, much less heat would be transmitted to the cryostat, and crystal temperature would be similar to Titan ambient.*

shown as Location 1, the attachment bracket will penetrate through the insulated lander shell and attach to the rotorcraft frame. Heat will then be transferred from the relatively warm rotorcraft interior to the cold cryostat. The wiring harness connecting DM electronics to the rotorcraft also contributes to this effect. As indicated by the thermal model, steady-state crystal temperature is the same as the outer cryostat temperature. Hence, heat input from the rotorcraft directly affects crystal operating temperature. If heat flow is high enough, crystal temperature may exceed the maximum operation temperature of 100 K. Heat flow from the rotorcraft via the attachment bracket and wiring harness is balanced by convective cooling to Titan's atmosphere. Steady-state crystal temperature can be calculated using Equation 3.1

$$T_{Crys} = \frac{q_{\mathrm{L}}}{h * A_{surf}} + T_{Amb} \tag{3.1}$$

where $\mathrm{T_{Crys}}$ is the steady-state crystal temperature, $\mathrm{q_L}$ is heat flow from the lander due to the mounting bracket and the wiring harness, h is the convective coefficient on Titan (estimated to be 2.7 $\frac{Watts}{m^2 * K}$), $\mathrm{A_{surf}}$ is the outer surface area of the cryostat, and $\mathrm{T_{Amb}}$ is Titan's surface temperature. Estimated steady-state crystal temperature versus heat input from the lander is shown in Figure 3.9. If the GRS is mounted on the lander skids, shown as Location 2 in Figure 3.8, heat transfer from the rotorcraft will be much smaller, as the landing skids are heat sunk to Titan's environment. The steady-state crystal temperature at Location 2 will be approximately 94 K.

It should be noted that heat lift due to Titan's ambient conditions is a source of uncertainty. The convection coefficient used in this work is an average of a range of convection coefficients calculated by analyzing data from the Huygens Probe.[46] It is unlikely that this data is perfectly applicable to the Dragonfly GRS, as gas flow around the system will be different from that of the Huygens Probe. While the thermal model presented in this work indicates the GRS will meet thermal requirements, it should be revisited when a Dragonfly Mission-specific convection coefficient is calculated.

Another source of uncertainty is GRS vacuum condition. This work investigated thermal

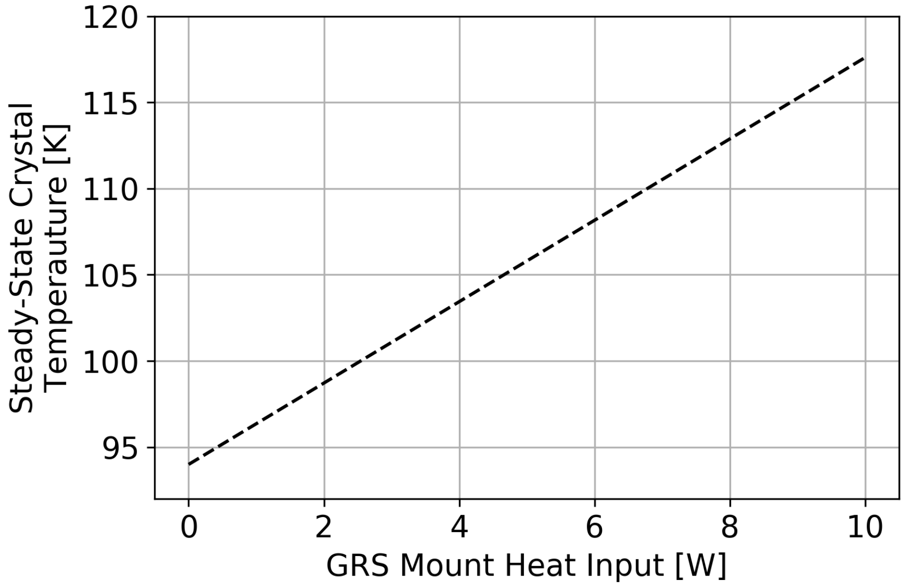

Figure 3.9: *Effect of heat from rotorcraft (via bracket and electrical harness) on crystal temperature. Heat from the rotorcraft can travel to the GRS cryostat via the mounting bracket and electrical harness. If heat flow is high enough, the steady-state GRS temperature can exceed its intended operating temperature of 100 K.*

performance of the DM which is vacuum evacuated using a non-evaporable getter. However, at the time of this writing, GRS vacuum design has not been finalized. Other vacuum maintenance methods are being investigated, such as zeolite molecular sieves and space-venting through a valve. Even a design that doesn't maintain vacuum at all is being considered. Each of these strategies correlate to a different vacuum condition inside the GRS and have major implications for the amount of power required for annealing (see Appendix B). Therefore, there will be significant uncertainties in GRS thermal performance until the vacuum design is determined.

The benchmarked thermal model presented in this work helps mitigate some uncertainty in Dragonfly GRS design. It can easily be updated to reflect changes in lander heat input, estimated Titan convection coefficient, and/or vacuum condition, making it a valuable tool for evaluating the thermal performance of future Dragonfly GRS design iterations.

3.3 GRS Vacuum Characterization and Measurements

The baseline Dragonfly GRS design calls for the cryostat to be vacuum isolated from the environment. This work performed multiple experiments to quantify the amount and types of gasses in the DM cryostat. It also investigated the efficacy of using a non-evaporable getter for vacuum maintenance.

3.3.1 Methods used for Measuring Gas Load and Type

A test station was created to facilitate DM vacuum measurements. Turbomolecular and ion pumps were mounted onto a reducer Tee and were connected to a 4-way cross via a UHV valve. The remaining three flanges on the cross were connected to the DM, a Pfeifer CMR 375 capacitance pressure gauge, and a Stanford Research Systems (SRS) 100 AMU residual gas analyzer (RGA). The test station is shown in Figure 3.10.

UHV vacuum practices were followed throughout DM vacuum testing, including using UHV-rated components and metal seals and always wearing gloves when handling vacuum components. It should be noted that the DM does not require pressure to be in the UHV range to operate properly. Rather, following UHV guidelines helps mitigate contamination and outgassing that could significantly contribute to DM gas load.

System gas load was measured using the rate of rise (RoR) method.[57] This technique involves pumping a chamber, then isolating it with a valve. Pressure inside a well-baked chamber will increase linearly with time, and the time rate of pressure increase in the chamber is proportional to gas load. This is shown in Eq 3.2

$$Q = \frac{\Delta P}{\Delta t} * V \tag{3.2}$$

where Q is gas load, P is pressure, t is time, and V is gas volume. DM gas volume is approximately 1 liter. This document will use the units $[mbar * liter * s^{-1}]$, mbar, seconds, and liter for gas load, pressure, and time, respectively.

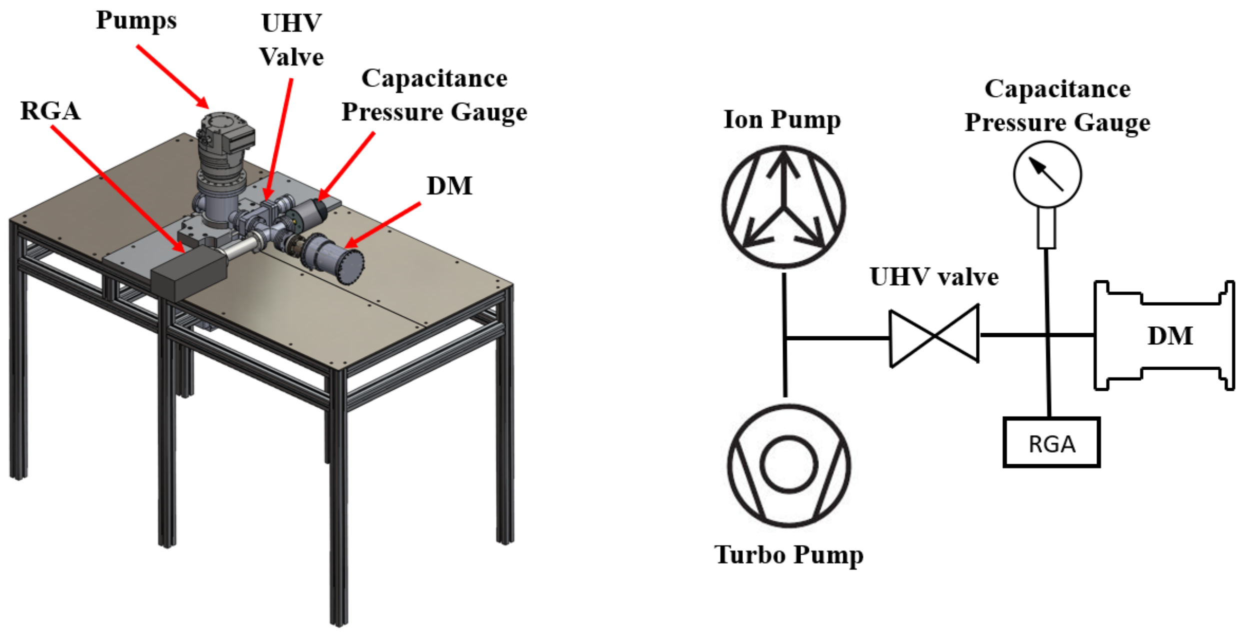

Figure 3.10: *Test station used for gas load and type measurements.* ***Left****: A CAD drawing of the Dragonfly vacuum test station is shown. This was used for gas load and gas type measurements.* ***Right****: A schematic representation of the vacuum test station is shown. An ion and a turbo pump were connected to a four-way cross via a UHV valve. The DM, a capacitance pressure gauge, and a RGA were connected to the remaining cross flanges. The capacitance gauge indicated DM pressure and the RGA monitored DM gas type.*

Prior to the gas load measurment, the DM was baked for 5 days at 373 K while being pumped by the turbo and ion pumps. This baking temperature was chosen because the encapsulated crystal's maximum temperature rating is 378 K. After the 5-day bake, the system passively cooled to room temperature and the UHV valve was closed. This isolated the DM from the vacuum pumps and caused pressure to increase due to gas load. Pressure increase was measured by the capacitance pressure gauge and recorded by a Pfeiffer TPG 366 pressure gauge controller. It should be noted that a D100 non-evaporable getter was installed in the DM prior to the start of the experiment. However it was not activated until after gas load and type measurements. This ensured that pumping from the getter was negligible.[53]

DM gas type was measured using the SRS RGA shown in Figure 3.10. Shortly after the gas load measurement was completed, the UHV valve was opened and the DM was again pumped using the laboratory pumps. Once base pressure was reached, the RGA was activated and a gas-type measurement was recorded.

The DM's ability to maintain its vacuum using a getter was measured indirectly by observing the amount of power required to anneal the crystal encapsulation. When the DM is vacuum evacuated, anneal power is a function of solid conduction and infrared heat transfer. However, as pressure increases, gas thermal conduction begins to increase proportionally (see Section B.6). This allowed an experiment to be designed to monitor cryostat vacuum condition via anneal power.

At the start of the experiment, the DM had been pumped and baked via laboratory pumps for approximately 5 days (corresponding to the gas load and type measurements mentioned above). The getter was activated and the system was separated from laboratory pumps by a copper pinch tube. DM anneal power was recorded for two configurations, each of which had a different boundary condition. In one configuration, the exterior surfaces of the DM were exposed to room-temperature air (∼293 K). The DM was submerged in liquid nitrogen (77 K) in the other configuration. Power was supplied to the anneal heater until the encapsulation temperature reached a steady-state value of ∼378 K. Power was then documented and the heater was deactivated. These measurements were repeated multiple times over approximately 5 months.

3.3.2 Vacuum Characterization and Hold Time Measurements

After baking, the DM gas load was measured to be 9×10^{-9} $[mbar * liter * s^{-1}]$. The corresponding RoR measurement is shown in Figure 3.11. The RGA scan of the baked, room-temperature DM is shown in Figure 3.12.

DM vacuum hold time was investigated immediately after gas load and type measurements. Note that the DM was not exposed to atmospheric conditions between measurements. Figure 3.13 shows measured anneal power versus elapsed time for two DM boundary conditions: room temperature and liquid nitrogen. At the start of the measurement, the getter was activated and the system was separated from laboratory pumps. The getter was not reactivated

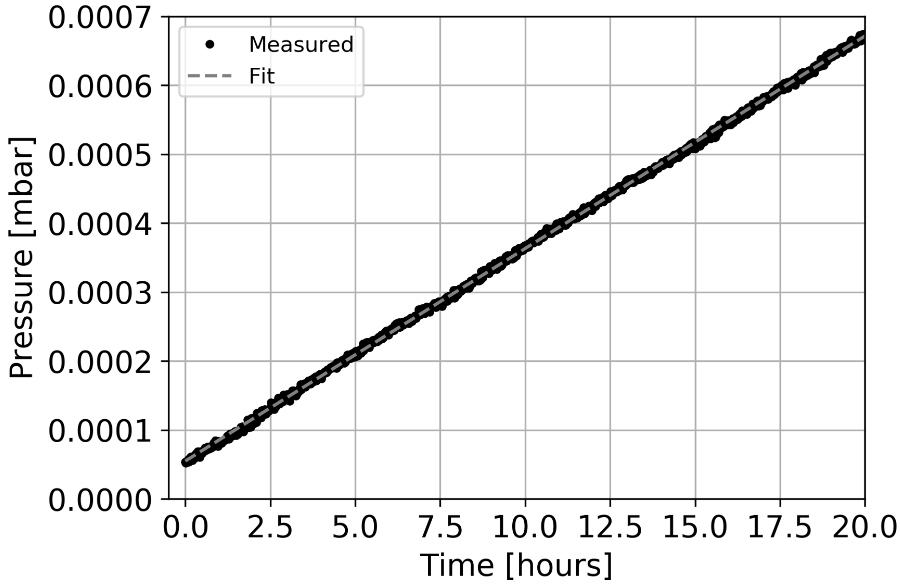

Figure 3.11: *Room-temperature ROR measurement. The DM was pumped and baked for approximately 5 days at 100˚C, then allowed to passively cool. Gas load was measured via RoR once the system reached room temperature.*

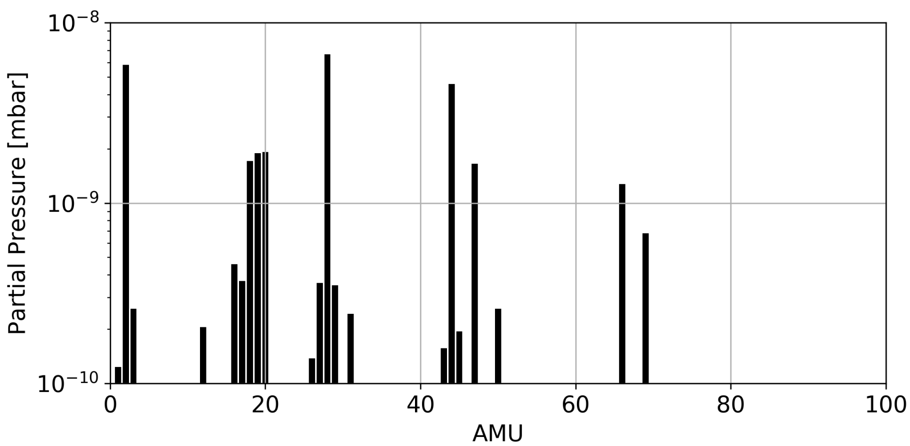

Figure 3.12: *Room-temperature RGA Measurement. A RGA measurement was performed on the well-baked DM to characterize the types and relative amounts of gasses in the system.*

during the measurement.

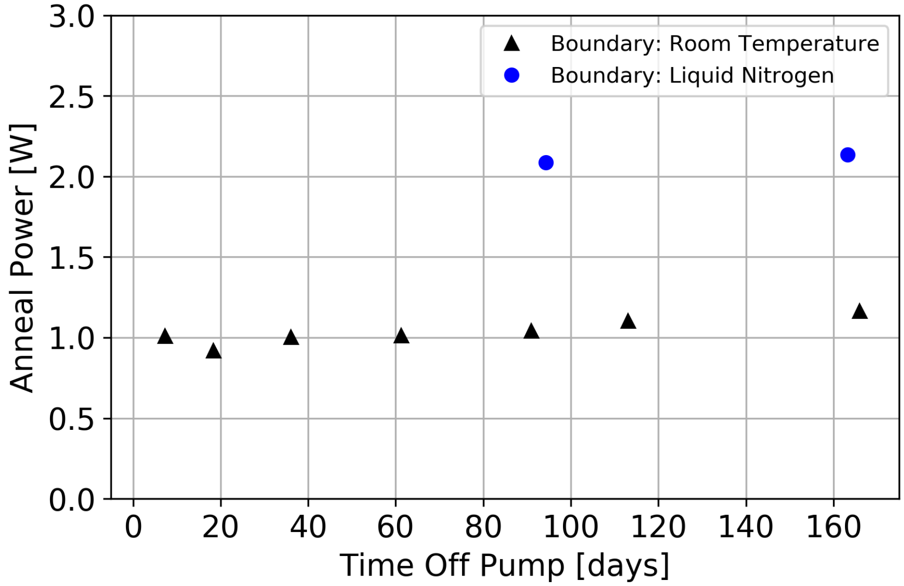

Figure 3.13: *Vacuum-hold measurement. The ability of the DM to maintain vacuum using a getter was investigated by recording anneal power over several months. At the beginning of the experiment (time = 0), system had been baked at 373 K for 5 days and the getter had just been activated. Data shown in blue circles corresponds to the liquid nitrogen boundary condition, in which the DM was held at 77 K during annealing. Data shown in black triangles corresponds to a room-temperature boundary condition.*

3.3.3 Vacuum Measurement Discussion and Implications

Results from vacuum measurements indicate that pumping and baking the DM for ∼5 days will result in a gas load of 9 $\times 10^{-9}$ $[mbar * liter * s^{-1}]$ (including leaks and outgassing) when all components are held at room temperature. This is a positive result and it seems unlikely that DM gas load could be significantly decreased below this amount for several reasons. First, the DM contains $\sim 2\times 10^3$ cm^2 of aluminum and stainless steel surfaces. Hence, if outgassing from metal surfaces were the only contributors to gas load, the area-normalized gas load would be $\sim 5 \times 10^{-12}$ $[mbar * liter * s^{-1} * cm^{-2}]$. This is near the outgassing rate expected for well-baked stainless steel.[57] Note that it is unlikely that metal surfaces are the only sources of outgassing, as the DM contains nearly a foot of braided Kevlar and PTFE wire insulation that has a large effective surface area.

Second, the DM has two electrical feedthroughs that have non-zero leak rates. The high voltage connector[38] is specified to have a maximum helium leak-rate of 10^{-8} $[atm * cc * s^{-1}]$ and the MDM connector[39] is specified to have a helium leak rate less than 10^{-9} $[atm*cc*s^{-1}]$. These can be converted to air leak rates by using Equation 3.3

$$\frac{L_{He}}{L_{Air}} = \sqrt{\frac{M_{Air}}{M_{He}}} \tag{3.3}$$

where L_{He} is the specified helium leak rate, L_{Air} is the equivalent air leak rate, M_{He} is the molar mass of helium (4 $[g * mol^{-1}]$), and M_{Air} is the molar mass of air (29 $[g * mol^{-1}]$). Use of Equation 3.3 indicates that the combined air leak rate through both feedthroughs is not guaranteed to be lower than 4×10^{-9} $[mbar * liter * s^{-1}]$. This is approximately half of the measured DM gas load.

The DM gas load measurement likely overestimates gas load during cruise, as it was performed with approximately 1 bar pressure differential across the cryostat seals and feedthroughs. This resulted in a non-zero leak rate and gas permeation. During cruise the cryostat will be exposed to space-vacuum, which will eliminate atmospheric gas infiltration. Furthermore, colder temperature during cruise and on Titan's surface will also decrease gas load.

RGA measurements indicate that the primary gasses in the DM cryostat produce RGA peaks at 2, 28, and 44 AMU. The peak at 2 is from H_2, which is the primary outgassing component in vacuum systems prepped for ultra-high vacuum.[57] A peak at 28 AMU could be from N_2 or CO. RGA fragmentation patterns indicate that ionization of N_2 should result in a 14 AMU fragment with 12% magnitude of the 28 AMU signal. As shown in Figure 3.12, no such fragment was measured. Detection of CO should result in a 5% contribution to the 12 AMU peak, which is visible in the RGA scan. The peak at 44 AMU is the primary signal from CO_2 fragmentation. Other CO_2 fragments include 28, 16, and 12 AMU, listed in order of decreasing magnitude. This is consistent with the DM RGA measurement.

Water is present in the system, as evidenced by RGA scan features at 16, 17, and 18 AMU. Contributions from this gas source could be reduced further by more baking. Peaks at 19, 20, 50, and 69 AMU are likely from polytetrafluoroethylene (PTFE) tubing used to provide insulation for cryostat wiring. This can not be known for certain, as the RGA was only able to scan for gasses less than or equal to 100 AMU. Further investigation is needed, but replacement of PTFE insulators with polyether ether ketone (PEEK) versions is being considered. PEEK offers both insulation and are ultra-high vacuum compatible. Lastly, the peak at 66 AMU is likely a fragment of a large-chain hydrocarbon molecule. Personal experience indicates that this RGA trace is associated with hand oil. While gloves were always used when handling DM components, cross contamination is possible. This measurement indicates that handling procedures should be followed more carefully in subsequent builds.

RGA analysis indicates that the major contributors to DM gas load are able to be captured by the getter. The D100 has massive hydrogen capacity, and significant capacity for CO and CO_2. If one assumes that the DM gas load is comprised equally of H_2, CO, and CO_2, then one could expect the getter to maintain pressure inside the cryostat of less than 10^{-8} mbar for between one and two years. This is a conservative estimate of vacuum hold time, as gas load will be lower when the system is cool during cruise and on Titan's surface. Once the getter is saturated, it would need to be reactivated to migrate adsorbed CO and CO_2 from the getter's surface to its internal volume. Once reactivation is completed, the getter surface will be clear of adsorbed gasses and be able to continue to maintain vacuum.

A SAES D100 getter was shown to maintain DM vacuum under two thermal boundary conditions: room temperature and liquid nitrogen. There were two motivations for using liquid nitrogen. First, an environmental chamber was not available for the entirety of this measurement. Liquid nitrogen, however, was readily available. Second, use of liquid nitrogen provided a conservative estimate of anneal power on Titan. The convection coefficient associated with liquid is higher than that of Titan's gaseous atmosphere. Additionally, liquid nitrogen temperature is $\sim$17 K lower than that of Titan. These two considerations make the liquid-nitrogen anneal power shown in Figure 3.13 an overestimate of what is expected during Titan surface operations.

This experiment shows that the Dragonfly GRS is capable of maintaining vacuum sufficient for annealing for greater than 160 days and indicates that a getter-only strategy is viable for the Dragonfly GRS. However, more testing is needed. Getters can adsorb a finite amount of gas before they saturate, at which point they can no longer pump gasses. The finite nature of getter pumping means that the results shown in Figure 3.13 can not be extrapolated to many years. Hence, longer-term testing is needed to investigate whether the getter can maintain vacuum throughout the mission.

3.4 Detecting Radioisotope and Neutron-Induced Gamma-rays

This section will discuss DM spectral measurements performed in a Titan-like thermal environment. Energy resolution was quantified and the system was shown to be sensitive to neutron-induced gamma rays relevant to gamma-ray spectroscopy on Titan.

3.4.1 Experimental Methods for Gamma-ray Detection in a Titan-like Thermal Environment

Gamma-ray measurements were performed with the DM GRS in a flight-like configuration. The system consisted of an encapsulated detector mounted in the cryostat via Kevlar suspension. The cryostat was sealed using indium, a getter maintained vacuum, and an APL-developed, charge-sensitive amplifier was used for signal readout. The amplifier was separated into two regions. The cold side attached to the top of the cryostat and housed an AC-coupled JFET and feedback loop. The warm side contained an Op Amp and connected to the cold components by $\sim$1 m cables. It was kept at room temperature throughout the measurement. The output of the warm-side amplifier connected to an ORTEC DSPEC 50[75] that provided trapezoidal pulse shaping and amplification. The DSPEC 50 was also used as a multi-channel analyzer and supplied bias voltage to the detector. A desktop computer and ORTEC Maestro software were used to record and display measured data. The preamplifier was outfitted with a test input that allowed a low-noise pulser signal to be injected into the JFET gate. The pulser signal, which is not subject to the statistical fluctuations inherent to gamma-ray signals, propagates through the detector electronics chain and is reported in the MCA as a Gaussian peak. The statistical spread of the pulser peak allows detector electronic noise to be quantified.

Care was taken to create Titan-like conditions during DM testing. A pressurized environmental chamber was not available during this phase of detector development. Instead, an 81 liter liquid nitrogen dewar[76] was used to passively cool the GRS. The detector was suspended inside the dewar so that its lower half was submerged in liquid nitrogen. The top portion of the DM and the cold region of the amplifier were above the liquid nitrogen level. This was done to prevent liquid nitrogen from interacting with the preamplifier electronics. Crystal temperature was 77 K throughout the measurement.

A NIST-calibrated 18.2 μCi Eu-152 gamma-ray source was used to characterize DM energy resolution. Figure 3.14 shows the experimental setup used for this measurement.

Capture and inelastic scatter gamma rays were measured by interrogating 6 kg of high-density polyethylene (HDPE) and 7 kg NaCl with a Cf-252 neutron source that produced 3.5×10^4 neutrons per second. This allowed DM sensitivity to gamma-rays with energies up to 8.6 MeV to be measured. Figure 3.15 shows the experimental setup for neutron-induced gamma-ray measurements. Borated HDPE bricks and bags of boric acid were used to lower neutron radiation dose in the area around the experiment. The detector was biased at +3 kV for both the Eu-152 and Cf-252 measurement. Pulse processing was performed using a trapezoidal filter with parameters 14 μs rise time and 1.0μs flat top width. Measurement dead time for the Eu-152 and Cf-252 measurements were 13.5% and 3.5%, respectively.

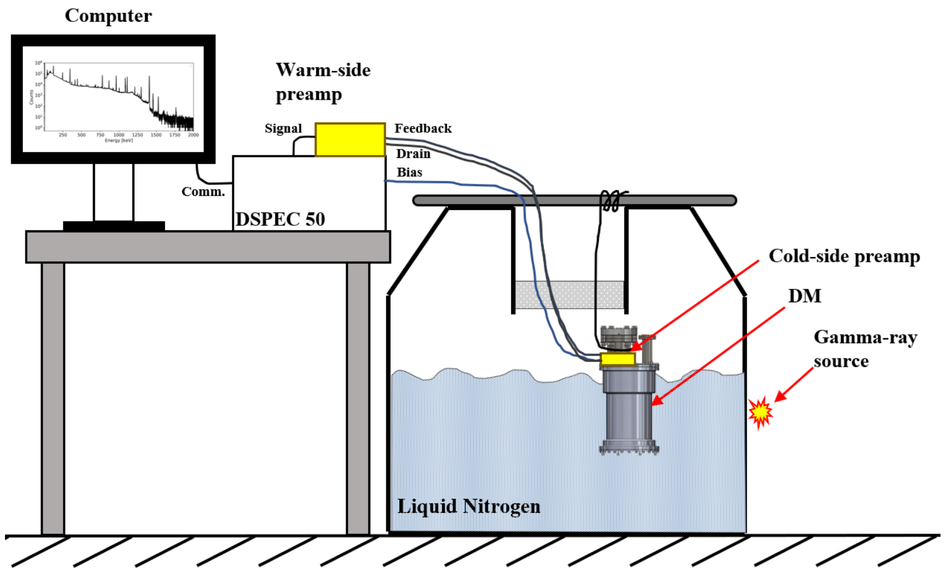

Figure 3.14: *DM Eu-152 gamma-ray measurement. The DM was passively-cooled to 77 K by being placed in a large liquid-nitrogen dewar. An Eu-152 gamma-ray source was placed outside the dewar, approximately 30 cm away from the DM. A custom amplifier was used for charge collection and an ORTEC DSPEC 50 was used for signal processing and bias voltage supply.*

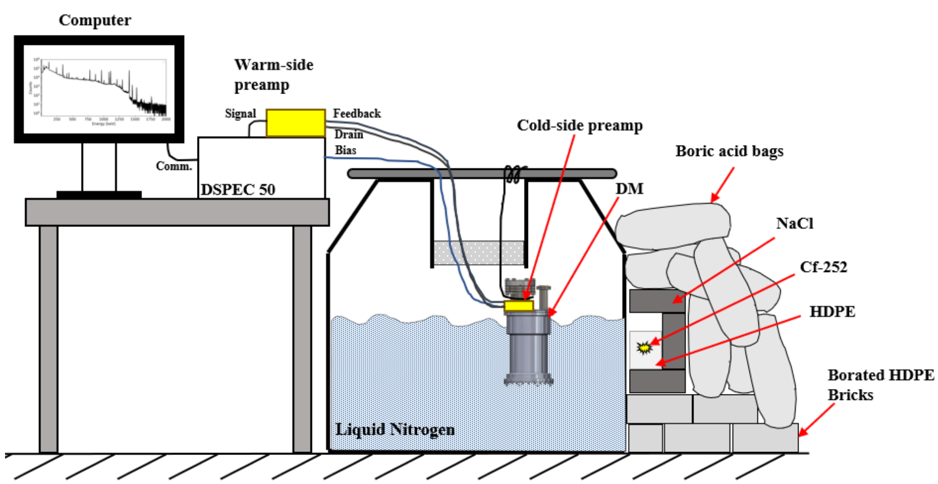

Figure 3.15: *DM neutron-induced gamma-ray measurement. An 8.1 μCi Cf-252 source was placed just outside the dewar, approximately 30 cm away from the DM. The source was enclosed by an HDPE cylinder and surrounded by NaCl bricks. The experiment was shielded by borated HDPE and boric acid.*

3.4.2 Gamma-Ray Measurements

The Eu-152 gamma-ray spectrum is shown in Figure 3.16. Detector live time for this measurement was 11.1 hr and a test pulser signal was injected into the preamplifier to quantify electrical noise to be 1.92 keV FWHM. Eu-152 decay results in the emission of multiple gamma rays, and the 10 most probable are identified in Figure 3.16.[20]

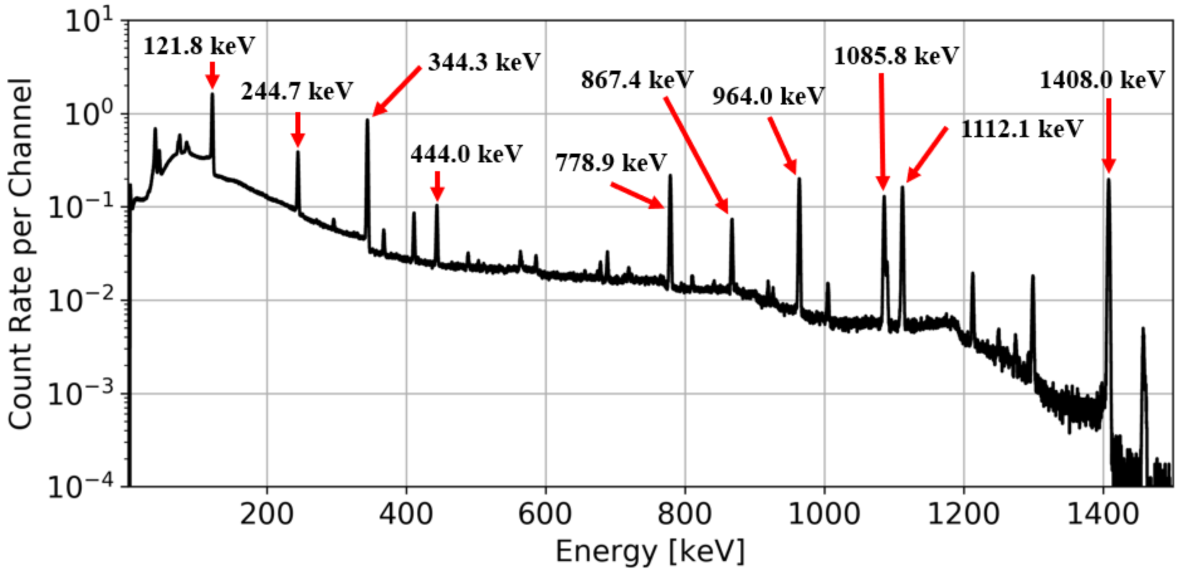

Figure 3.16: *Eu-152 gamma ray spectrum. The DM was used to measure gamma-rays emitted from Eu-152 gamma-ray source. Detector live time was 11.1 hours and total count rate was 3350 counts per second (CPS). The 10 most probable gamma-ray emissions from Eu-152 decay are shown.*

A 6.5-day measurement of neutron-induced gamma-rays was performed using the configuration shown in Figure 3.15. Electronic noise for this configuration was 2.1 keV. The resulting spectrum is shown in Figure 3.17. Peak areas and measurement details are shown in Appendix C.

3.4.3 GRS Spectral Performance

The DM was used to measure gamma-rays from radioactive isotopes and from neutron interactions with various materials. The purpose of these measurements was to demonstrate that the Dragonfly DM is able to perform gamma-ray spectroscopy in a Titan-like environment. Measurements performed in this work also verified the performance of custom preamplifier electronics.

Figure 3.18 shows DM energy resolution as a function of gamma-ray energy. The width of a

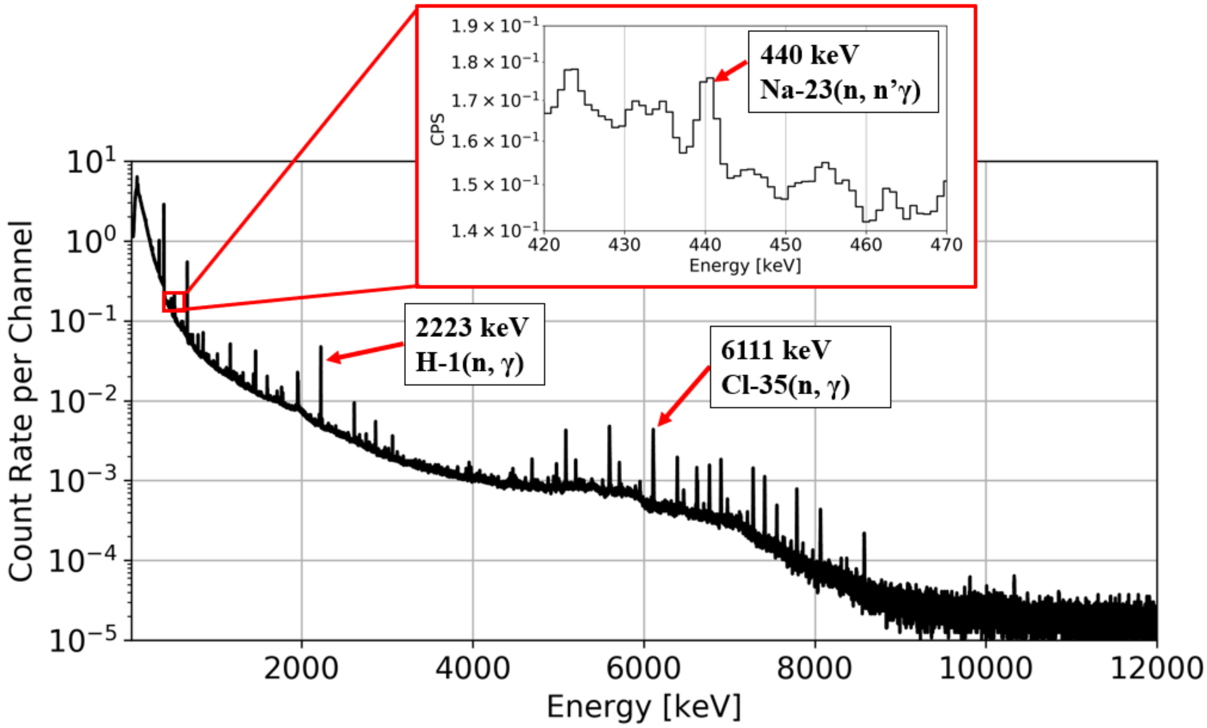

Figure 3.17: *Neutron-induced gamma-ray spectrum. A Cf-252 neutron source was used to measure gamma-rays from neutron interactions with hydrogen, sodium, and chlorine. Gamma-rays identified for measurement on Titan (see Table 1.1) are visible in this spectrum. Detector live time was 155.9 hours and gamma-ray count rate was 834 CPS.*

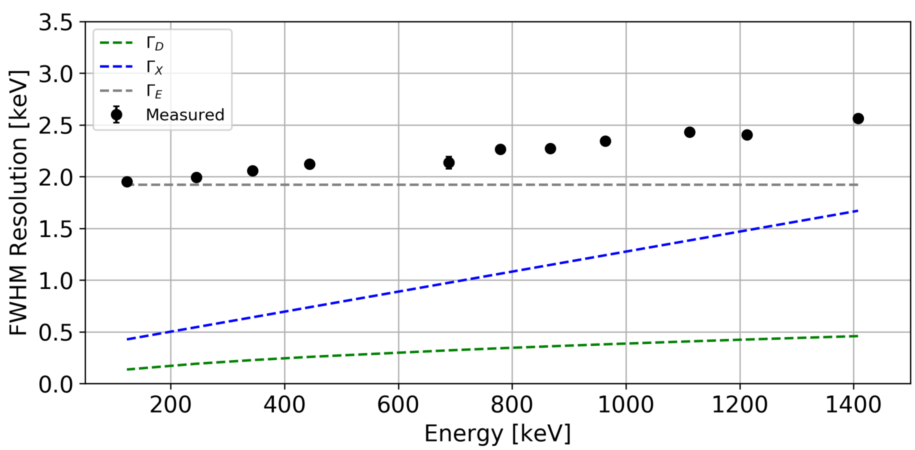

Figure 3.18: *DM FWHM resolution. An Eu-152 gamma-ray source was used to quantify GRS energy resolution at multiple energies. Measured FWHM energy resolution is shown by the black markers. Contributions from statistical fluctuations of charge carrier production, incomplete charge collection, and electronic noise are shown by the green, blue, and gray dashed lines, respectively.*

gamma-ray full-energy peak is determined by three factors: Statistical noise in charge carrier production (Γ_{D}), incomplete charge collection (Γ_{X}), and broadening due to electronic components (Γ_{E}).[20] The individual contributions to DM resolution are identified in Figure 3.18. Each factor contributes to total resolution (shown as black circles in Figure 3.18) according to Equation 3.4.

$$\Gamma_T = \sqrt{\Gamma_D^2 + \Gamma_E^2 + \Gamma_X^2} \tag{3.4}$$

Γ_{D} is a function of the number of charge carriers produced by gamma-ray energy deposition and is shown in Equation 3.5

$$\Gamma_D^2 = 2.35^2 * F * \epsilon * E \tag{3.5}$$

where F is the Fano factor, ϵ is the energy needed to produce an electron-hole pair, and E is gamma-ray energy.[20] The Fano factor scales Poisson-statistic predicted charge carrier fluctuation to a value that agrees with experimental data, and is approximately 0.08 for germanium detectors.[20] The energy needed to produce and electron-hole pair is approximately 2.96 eV. Peak broadening from statistical fluctuation was calculated using Equation 3.5 and is shown by the green line in Figure 3.18. Electronic noise (Γ_{E}) was determined to be 1.92 keV using an electronic pulser and is shown in the gray dashed-line in Figure 3.18. Γ_{X} was calculated by rearranging Equation 3.5 and is shown as a blue line in Figure 3.18. This measurement indicates that the DM is producing energy resolution well below its specification of 4.2 keV. However this can be improved, as the main contributor to DM energy resolution is electronic noise. A lower noise amplifier is currently being developed by APL.

Figure 3.17 shows that the DM is able to measure gamma-rays produced from neutron interrogation of sodium, chlorine, and hydrogen targets. Three gamma-rays identified for measurement on Titan are shown in Figure 3.17. Detection of these elements indicate the the DM GRS is able to measure gamma rays relevant to Dragonfly science requirements while both using custom preamplifier electronics and operating in a cryogenic environment.

3.5 Dragonfly GRS MMRTG Radiation Damage and Repair

The Dragonfly rotorcraft will operate for multiple years on Titan's surface. It will be powered by an MMRTG, which converts thermal energy from PuO_2 alpha decay to electric energy. Fast neutrons capable of degrading GRS spectral resolution will also be continuously emitted. Energy resolution degradation due to these fast neutrons was quantified through experimentation. Additionally, repair of neutron radiation damage through annealing was also investigated.

3.5.1 Radiation Damage and Annealing Experimental Setup and Methods

A custom dipstick cryostat provided by Mirion, Inc. was used for the radiation damage and repair experiment. A Dragonfly encapsulated detector was installed into the cryostat and was conductively-cooled by a $\sim$75 cm copper rod. One end of the rod was placed in a LN dewar and was held at 77 K and the other was heat sunk to the encapsulated detector. Though the cryostat was vacuum evacuated to thermally-isolate the encapsulated detector, infrared and conductive heat input caused the encapsulated detector to be held at a steady-state temperature of 99 K. Cooling time to reach this temperature was approximately 4 hours. It should be noted that the DM cryostat was not used for this experiment due to its long passive-cooling time. Figure 3.19 shows the dipstick cryostat. The cryostat allowed the encapsulated crystal to connect to commercially-available preamplifier electronics. The preamplifier output was connected to an ORTEC DSPEC 50 shaping amplifier and MCA, which also provided bias voltage to the detector. The DSPEC 50 was connected to a laptop computer and ORTEC Maestro software was used to record pulse-height spectra.

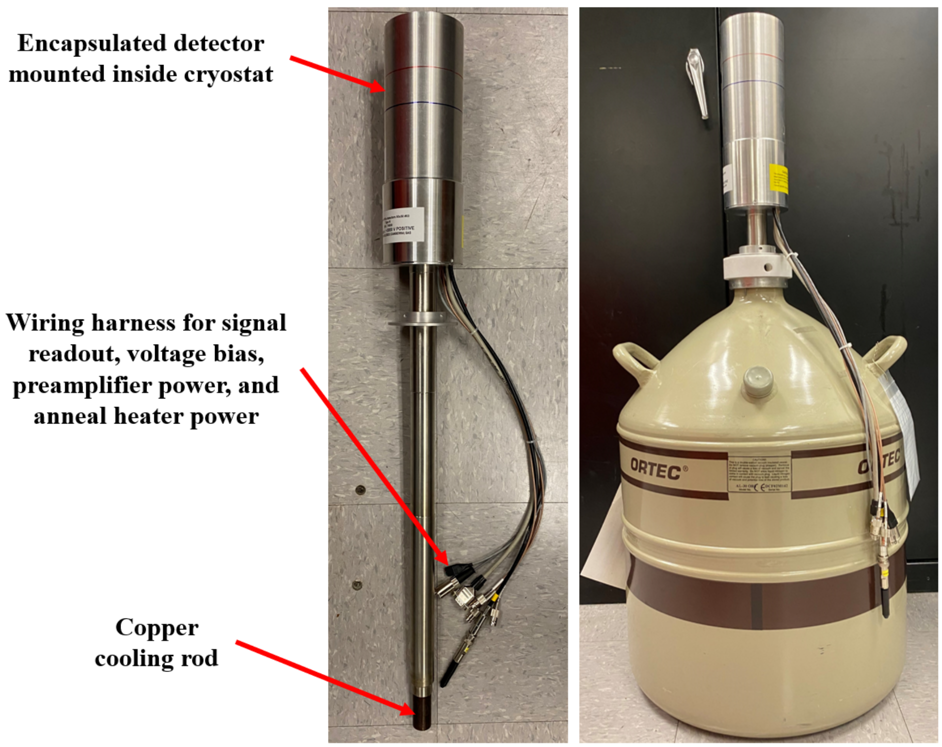

Figure 3.19: *Liquid-nitrogen dipstick cryostat.* ***Left:*** *A custom cryostat was used to house the Dragonfly encapsulated crystal for the radiation damage and repair experiment. The vacuum-evacuated cryostat used liquid nitrogen to conductively cool the crystal to 99 K via a copper rod. The system used commercially-available preamplifier electronics for signal readout and was outfitted with an anneal heater for radiation damage repair.* ***Right:*** *The dipstick cryostat was mounted onto a portable liquid nitrogen Dewar that allowed the detector to be kept at a constant temperature during neutron irradiation.*

3.5.1.1 Radiation Damage

The detector was irradiated with a plutonium-boron (PuB) neutron source. This source was chosen because it offered a similar neutron energy spectrum to that of a MMRTG. Figure 3.20 compares MMRTG and PuB neutron spectra. The PuB source had neutron activity

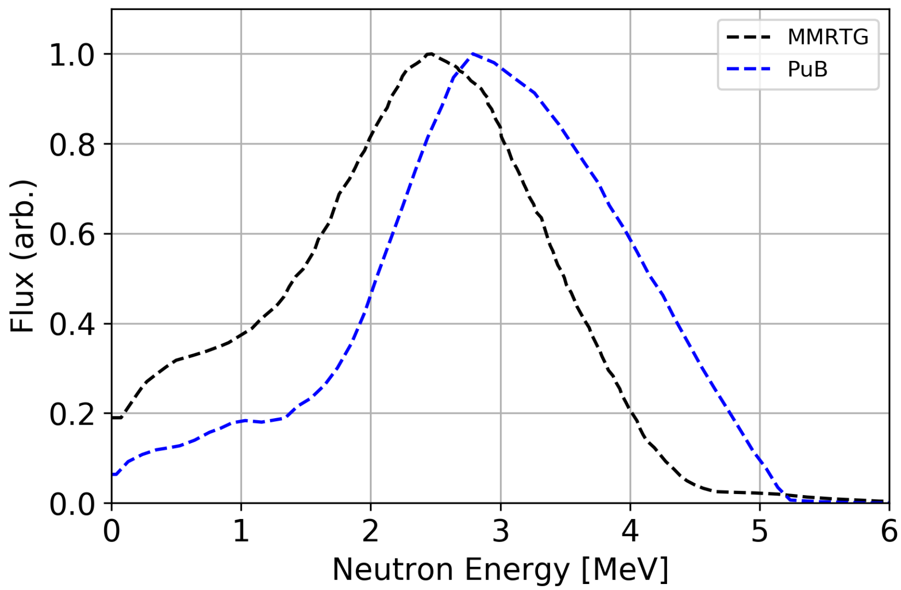

Figure 3.20: *Comparison between PuB and MMRTG neutron spectra. Data shown in black is from a publication by Smith that simulated neutron energy spectra from a generic MMRTG with fuel composition representative of past space MMRTGs.[9] Data shown in blue is from a simulation by Gauld et al. that calculated the neutron energy spectrum from PuB.[10] The average neutron energies of simulated MMRTG and PuB neutrons were 2.3 and 2.9 MeV, respectively.*

of 5×10^6 neutrons per second at the time of the experiment and was encapsulated in a 31 mm diameter by 40 mm long stainless steel shell. Other sources of radiation associated with this source include alpha particles and gamma rays, both of which do not contribute to GRS lattice damage. The source was placed approximately 68 mm away from the centerline of the coaxial HPGe crystal, as shown in Figure 3.21. The center of the source was vertically aligned with the center of the crystal. MCNP6 was used to estimate neutron flux in the HPGe crystal. The PuB neutron source was modeled as a distributed source with a neutron emission spectrum from Gauld et al.[10] The encapsulated detector was also modeled and a

F4 tally was used to determine neutron flux inside the crystal.

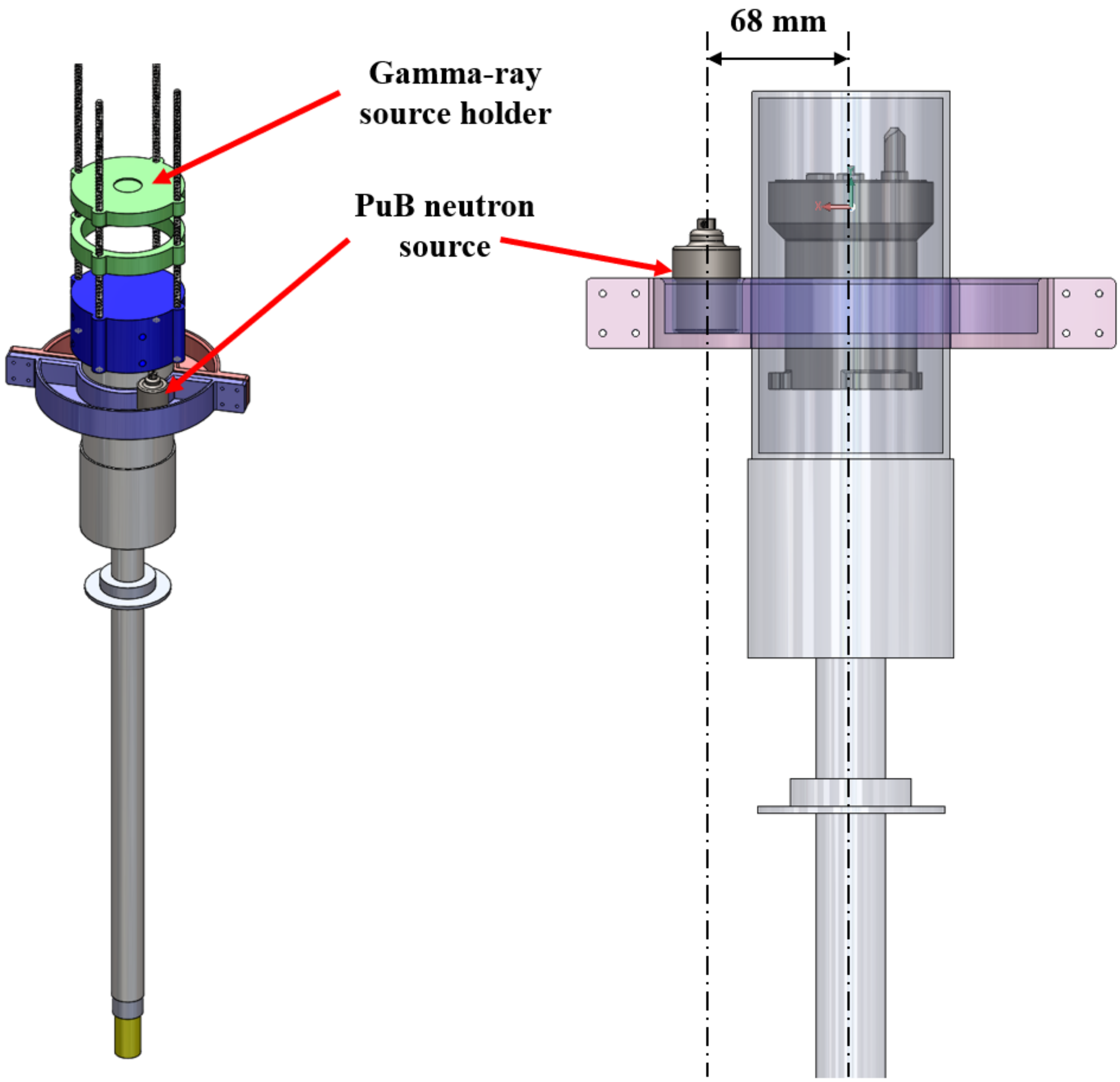

Figure 3.21: *Dipstick cryostat with neutron and gamma-ray source holders.* ***Left:*** *The PuB neutron source was placed in a tray and vertically aligned with the center of the HPGe crystal. A source holder was used to position a gamma-ray check source 25 cm away from the planer face of the coaxial HPGe crystal.* ***Right:*** *The PuB neutron source was placed 68 mm away the HPGe crystal centerline.*

The neutron damage experiment was designed to track energy resolution degradation at various neutron fluences. This was accomplished by first measuring the detector's energy resolution prior to irradiation. A Co-60 gamma-ray source was placed in a holder 25 cm away from the face of the HPGe detector and a gamma-ray measurement was performed. Note that cryostat design dictated that the encapsulated detector be mounted so that the open end of the crystal's coaxial well faced the gamma-ray source. DSPEC 50 trapezoidal rise time and width parameters were 14 μs an 1 μs, respectively. This long shaping time was used to mitigate high-frequency noise visible in the preamplifier output. After the gamma-ray measurement was complete, the PuB source was placed next to the detector, as shown in Figure 3.21. After multiple hours of irradiation, the PuB source was removed, neutron irradiation time was documented, and another gamma-ray measurement was performed using the same shaping parameters as the initial measurement. This process was repeated until the detector was exposed to a PuB neutron fluence $>10^{10}$ cm^{-2}. The encapsulated crystal was maintained at 99 K and was biased at 3 kV throughout the irradiation experiment. Table 3.2 shows measurement details.

GRS energy resolution degradation was observed by monitoring the structure of the 1333 keV photopeak from Co-60 decay. Peaks were fit with a Gaussian, an exponentially-modified Gaussian, and a step function. Gaussian fitting is commonly used to fit gamma-ray spectra, but an exponentially-modified Gaussian function was needed to account for low-energy tailing associated with radiation damage. The step function subtracts background from the full-energy peak. All gamma-ray measurements had less than 10% dead time.

3.5.1.2 Radiation Damage Repair

Annealing was performed in stages so energy resolution performance and photopeak efficiency could be correlated to cumulative annealing time. Prior to annealing, the LN dipstick cryostat was removed from the LN dewar and connected to a turbo molecular pump via a valve and $\sim$1 m long vacuum bellows. Active pumping ensured that the gas load generated during annealing was extracted from the cryostat. Once the detector passively warmed to room temperature, a temperature controller was used to supply power to an anneal heater that was connected to the encapsulated detector. The controller utilized temperature feed-

Table 3.2: *Neutron Radiation Damage Measurements*

Measurement	Total irradiation time [hr]	Total fluence [cm^{-2}]	Live time [s]
1	0	0	300
2	18.95	$6{\times}10^8$	300
3	42.45	$1.4{\times}10^9$	300
4	61.92	$2.1{\times}10^9$	300
5	88.42	$3.0{\times}10^9$	300
6	155.92	$5.3{\times}10^9$	300
7	171.10	$5.8{\times}10^9$	300
8	193.63	$6.5{\times}10^9$	300
9	220.45	$7.4{\times}10^9$	300
10	314.23	$1.06{\times}10^{10}$	600
11	330.60	$1.11{\times}10^{10}$	600
12	358.12	$1.21{\times}10^{10}$	600
13	407.20	$1.37{\times}10^{10}$	600

back to maintain the crystal at 378 +/- 0.5 K. This temperature was maintained for the duration of the anneal. The experimental setup used for annealing the detector is shown in Figure 3.22. After the anneal was complete, the anneal heater was deactivated, anneal duration was documented, and the encapsulated detector passively cooled to room temperature. The valve was then closed and the dipstick cryostat was inserted into the LN Dewar. Once the detector cooled to 99 K, it was biased to 3 kV and a Co-60 gamma-ray measurement was performed to determine energy resolution and photopeak efficiency. Pulse processing parameters and gamma-ray source location were identical to those discussed in Section 3.5.1.1 and dead time did not exceed 10%. This process was repeated multiple times, with gamma-ray measurements performed after each anneal. Table 3.3 summarizes these measurements.

Table 3.3: *Anneal Measurements*

Measurement	Cumulative anneal time [hr]	Live time [s]
1A	85.8	4400
2A	181.8	16014
3A	277.1	4200
4A	373.1	11400
5A	495.6	18000

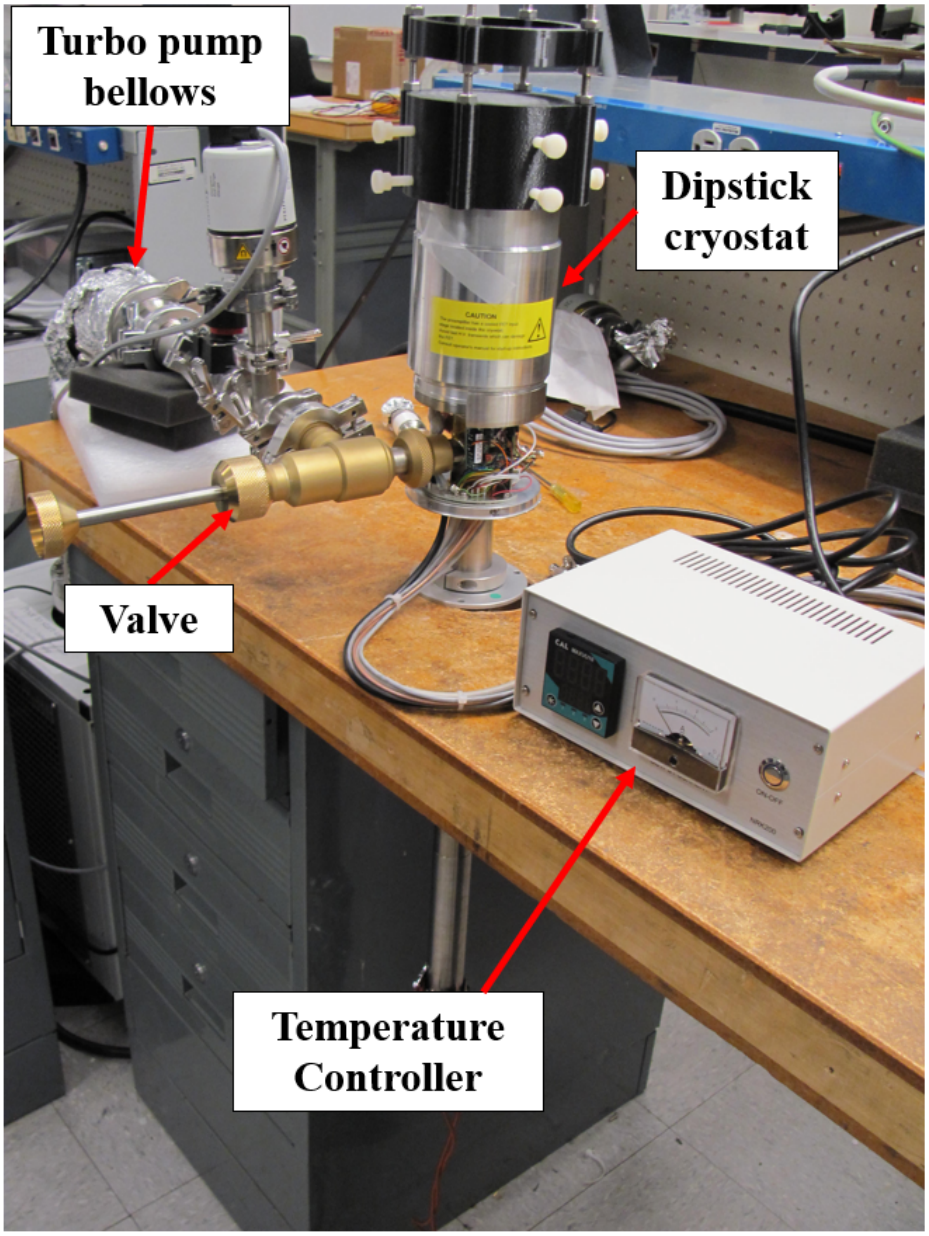

Figure 3.22: *Annealing setup. A temperature controller was used to maintain detector temperature at 378+/-0.5 K during annealing. A turbo pump was connected to the dipstick cryostat via a valve and was used extract excess outgassing produced by heating internal components.*

3.5.2 Results from Radiation Damage and Annealing Experiments

Figure 3.23 shows measured Co-60 gamma-ray spectra at multiple neutron fluence levels. The photopeak measured prior to radiation damage shows no low-energy tailing. However, tailing becomes apparent as neutron fluence increases.

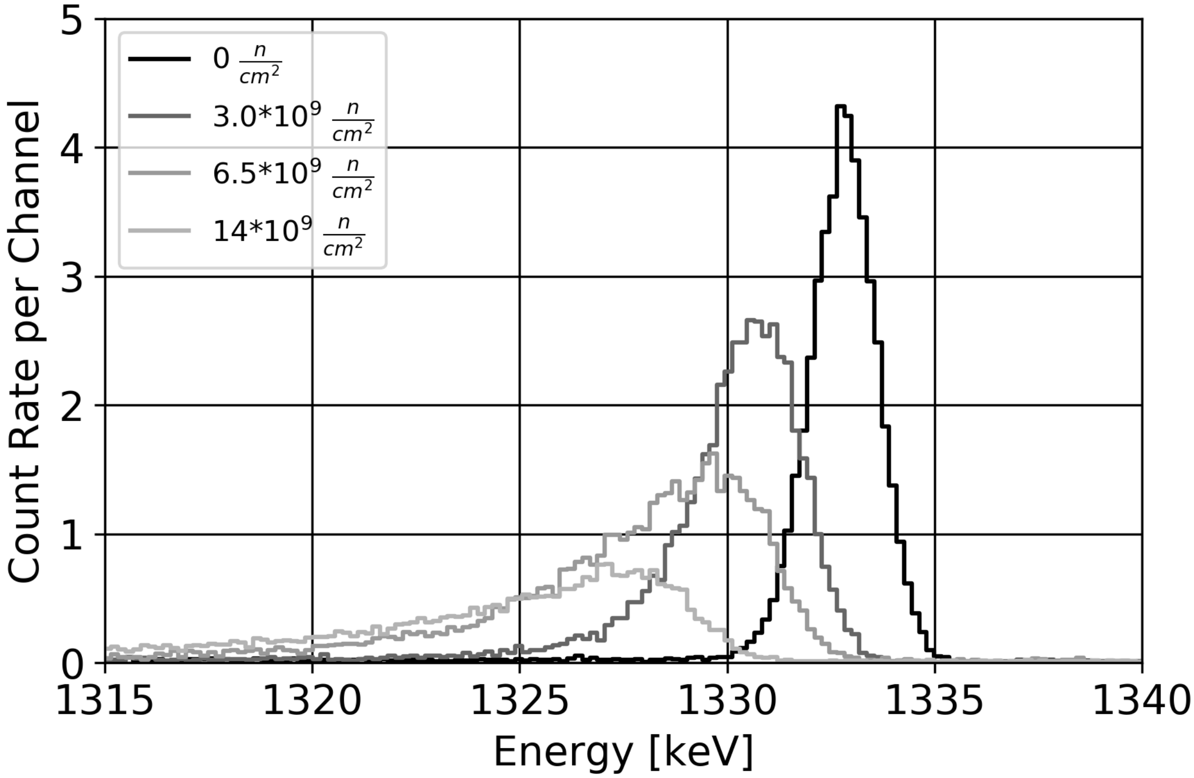

Figure 3.23: *1333 keV Co-60 photopeak at various neutron fluences. Measurements shown in this figure correspond to measurements 1, 5, 8, and 13 (from right to left) listed in Table 3.2. Photopeak measurements performed with the radiation-damaged detector exhibit significant low-energy tailing due to charge trapping.*

HPGe resolution degradation due to neutron damage was quantified by observing the structure of the 1333 keV photopeak from Co-60 decay. Figure 3.24 shows FWHM energy resolution measurements at multiple neutron fluences. Fitting parameters used to fit the data are located in Appendix D. Due to the non-Gaussian shape peak shapes measured with the radiation damaged detector, the FWHM values reported here can not be used to quantify statistical spread in measured data (as is the case for normally-distributed data). Rather, they simply indicate the width of the photopeak at one half its maximum value. FWHM was determined by interpolating the function used to fit the data.

Complete restoration of detector energy resolution was accomplished through long-duration annealing at 378 K. Figure 3.25 shows measured FWHM and full width tenth maximum

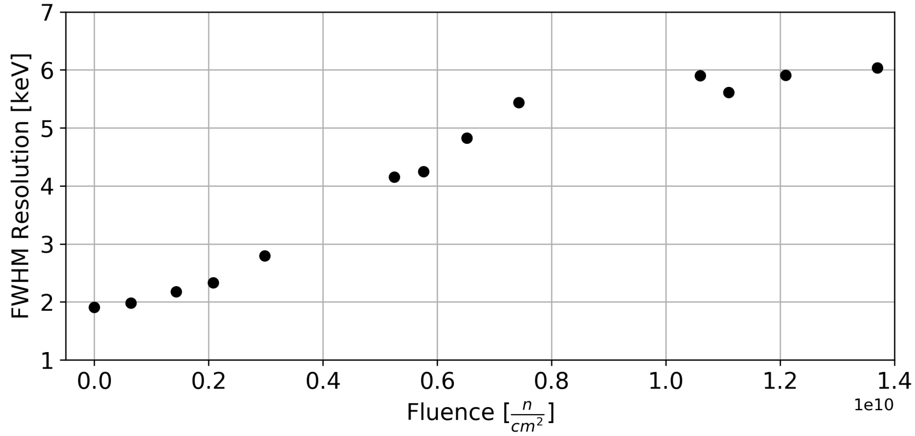

Figure 3.24: *Energy resolution versus neutron fluence. The GRS energy resolution was severely degraded due to fast neutrons. GRS energy resolution was characterized at multiple neutron fluences.*

(FWTM) values corresponding to multiple anneal times. Data shown at time = 0 correspond to measurement 13 in Table 3.2 and all other data came from measurements listed in Table 3.3. Fitting parameters used to analyze this data are located in Appendix D.

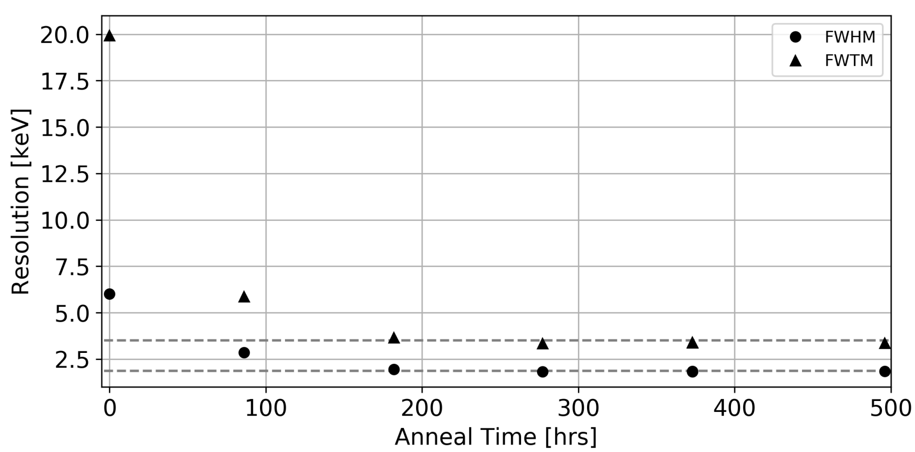

Figure 3.25: *Energy resolution recovery from annealing. GRS spectral performance was documented at various anneal times by monitoring FWHM and FWTM energy resolution for the 1333 keV Co-60 full-energy peak. Full GRS spectral performance was restored after annealing the detector at 378 K for 280 hours. The upper and lower horizontal dashed lines indicate FWTM and FWHM energy resolution, respectively, prior to radiation damage.*

Detector efficiency was also monitored throughout annealing. Figure 3.26 shows 1333 keV photopeak areas at different anneal times. Source-detector placement was constant throughout these measurements and change in Co-60 activity due to radioactive decay was considered. The measurement shown at time = 0 was performed before the detector was exposed to the neutron source (measurement 1 in Table 3.2) and other data correspond to Table 3.3. All data was normalized to the initial measurement.

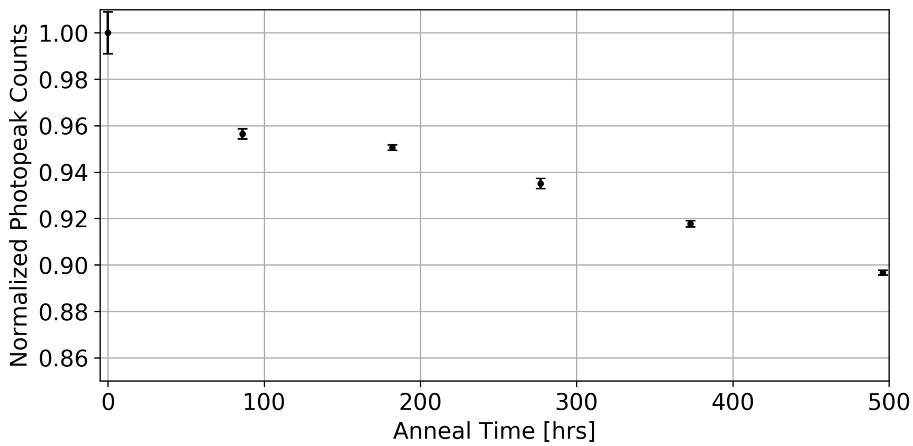

Figure 3.26: *Effect of annealing on photopeak efficiency. The Dragonfly HPGe crystal was annealed for approximately 500 hours and Co-60 gamma-ray measurements were performed intermittently to quantify efficiency loss due to annealing. The leftmost measurement was measured with the undamaged detector (measurement 1 in Table 3.2). It has a larger uncertainty in comparison to the other measurements due to shorter measurement time.*

3.5.3 Interpretation of Radiation Damage and Annealing Experiments

Data presented in Figure 3.23 show that radiation damage results in a decrease in full-energy peak centroid and low-energy tailing. The radiation damage simulation discussed in Section 2.3 predicted both of these outcomes by modeling hole trapping in coaxial HPGe detectors. This indicates that the physics behind resolution degradation shown in Figure 3.23 are understood and that results produced in this work align with expectations. There are some differences between full-energy peak shapes predicted by the simulation and measured in this work. This is not unexpected, as the model is built upon simplifying assumptions (see Appendix A.2) and uses parameters that can vary between experiments. Future work could use data presented in this work to increase the accuracy of the model.

At the time of this writing, the Dragonfly rotorcraft layout has not been finalized. While the separation distance between the GRS and MMRTG has been estimated to be 200 cm, shielding between the two components is not well known. With respect to radiation damage, a conservative estimate of resolution degradation due to the MMRTG can be made by assuming no shielding between the GRS and MMRTG. Using the MMRTG neutron activity discussed in Section 2.3 and an assumption of inverse distance-squared flux dependence[8], the MMRTG neutron flux at the GRS can be estimated to be ~48 $[cm^{-2} * s^{-1}]$. This corresponds to a MMRTG mission neutron fluence of $\sim 5 \times 10^9\ cm^{-2}$. Data shown in Figure 3.24 indicates that FWHM resolution corresponding to this neutron fluence is near the 4.2 keV FWHM instrument requirement. Neutron damage from the DT neutron generator and the possibility of a mission extension increase GRS radiation damage. Hence, this conservative estimate indicates that a surface anneal would likely be needed on Titan's surface to restore detector energy resolution performance. It should also be mentioned that, while the PuB source has a similar neutron energy spectrum to that of a MMRTG, its average neutron energy is higher (2.9 vs. 2.3 MeV). Previous studies indicate that this difference makes PuB radiation damage slightly more damaging than the MMRTG.[61;63;68] Hence, data shown in Figure 3.24 overestimates GRS energy resolution degradation due to MMRTG neutrons.

Future work should include a less conservative, more precise prediction of GRS spectral performance during surface operations. This requires resolution degradation results presented in this work to be supplemented with simulations. APL has developed a GEANT4 model that calculates the neutron environment at the GRS mounting location on the Dragonfly rotorcraft. Neutron shielding due to material between the GRS and MMRTG and neutron contributions from the MMRTG, neutron generator, and reflection from the environment are being considered. Simulations are ongoing, as uncertainties in lander layout and material have prevented results from being finalized. Results will be used to inform GRS development and operations on Titan's surface, as neutron shielding and downscattering may reduce GRS radiation damage and eliminate the need to anneal the detector on Titan's surface. This would allow GRS design to be simplified and would reduce GRS downtime during surface operations.

Accurate prediction of GRS spectral performance during surface operations also requires a precise estimate of detector temperature on Titan. As indicated in Figure 3.9, the steady-state crystal temperature on Titan is a function heat transfer from the rotorcraft via the mounting bracket and electrical harness. Since the amount of energy resolution degradation exhibited by a radiation-damaged HPGe detector is temperature dependent[67], accurate estimation of GRS temperature on Titan is critical to predicting spectral performance. Data shown in this work correspond to a detector operated at 99 K, or 5 K above Titan's ambient temperature. More radiation damage measurements should be performed if refined estimates of the Dragonfly GRS operation temperature exceed 99 K.

Results from the annealing measurement indicate that resolution degradation corresponding to a fast neutron fluence of approximately 1.4 $\times 10^{10}$ cm^{-2} can be repaired by annealing the detector at 378 K for 277 hours. This result provides an upper bound for annealing duration during surface operations on Titan, as it is very unlikely that the detector will incur neutron fluence greater than 1.4×10^{10} cm^{-2}, even if the mission is extended by a factor of two. Detector annealing continued after spectral performance was restored in order to track efficiency loss. This effect is believed to be due to diffusion of lithium from the n-contact into the bulk of the germanium.[7] Efficiency loss shown in Figure 3.26 indicates the need to carefully plan Dragonfly GRS anneals. Of particular concern is the cruise anneal that is scheduled to be performed in space prior to the rotorcraft being deployed onto Titan. The purpose of this anneal is to repair radiation damage that the GRS incurs from MMRTG neutrons and cosmic rays during travel between Earth and Titan. Due to the GRS's passively-cooled thermal design, the effectiveness of the orbit anneal will not be determined until the rotorcraft is deployed onto Titan's surface and the GRS cools to operating temperature. If the cruise anneal duration was not sufficient to restore GRS energy resolution, then a surface anneal will be required. This should be avoided because it would delay measurements on Titan's surface. The probability of successfully repairing the detector during cruise can be increased by extending the duration of the cruise anneal. This work indicates that one drawback to this strategy is GRS efficiency loss. Future work should develop an annealing recipe that balances these considerations. One strategy would be to utilize a monitor that characterizes the radiation environment onboard the Dragonfly spacecraft during cruise. Data from this system could be used by mission planners to determine the duration of the cruise anneal.

The annealing experiment ensured that the Dragonfly encapsulated detectors are compatible with long-duration anneals. The commercial version of these detectors are not typically radiation damaged as severely as is expected for the Dragonfly mission. Normal practice is to anneal them for ∼ten of hours[51], while the Dragonfly GRS will potentially need to be annealed for hundreds of hours. This difference was concerning as annealing increases gas load inside the hermetically-sealed detector encapsulation and forces the getter to capture more gas. If the getter is unable to maintain vacuum, pressure inside the encapsulation could increase and cause high voltage breakdown and/or leakage current. The anneal study presented in this work showed that the encapsulated detector could be annealed for ∼500 hours at 105°C without any resolution degradation or high-voltage breakdown.

Chapter 4

Conclusion

The Dragonfly HPGe gamma-ray spectrometer will be sent roughly one-billion miles from Earth to investigate the icy moon Titan. The system must survive intense vibration from rocket launch, operate in Titan's unique thermal environment, and perform high-resolution gamma-ray spectroscopy on Titan's surface. Additionally, the system must be able to repair radiation damage incurred throughout the mission.

This work characterized the development model Dragonfly GRS to show that the system can meet mission requirements. It was subjected to generic rocket launch vibration loads, then checked for damage. Subsequent testing indicated that the system did not incur mechanical damage or energy resolution degradation. The GRS was shown to meet passive cooling and annealing thermal objectives through testing in an environmental chamber that mimicked Titan conditions. A thermal model was developed and benchmarked using experimental data, and allows detector thermal performance to be simulated when it is subjected to various conditions. This ability is critical to GRS development, as thermal boundary conditions are not finalized. Thermal implications from changes in the GRS-rotorcraft mounting method or updated estimates of the Titan convection coefficient can be quickly estimated with the model presented in this work.

The development model GRS was designed to be annealed for 5 W or less during operations on Titan's surface. Accomplishing a low-power anneal requires that the cryostat be vacuum evacuated. This work extensively characterized the vacuum condition inside the cryostat. Gas load was measured to be 9 $\times 10^{-9}$ $[mbar * liter * s^{-1}]$ and the major gasses comprising GRS gas load were H_2, CO, and CO_2. A SAES D100 getter was shown to be able to maintain vacuum inside the cryostat for ~160 days. The finite nature of getter pumping prevents the 160-day vacuum hold time measurement from being extrapolated to predict multi-year vacuum performance. Longer duration testing should be performed in the future to better estimate how frequently the getter will need to be reactivated during the mission. Additionally, the getter's inability to capture methane poses a risk for operation on Titan's surface, as Titan's atmosphere contains 5% methane.

Future vacuum work should include investigating UHV-compatible replacements for PTFE components. RGA scans indicated that fluorine, a constituent of PTFE, is present in the system. Reduction of this material may reduce system gas load. Additionally, performing higher-AMU scans would help investigate sources of the >44 AMU fragments apparent in RGA scans and would help guide efforts to reduce gas load. Other vacuum maintenance strategies should also be investigated for the Dragonfly GRS. One potential option involves using a small valve to vent the cryostat to space vacuum during cruise. This guarantees that GRS vacuum will be sufficient to facilitate a low-power cruise anneal. Just before being deployed into Titan's atmosphere, the valve would be closed and system vacuum would be maintained with a molecular sieve, such a zeolite. This strategy is being actively considered as of this writing.

Measurements indicate that the GRS is capable of measuring high-resolution gamma-ray spectra using a custom, APL-developed charge-integrating preamplifier. Resolution measurements were shown to be better than 4.2 keV FWHM for 1332 keV gamma rays, indicating that the system meets specifications. The GRS was also shown to be sensitive to gamma rays from neutron interactions expected on Titan, including neutron capture interactions with chlorine and hydrogen and inelastic scatter interactions with sodium.

Future work should include refining amplifier design, as analysis indicated that electronic noise was the main contributor to GRS energy resolution. This work is non-trivial, as all amplifier components must be flight rated and cryogenically compatible. Future amplifier testing should be conducted in an environmental chamber rather than liquid nitrogen. This would be more representative of Titan's thermal environment.

The Dragonfly GRS will be exposed to multiple sources of radiation damage, including cosmic rays and neutrons from the MMRTG and DT neutron generator, that will degrade energy resolution performance. GRS energy resolution degradation due to MMRTG neutron radiation damage was investigated by exposing a Dragonfly detector to neutrons from a PuB source. This source has a similar neutron energy spectrum and average energy to that of a MMRTG. Spectral measurements were performed throughout the experiment, allowing energy resolution to be documented at multiple neutron fluences.

Results indicate that a MMRTG would likely degrade the Dragonfly GRS energy resolution past specifications during surface operations *if the MMRTG has direct line of sight to the GRS*. However, materials inside the Dragonfly rotorcraft will undoubtedly shield and downscatter MMRTG neutrons before they interact with the HPGe crystal. Simulations are in progress to investigate the extent of this effect. In addition to shielding, simulations should also consider neutrons from the DT neutron generator, MMRTG, and reflection off of Titan's surface.

Repair of the neutron-damaged detector was investigated in this work, leading to three important conclusions. First, a Dragonfly encapsulated that was exposed to a neutron fluence of $1.4\times10^{10}\ cm^{-2}$ was able to recover full energy resolution performance after 280 hours of annealing at 378 K. This provides an upper bound for annealing time on Titan's surface, as this fluence is significantly higher than what is expected during surface operations. Second, detector efficiency loss was monitored throughout a 500-hour anneal, allowing for a correlation between anneal duration and efficiency loss. This data is useful for planning the cruise anneal, which will occur just prior to the rotorcraft being deployed onto Titan's surface.

It also indicates the need to optimize annealing recipes to fully restore detector resolution performance in the shortest time possible. Lastly, the long-duration annealing experiment indicated that the encapsulated detector vacuum design is compatible with hundreds of hours of annealing. This is an important result, as it was unknown if the encapsulation getter could handle the increased gas load associated with long-duration anneals.

Bibliography

[1] Jet Propulsion Laboratory. Titan's north. Accessed Apr. 18, 2022 [Online].

[2] European Space Agency. Disr image of titan's surface. Accessed Apr. 18, 2022 [Online].

[3] Jason W Barnes, Elizabeth P Turtle, Melissa G Trainer, Ralph D Lorenz, Shannon M MacKenzie, William B Brinckerhoff, Morgan L Cable, Carolyn M Ernst, Caroline Freissinet, Kevin P Hand, et al. Science goals and objectives for the dragonfly titan rotorcraft relocatable lander. *The Planetary Science Journal*, 2(4):130, 2021.

[4] Thomas Prettyman, Arnold Burger, Naoyuki Yamashita, James Lambert, Keivan Stassun, and Carol Raymond. Ultra-bright scintillators for planetary gamma-ray spectroscopy. *SPIE Newsroom*, 2015.

[5] WC Feldman, BL Barraclough, KR Fuller, DJ Lawrence, S Maurice, MC Miller, TH Prettyman, and AB Binder. The lunar prospector gamma-ray and neutron spectrometers. *Nuclear Instruments and Methods in Physics Research Section A: Accelerators, Spectrometers, Detectors and Associated Equipment*, 422(1-3):562–566, 1999.

[6] Nobuyuki Hasebe, Eido Shibamura, Takashi Miyachi, Takeshi Takashima, Masanori Kobayashi, Osamu Okudaira, Nana Yamashita, Shingo Kobayashi, Yuzuru Karouji, Makoto Hareyama, Satoshi Kodaira, Kanako Hayatsu, Kazuya Iwabuchi, Shinpei Nemoto, Kunitomo Sakurai, Shinichi Komatsu, Mitsuhiro Miyajima, Mitsuru Ebihara, Takeshi Hihara, and Robert Reedy. High performance germanium gamma-ray spectrometer on lunar polar orbiter selene (kaguya). *Transactions of Space Technology Japan*, 7, 01 2010.

[7] Patrick N Peplowski, Morgan Burks, John O Goldsten, Samuel Fix, Lena E Heffern, David J Lawrence, and Zachary W Yokley. Radiation damage and annealing of three coaxial n-type germanium detectors: preparation for spaceflight missions to asteroid 16 psyche and mars' moon phobos. *Nuclear Instruments and Methods in Physics Research Section A: Accelerators, Spectrometers, Detectors and Associated Equipment*, 942:162409, 2019.

[8] Mojtaba Taherzadeh and Peter J Gingo. Neutron radiation characteristics of plutonium dioxide fuel. *Nuclear Technology*, 15(3):396–410, 1972.

[9] Michael BR Smith. Radioisotope power source dose estimation tool (rps-det). In *2018 IEEE Aerospace Conference*, pages 1–19. IEEE, 2018.

[10] IC Gauld, EF Shores, and RT Perry. New neutron source algorithms in the origen-s code. In *Proc. of American Nuclear Society 2002 Winter Meeting" Building the World Nuclear Community–Strategies for the Deployment of New Nuclear Technologies*, pages 17–21. Citeseer, 2002.

[11] Th Kröll, I Peter, Th W Elze, J Gerl, Th Happ, M Kaspar, H Schaffner, S Schremmer, R Schubert, K Vetter, et al. Analysis of simulated and measured pulse shapes of closed-ended hpge detectors. *Nuclear Instruments and Methods in Physics Research Section A: Accelerators, Spectrometers, Detectors and Associated Equipment*, 371(3):489–496, 1996.

[12] Ulrich Piesbergen. Die durchschnittlichen atomwärmen der aiii bv-halbleiter alsb, gaas, gasb, inp, inas, lnsb und die atomwärme des elements germanium zwischen 12 und 273°k. *Zeitschrift für Naturforschung A*, 18(2):141–147, 1963.

[13] Randall F Barron and Gregory F Nellis. *Cryogenic Heat Transfer*. CRC Press, 2 edition, 2016.

[14] Ralph D Lorenz, Elizabeth P Turtle, Jason W Barnes, Melissa G Trainer, Douglas S Adams, Kenneth E Hibbard, Colin Z Sheldon, Kris Zacny, Patrick N Peplowski, David J Lawrence, et al. Dragonfly: A rotorcraft lander concept for scientific exploration at titan. *Johns Hopkins APL Technical Digest*, 34(3):14, 2018.

[15] Ann M Parsons. Review of nuclear techniques for planetary science. In *International Journal of Modern Physics: Conference Series*, volume 50, page 2060004. World Scientific, 2020.

[16] AM Demidov, LI Govor, Yu K Cherepantsev, MR Ahmed, S Al-Najjar, MA Al-Amili, N Al-Assafi, and N Rammo. Atlas of gamma-ray spectra from the inelastic scattering of reactor fast neutrons. *Moscow: Atomizdat*, 1978.

[17] IAEA Prompt Gamma ray Neutron Activation Analysis. Online Database.

[18] IAEA X-ray, Gamma ray Decay Data Standards for Detector Calibration, and Other Applications. Online Database.

[19] Douglas S. McGregor and Kenneth J. Shultis. *Radiation Detection Concepts, Methods, and Devices*. CRC Press, 1 edition, 2021.

[20] Glenn Frederick Knoll. *Radiation detection and measurement*. John Wiley & Sons, 3 edition, 2000.

[21] David M Smith, RP Lin, P Turin, DW Curtis, JH Primbsch, RD Campbell, R Abiad, P Schroeder, CP Cork, EL Hull, et al. The rhessi spectrometer. In *The Reuven Ramaty High-Energy Solar Spectroscopic Imager (RHESSI)*, pages 33–60. Springer, 2003.

[22] G Vedrenne, J-P Roques, V Schönfelder, P Mandrou, GG Lichti, A Von Kienlin, B Cordier, S Schanne, J Knödlseder, G Skinner, et al. SPI: The spectrometer aboard INTEGRAL. *Astronomy & Astrophysics*, 411(1):L63–L70, 2003.

[23] WA Mahoney, JC Ling, AS Jacobson, and RM Tapphorn. The heao 3 gamma-ray spectrometer. *Nuclear Instruments and Methods*, 178(2-3):363–381, 1980.

[24] Naoyuki Yamashita, Nobuyuki Hasebe, Eido Shibamura, Takashi Miyachi, Takeshi Takashima, Masanori Kobayashi, Osamu Okudaira, Shingo Kobayashi, Makoto Hareyama, Yuzuru Karouji, et al. Germanium gamma-ray spectrometer on selene (kaguya). *Journal of the Physical Society of Japan*, 78(Suppl. A):153–156, 2009.

[25] WV Boynton, JI Trombka, WC Feldman, JR Arnold, PAJ Englert, AE Metzger, RC Reedy, SW Squyres, H Wänke, SH Bailey, et al. Science applications of the mars observer gamma ray spectrometer. *Journal of Geophysical Research: Planets*, 97(E5):7681–7698, 1992.

[26] WV Boynton, WC Feldman, IG Mitrofanov, LG Evans, RC Reedy, SW Squyres, R Starr, JI Trombka, C d'Uston, JR Arnold, et al. The mars odyssey gamma-ray spectrometer instrument suite. *Space Science Reviews*, 110(1):37–83, 2004.

[27] John O Goldsten, Edgar A Rhodes, William V Boynton, William C Feldman, David J Lawrence, Jacob I Trombka, David M Smith, Larry G Evans, Jack White, Norman W Madden, et al. The messenger gamma-ray and neutron spectrometer. In *The Messenger Mission to Mercury*, pages 339–391. Springer, 2007.

[28] DJ Lawrence, MT Burks, M Cully, LT Elkins-Tanton, JO Goldsten, I Jun, TJ McCoy, PN Peplowski, CA Polanskey, TH Prettyman, et al. The psyche gamma-ray and neutron spectrometer: Update on instrument design and measurement capabilities. In *50th Annual Lunar and Planetary Science Conference*, number 2132, page 1554, 2019.

[29] David J Lawrence, PN Peplowski, AW Beck, MT Burks, NL Chabot, RC Elphic, CM Ernst, JO Goldsten, SL Murchie, and T Usui. The mars-moon exploration with gamma rays and neutrons (megane) investigation for the martian moon exploration

(mmx) mission. In *49th Annual Lunar and Planetary Science Conference*, number 2083, page 2121, 2018.

[30] MG Trainer, WB Brinckerhoff, C Freissinet, DJ Lawrence, PN Peplowski, AM Parsons, K Zacny, EP Turtle, JW Barnes, RD Lorenz, et al. Dragonfly: investigating the surface composition of titan. In *Lunar andPlanetary Science Conference*, number GSFC-E-DAA-TN53846, 2018.

[31] Nicholas Tsoulfidis. *Measurement and Detection of Radiation*. CRC Press, 4 edition, 2015.

[32] DL Upp, RM Keyser, and TR Twomey. New cooling methods for hpge detectors and associated electronics. *Journal of radioanalytical and nuclear chemistry*, 264(1):121–126, 2005.

[33] Morgan T Burks, Owen B Drury, John O Goldsten, Lisle B Hagler, Lena E Heffern, Nathan R Hines, Geon-Bo Kim, David J Lawrence, Karl E Nelson, Patrick N Peplowski, et al. Gemini: A high-resolution, low-resource, gamma-ray spectrometer for planetary science applications. *Space Science Reviews*, 216(7):1–23, 2020.

[34] PW Martin. Gamma-ray yields from inelastic neutron scattering of 14.1 mev neutrons from sodium, magnesium, silicon, sulphur, manganese and iron. *J. Nucl. Energy Parts A/B*, 19:447, 1965.

[35] J Eberth and J Simpson. From ge (li) detectors to gamma-ray tracking arrays–50 years of gamma spectroscopy with germanium detectors. *Progress in Particle and Nuclear Physics*, 60(2):283–337, 2008.

[36] Andreas Wiens, Herbert Hess, Benedikt Birkenbach, Bart Bruyneel, Jürgen Eberth, Daniel Lersch, Gheorghe Pascovici, Peter Reiter, Heinz-Georg Thomas, Agata Collaboration, et al. The agata triple cluster detector. *Nuclear Instruments and Methods*

in Physics Research Section A: Accelerators, Spectrometers, Detectors and Associated Equipment, 618(1-3):223–233, 2010.

[37] J. Eberth, H.G. Thomas, P.v. Brentano, R.M. Lieder, H.M. Jäger, H. Kämmerfing, M. Berst, D. Gutknecht, and R. Henck. Encapsulated ge detectors: Development and first tests. *Nuclear Instruments and Methods in Physics Research Section A: Accelerators, Spectrometers, Detectors and Associated Equipment*, 369(1):135–140, 1996.

[38] Teledyne Reynolds. *Series 600 HV Feedthrough Specifications*.

[39] Winchester Interconnect. *Micro-D Connectors*, 2019.

[40] Marc Trubert. Mass acceleration curve for spacecraft structural design. Technical Report JPL D - 5882, 1989.

[41] Smalley. *Smalley SSR-0375*, 2021.

[42] J.O. Goldsten, E.A. Rhodes, W.V. Boynton, W.C. Feldman, D.J. Lawrence, J.I. Trombka, D.M. Smith, L.G. Evans, J. White, N.W. Madden, P.C. Berg, G.A. Murphy, R.S. Gurnee, K. Strohbehn, B.D. Williams, E.D. Schaefer, C.A. Monaco, C.P. Cork, J.D. Eckels, W.O. Miller, M.T. Burks, L.B. Hagler, S.J. DeTeresa, and M.C. Witte. The messenger gamma-ray and neutron spectrometer. *Space Science Reviews*, 131:162409, 2019.

[43] DJ Lawrence, MT Burks, M Cully, LT Elkins-Tanton, JO Goldsten, I Jun, TJ McCoy, PN Peplowski, CA Polanskey, TH Prettyman, et al. The psyche gamma-ray and neutron spectrometer: Update on instrument design and measurement capabilities. In *Lunar and Planetary Science Conference*, number 2132, page 1554, 2019.

[44] David J Lawrence, Patrick N Peplowski, Andrew W Beck, Morgan T Burks, Nancy L Chabot, Michael J Cully, Richard C Elphic, Carolyn M Ernst, Samuel Fix, John O

Goldsten, et al. Measuring the elemental composition of phobos: The mars-moon exploration with gamma rays and neutrons (megane) investigation for the martian moons exploration (mmx) mission. *Earth and Space Science*, 6(12):2605–2623, 2019.

[45] Valeria Cottini, Conor A Nixon, Donald E Jennings, Remco de Kok, Nicholas A Teanby, Patrick GJ Irwin, and F Michael Flasar. Spatial and temporal variations in titan's surface temperatures from cassini cirs observations. *Planetary and Space Science*, 60(1):62–71, 2012.

[46] Ralph D Lorenz. Thermal interactions of the huygens probe with the titan environment: Constraint on near-surface wind. *Icarus*, 182(2):559–566, 2006.

[47] Frank P Incropera, David P DeWitt, Theodore Bergman, and Adrienne Lavine. *Fundamentals of heat transfer*. Wiley, 6 edition, 2016.

[48] SAES Group. *St 171 and 172 Sintered Porous Getters*, 1994.

[49] A Roth. *Vacuum Technology*. North-Holland, 3 edition, 1990.

[50] SAES Group. *St 175 - Sintered Porous Getters*.

[51] Jurgen Eberth. personal communication.

[52] SAES Group. *CapaciTorr D 50, D 100, D 200*.

[53] Ishwar Niraula. Email correspondence with ishwar niraula, saes applications engineer. personal communication, 2022.

[54] J-F Mariscal, Nicolas Rouanet, J-L Maria, Benjamin Lustrement, Emmanuel Bertran, Christophe Montaron, Gabriel Guignan, Aurélie Reberac, Eric Quémerais, P Zuppella, et al. Phebus uv spectrometer on board esa-bepicolombo mission: Instrument design & performance results. In *International Conference on Space Optics—ICSO 2018*, volume 11180, page 111802T. International Society for Optics and Photonics, 2019.

[55] LATMOS. *D400-2 (St172) getter vibration test report*, 2016.

[56] C Benjamin Nakhosteen and Karl Jousten. *Handbook of vacuum technology*. John Wiley & Sons, 2016.

[57] Rebecca Grinham and Dr Andrew Chew. A review of outgassing and methods for its reduction. *Applied Science and Convergence Technology*, 26(5):95–109, 2017.

[58] HC Hseuh and Xiuhua Cui. Outgassing and desorption of the stainless-steel beam tubes after different degassing treatments. *Journal of Vacuum Science & Technology A: Vacuum, Surfaces, and Films*, 7(3):2418–2422, 1989.

[59] L Fabris, NW Madden, and H Yaver. A fast, compact solution for low noise charge preamplifiers. *Nuclear Instruments and Methods in Physics Research Section A: Accelerators, Spectrometers, Detectors and Associated Equipment*, 424(2-3):545–551, 1999.

[60] Ametek Advanced Measurement Technology. Preamplifier introduction. Technical report, 2009.

[61] HW Kraner. Fast neutron damage in germanium detectors. *IEEE Transactions on Nuclear Science*, 27(1):217–234, 1980.

[62] Lawrence S Darken Jr, Rex C Trammell, Thomas W Raudorf, Richard H Pehl, and Jack H Elliott. Mechanism for fast neutron damage of ge (hp) detectors. *Nuclear Instruments and Methods*, 171(1):49–59, 1980.

[63] Ethan L Hull. *Charge Collection Physics in Germanium Detectors*. PhD thesis, Indiana University, 1998.

[64] HW Kraner, C Chasman, and KW Jones. Effects produced by fast neutron bombardment of ge (li) gamma ray detectors. *Nuclear Instruments and Methods*, 62(2):173–183, 1968.

[65] Richard H Pehl, Norman W Madden, Jack H Elliott, Thomas W Raudorf, Rex C Trammell, and Lawrence S Darken. Radiation damage resistance of reverse electrode ge coaxial detectors. *IEEE Transactions on Nuclear Science*, 26(1):321–323, 1979.

[66] C DeW Van Siclen, EH Seabury, CJ Wharton, and AJ Caffrey. Phenomenological model for predicting the energy resolution of neutron-damaged coaxial hpge detectors. *IEEE Transactions on Nuclear Science*, 59(5):2487–2493, 2012.

[67] EH Seabury, C Dew Van Siclen, JB McCabe, CJ Wharton, and AJ Caffrey. Neutron damage in mechanically-cooled high-purity germanium detectors for field-portable prompt gamma neutron activation analysis (pgnaa) systems. In *2013 IEEE Nuclear Science Symposium and Medical Imaging Conference (2013 NSS/MIC)*, pages 1–4. IEEE, 2013.

[68] V Borrel, B Kandel, F Albernhe, P Frabel, B Cordier, G Tauzin, S Crespin, R Coszach, JM Denis, and Pierre Leleux. Fast neutron-induced damage in integral n-type hpge detectors. *Nuclear Instruments and Methods in Physics Research Section A: Accelerators, Spectrometers, Detectors and Associated Equipment*, 430(2-3):348–362, 1999.

[69] Thomas W Raudorf, Rex C Trammell, Sanford Wagner, and Richard H Pehl. Performance of reverse electrode hpge coaxial detectors after light damage by fast neutrons. *IEEE Transactions on Nuclear Science*, 31(1):253–257, 1984.

[70] HG Thomas, J Eberth, F Becker, T Burkardt, S Freund, U Hermkens, T Mylaeus, S Skoda, W Teichert, A vd Werth, et al. Neutron induced radiation damage of a n-type ge detector influence of the operating temperature. *Nuclear Instruments and Methods in Physics Research Section A: Accelerators, Spectrometers, Detectors and Associated Equipment*, 332(1-2):215–219, 1993.

[71] Lawrence S Darken, Rex C Trammell, Thomas W Raudorf, and Richard H Pehl. Neutron

damage in ge (hp) coaxial detectors. *IEEE Transactions on Nuclear Science*, 28(1):572–578, 1981.

[72] B Kandel, V Borrel, F Albernhe, P Frabel, B Cordier, G Tauzin, S Crespin, R Coszach, JM Denis, and Pierre Leleux. Influence of temperature on the behaviour of integral n-type hpge detectors irradiated with fast neutrons. *Nuclear Instruments and Methods in Physics Research Section A: Accelerators, Spectrometers, Detectors and Associated Equipment*, 430(2-3):363–372, 1999.

[73] M Edward Anderson. Neutron flux, spectrum, and dose equivalent measurements for a 4500-w (th)/sup 238/puo/sub 2/general purpose heat source. Technical report, Monsanto Research Corp., Miamisburg, OH (USA). Mound, 1985.

[74] Goddard Space Flight Center. *General Environmental Verification Standard (GEVS) for GSFC Flight Programs and Projects*, 2021.

[75] ORTEC. *DSPEC 50*, 2020.

[76] Worthington Industries. *Worthington Industries, LS Series Dewars*, 2017.

[77] G Ventura and V Martelli. Thermal conductivity of kevlar 49 between 7 and 290 k. *Cryogenics*, 49(12):735–737, 2009.

[78] National Institute of Standards and Technology. Material properties: Ofhc copper (uns c10100/c10200). Technical report, 2010.

[79] National Institute of Standards and Technology. Material properties: 6061-t6 aluminum (uns a96061). Technical report.

[80] Piti Ongmongkolkul. Iminuit optimiser and error estimator. https://iminuit.readthedocs.io/en/stable/about.html, 2022.

This work was performed under the auspices of the U.S. Department of Energy by Lawrence Livermore National Laboratory under Contract DE-AC52-07NA27344.

Release: LLNL-TH-838306

Appendix A

Signal Formation and Charge Trapping in Coaxial HPGe Detectors

A.1 Signal Formation

The section estimates induced charged from collection of electrons and holes in the coaxial germanium detector, shown in Figure A.1. The method used for performing this analysis uses the Shokley-Ramo theorem and makes use of the concept of a weighting potential. This technique is outlined in Appendix D of *Radiation Detection and Measurements*[20] and it is recommended that the reader consult this work for more in-depth analysis.

Assumptions used in this work include:

- True coaxial n-type HPGe detector (central bore hole extends through the entirety of the detector). This allows one to assume that charge carriers travel in straight lines between their point of generation and crystal contacts and that there is no z-component in the detector electric and weighting fields.
- Charge carriers are generated at a fixed position within the detector that correspond to a single, full-energy deposition gamma-ray interaction (photoelectric effect).

- The electric field in the HPGe detector is sufficiently large to saturate charge carrier velocities

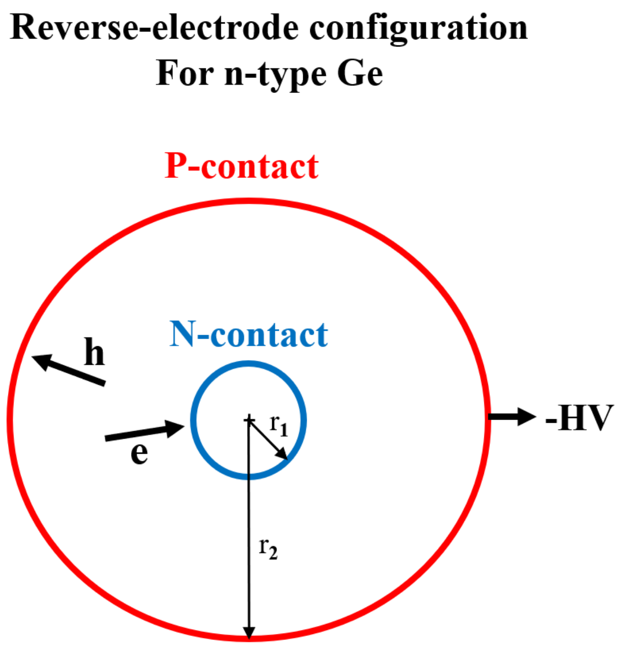

Figure A.1: *Reverse-electrode HPGe detector. A n-type coaxial detector is shown here. The inner circle indicates the detector well (n contact) and the outer circle indicates the crystal's outer surface (p contact).* r_1 *refers to the well radius and* r_2 *is the crystal radius. Electrons and holes are collected on the well and outer surface, respectively, for this crystal configuration.*

Charge induced by electrons and holes moving to crystal contacts can be estimated using Equation A.1[20].

$$Q = q * \Delta W_p \tag{A.1}$$

where Q is the induced charge, q is the charge of an electron, and ΔW_p is the change in weight potential from the beginning to end of the charge carrier path. To determine weighting potential as a function of charge carrier location, the Laplace equation for the geometry of the detector must be solved, as shown Equation A.2.

$$\nabla W_p = 0 \tag{A.2}$$

For cylindrical coordinates, Equation A.2 can be written as

$$\frac{d^2W_p}{dr^2} + \frac{1}{r}\frac{dW_p}{dr} = 0 \tag{A.3}$$

The general solution to Equation A.3 is

$$W_p(r) = C_a * ln(r) + C_b \tag{A.4}$$

where C_a and C_b are constants.

Solving the for the constants in Equation A.4 requires use of boundary conditions. As outlined in[20], these boundary conditions are:

- The voltage on the electrode for which the induced charge is to be calculated is set to 1
- The voltages on all other electrodes are set to zero

Using these boundary conditions, the weighting potential for calculating induced charge on the inner well of the coaxial detector is determined using Equation A.5

$$W_{p,well}(r) = \frac{ln(r)}{ln(\frac{r_1}{r_2})} - \frac{ln(r_2)}{ln(\frac{r_1}{r_2})} \tag{A.5}$$

where r is the position of the charge carrier, r_1 is the well radius, and r_2 is the crystal radius. Weighting potential for induced charge on the outer contact is calculated using Equation A.6.

$$W_{p,outer}(r) = \frac{ln(r)}{ln(\frac{r_2}{r_1})} - \frac{ln(r_1)}{ln(\frac{r_2}{r_1})} \tag{A.6}$$

To determine time-dependent induced charge, one must relate the radial position of a charge carrier to time. This can be done using charge carrier velocity. As mentioned above, this analysis assumes that the electric field inside the HPGe detector is sufficiently high to saturate charge carrier velocities, which corresponds to an electric field strength of approximately

10^5 volts per meter or higher[20;63]. This is a reasonable assumption, as HPGe detectors are typically specified to be operated with electric fields in this range[63]. Saturation velocities for both electrons and holes are approximately 10^5 $[m * s^{-1}]$[20].

For reverse electrode HPGe detectors (n-type germanium), electrons travel to the well (see Figure A.1). Electron position at any time can be calculated using Equation A.7

$$r_e(t) = r_o - v_e * t \tag{A.7}$$

where r_o is the location where the electron was generated, v_e is electron velocity, and t is time. Similarly, A.8 can be used to determine time-dependent hole position

$$r_h(t) = r_o + v_h * t \tag{A.8}$$

where v_h is hole velocity.

Hence, time dependent induced charge from collection of electrons (q_e) in reverse-configured HPGe detectors can be determined by combining Equation A.1 with Equations A.5 and A.7.

$$q_e(t) = q * \left[\left(\frac{ln(r_o - v_e * t)}{ln(\frac{r_1}{r_2})} - \frac{ln(r_2)}{ln(\frac{r_1}{r_2})}\right) - \left(\frac{ln(r_o)}{ln(\frac{r_1}{r_2})} - \frac{ln(r_2)}{ln(\frac{r_1}{r_2})}\right)\right] \tag{A.9}$$

Time dependent induced charge from collection of holes (q_h) is calculated by combining Equation A.1 with Equations A.6 and A.8.

$$q_h(t) = q * \left[\left(\frac{ln(r_o + v_h * t)}{ln(\frac{r_2}{r_1})} - \frac{ln(r_1)}{ln(\frac{r_2}{r_1})}\right) - \left(\frac{ln(r_o)}{ln(\frac{r_2}{r_1})} - \frac{ln(r_1)}{ln(\frac{r_2}{r_1})}\right)\right] \tag{A.10}$$

Equations A.9 and A.10 were used to produce plots shown in Figure 2.9. Note that induced current can be determined by simply taking the time derivative of Equations A.9 and A.10. Induced charge in conventional HPGe detectors can be determined in a similar manner as presented above. One must only change Equations A.7 and A.8 to reflect the fact that charges move in opposite directions in conventional electrode detectors. Figure A.2 shows calculated induced charge for conventional and reverse-electrode HPGe detectors for 3 gamma-ray interaction locations.

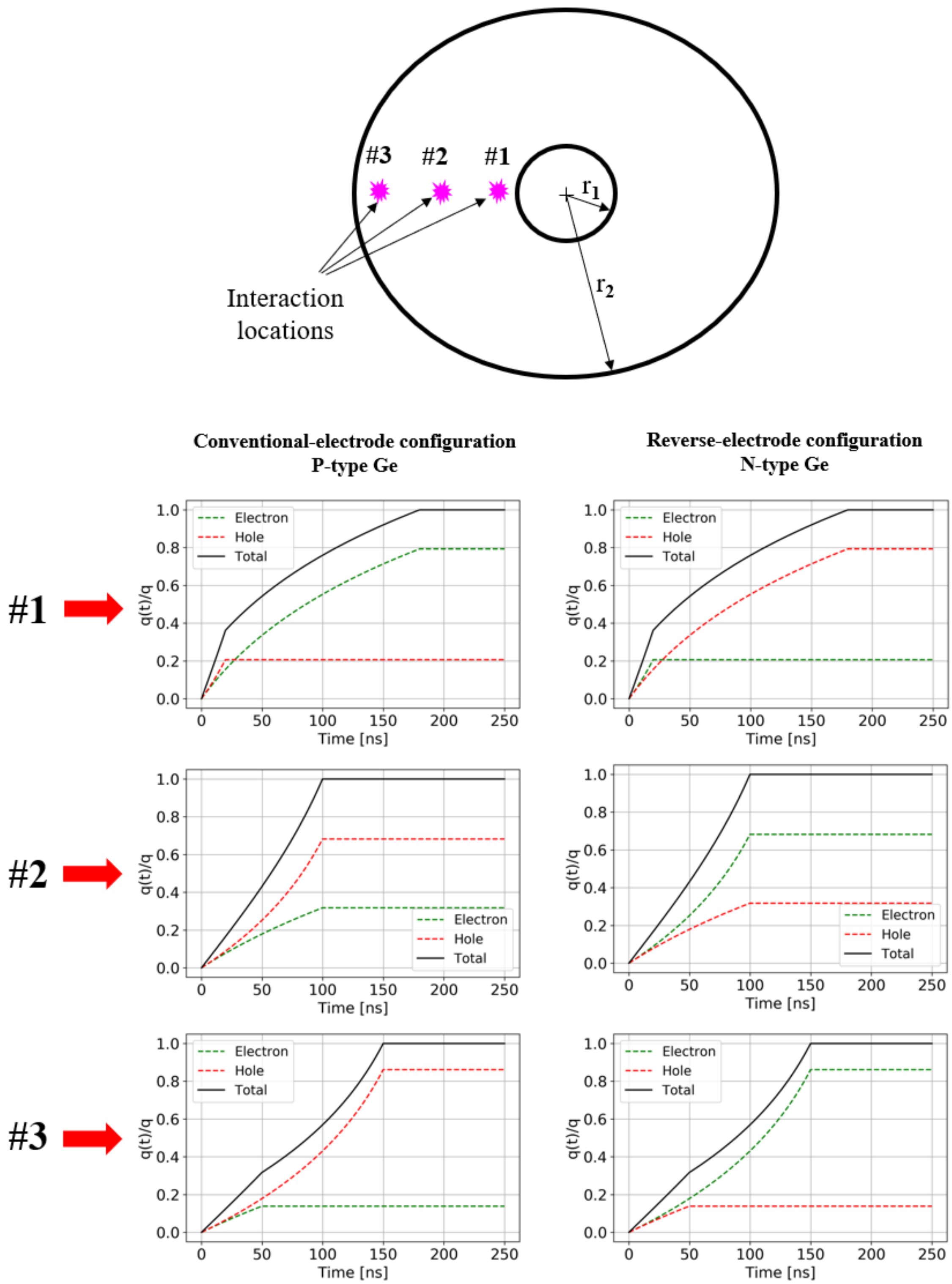

Figure A.2: *Comparison of induced charge in n and p-type coaxial HPGe detectors. The top graphic shows a cross section of a HPGe detector with 3 interaction locations. Charge induction resulting from electrons and holes are shown for each interaction location for both n and p-type detectors.*

A.2 Charge Trapping

When a gamma ray interacts with a HPGe detector, electron-hole pairs are generated and swept to the crystal contacts. As shown in Section A, these charge carriers induce signal as they travel to the n and p-contacts. When a HPGe detector is exposed to a large fluence of high energy particles, hole traps form that have the ability to immobilize holes before they arrive at the p-contact. This reduces the amount of charge induced at the contacts and degrades detector energy resolution. This section overviews a method for estimating energy resolution degradation due to neutron radiation damage. Assumptions and signal calculation described in Section A are used in this analysis.

The probability of charge trapping is quantified by a trapping cross section σ_t. This value is inversely proportional to the electric field[63;66] and is estimated by Equation A.11[66]

$$\sigma_t = \alpha_h * \frac{q}{\epsilon * E(r)} \tag{A.11}$$

where α_h is a dimensionless tuning parameter, q is the charge of an electron, ϵ is Ge permittivity, and $E(r)$ is the electric field in the detector. Experimental data indicates that 0.1 is a reasonable value for α_h[66].

The electric field in a true coaxial detector can be determined by solving Poisson's equation for electrical potential when impurities are present, as shown in Equation A.12.

$$\frac{d^2V}{dr^2} + \frac{1}{r}\frac{dV}{dr} = -\frac{\rho}{\epsilon} \tag{A.12}$$

V represents voltage and ρ is the intrinsic space charge density in germanium. ρ for reverse-electrode detectors is $q * N_D$, where N_D is the impurity concentration of donor atoms. The general solution of radially-dependent voltage is shown in Equation A.13

$$V = -\frac{\rho * r^2}{4 * \epsilon} + C_1 * ln(r) + C_2 \tag{A.13}$$

The constants shown in Equation A.13 can be determined using boundary conditions shown in Figure A.1, namely $V(r_1) - V(r_2)$ is equivalent to the bias applied to the crystal (V_b). Hence the electric field in a reverse-electrode detector is shown in Equation A.14

$$E(r) = \frac{\rho}{2 * \epsilon} * r - \frac{C_1}{r} \tag{A.14}$$

where C_1 is

$$C_1 = \frac{V_b - \frac{\rho}{4 * \epsilon} * (r_2^2 - r_1^2)}{ln(\frac{r_1}{r_2})} \tag{A.15}$$

The probability that a hole completes its journey from the gamma-ray interaction location to the outer p-contact in a reverse-electrode detector can be estimated using Equation A.16 [66]

$$p_q(r_o, r_2) = exp\left(-\int_{r_o}^{r_2} \rho_t * \sigma_t(r) dr\right) \tag{A.16}$$

where r_o is the gamma-ray interaction radial position and ρ_t is the density of hole traps in the germanium detector. Darken et al. estimated that a fast neutron flux of 10^{10} $[cm^{-2}]$ would produce a trap density of approximately 2×10^9 $[cm^{-3}]$ [62].

A computer simulation can be used to illustrate the effects of charge trapping on HPGe gamma-ray spectroscopy. This is done by using Equation A.16 to calculate the probability density and cumulative density functions for trapping. The probability density function (PDF) for hole trap position is defined as

$$PDF = -\frac{dp_q(r_o, r)}{dr} \tag{A.17}$$

The integral of the PDF is the cumulative density function (CDF), which indicates the probability that a hole created at r_o never arrives at radial position r is

$$CDF = 1 - p_q(r_o, r) \tag{A.18}$$

The inversion method can be used to sample the CDF to determine if a hole is trapped before it reaches the detector contact, and, if so, the hole trap location. This is shown in Equation A.19

$$x = CDF = 1 - p_q(r_o, r_2) \tag{A.19}$$

where x is a random variable between 0 and 1. Further information about sampling techniques can be found in[66].

Sampling Equation A.19 provides a stochastic method for determining the final position of the hole. If no trapping occurs, the final hole position is the detector p contact. If the hole becomes trapped, its final location is somewhere between its original location and the p contact. Once final hole location is determined, Equations A.9 and A.10 can be used to determine the induced charge from electrons and holes.

This method was used to simulate charge trapping for two detectors. One was assumed to not have any hole trapping and the other was assumed to have been exposed to a fast neutron fluence of 10^{10} cm^{-2}. Each simulation considered ten-thousand, 1333 keV gamma ray interactions. Initial interaction positions (and resulting electron-hole pair generation locations) were randomly sampled from a uniform areal distribution that corresponded to the crystal cross section. The average number of electron-hole pairs generated per gamma-ray interaction (N_p) is shown in Equation A.20

$$N_p = \frac{E_y}{E_{e-h}} \tag{A.20}$$

where E_y is gamma-ray energy and E_{e-h} is the average energy required to excite an electron-hole pair in Ge (2.96 eV[20]). It was assumed that N_p is normally distributed with a standard deviation of $\sqrt{N_p * F}$, where F is the Fano factor. *Radiation Detection and Measurements*[20] indicates reasonable values for F are between 0.057 and 0.129. Detector dimensions and donor impurity content are consistent with the Dragonfly GRS. Simulation results and parameters are shown Figure A.3 and Table A.1, respectively. The magnitude of the radially-dependent electric field used in these calculations is shown in Figure A.4. Note that no electron trapping was considered. This is a reasonable assumption, as it is estimated that the electron trapping cross section is two orders of magnitude less than that of holes in HPGe detectors that are damaged by high-energy neutrons[66;71].

Table A.1: *Trapping Simulation Parameters*

Parameter	Value	Description
r_1	5×10^{-3} $[m]$	Crystal well radius
r_2	25×10^{-3} $[m]$	Crystal outer radius
q	1.6022×10^{-19} $[C]$	Electron charge
α_h	0.1	Tuning parameter
ϵ	1.416×10^{-10} $[s^4 * A^2 * m^{-3} * kg^{-1}]$	Ge permittivity
N_D	1.3×10^{16} $[m]^{-3}$	Crystal donor density[33]
V_b	3000 $[V]$	Crystal bias
ρ_t	2×10^{15} $[m^{-3}]$	Hole trap density
F	0.1	Fano factor

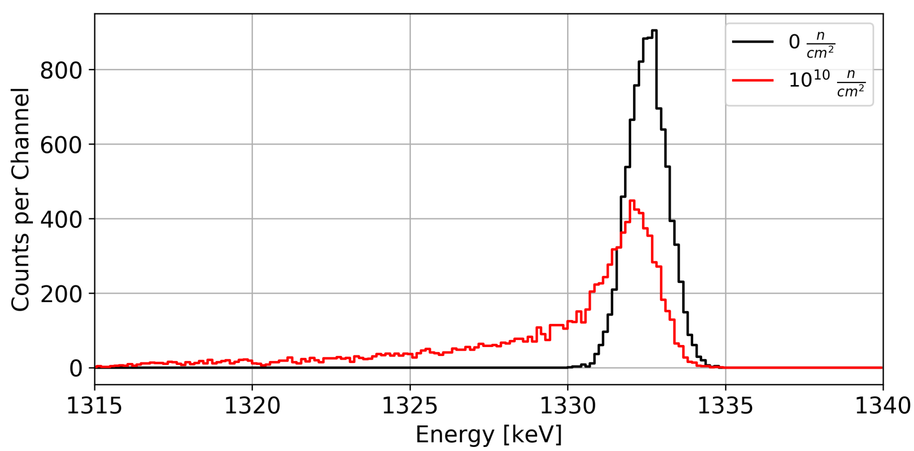

Figure A.3: *Charge trapping simulation. Data shown in black correspond to a detector that has not been exposed to fast neutrons and data shown in red correspond to the same detector after exposure to a fast neutron fluence of* 10^{10} cm^{-2}.

The method presented here is useful for illustrating how neutron radiation damage degrades GRS spectral performance. However, it utilizes several simplifying assumptions that limit its accuracy in predicting resolution degradation for the Dragonfly GRS. First, the

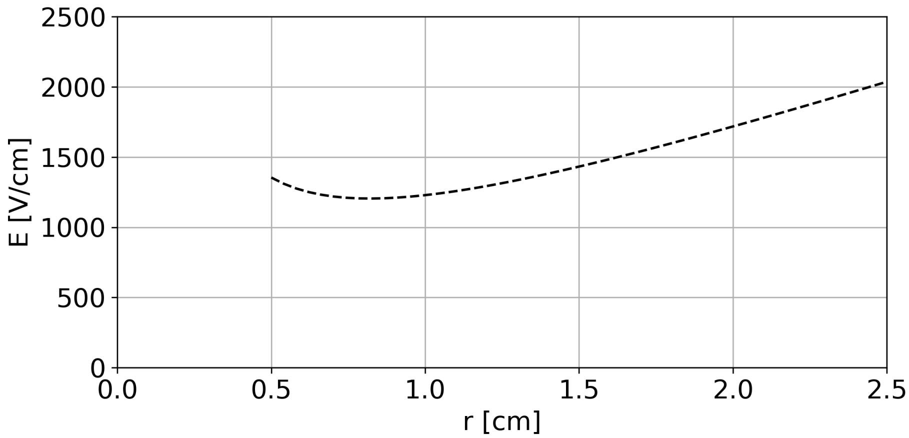

Figure A.4: *True coaxial detector electric field. The electric field calculated using Equation A.14 and the parameters listed in Table A.1 is shown. Radial positions of* 0.5 *cm and* 2.5 *cm correspond to the well (n contact) and outer crystal surface (p contact), respectively.*

electric field calculation shown in Equation A.14 applies to true coaxial detectors. As indicated in Figure 2.2, the Dragonfly GRS utilizes a closed-ended HPGe crystal. True coaxial and closed-ended detectors have different electric fields, which affects both induced charge calculations and trapping probability. This difference is illustrated in Figure A.5[11]. Hole trap density is difficult to estimate, as it depends on the electric field and the neutron environment. Lastly, this model assumes that gamma-rays deposit all of their energy at a single location. While this is possible, gamma rays can also interact multiple times before contributing to a full-energy peak. This affects signal formation and trapping, as multiple interactions locations result in electron-hole pairs being generated at multiple positions within the crystal.

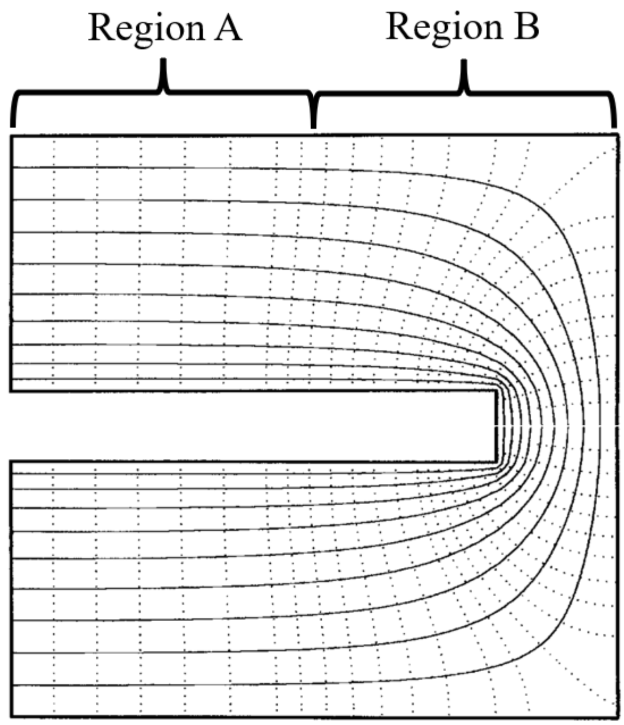

Figure A.5: *Closed-ended HPGe detector*[11]. *Coaxial HPGe detectors have electric field lines that extend between the outer crystal surface and the well. Shown here is cross section of a closed-ended coaxial HPGe detector. Note that the electric field lines (dashed) are straight and have nearly the same length in Region A. This is similar to a true coaxial detector's electric field, which was analytically determined in Equation A.14. However, the electric field lines in Region B are not straight and vary in length due to the well. Additionally, the magnitude of the electric field varies significantly in this region, as indicated by the potential field (solid lines). Hence, signal generation and charge trapping effects in Region A will differ from Region B.*

Appendix B

Dragonfly DM Thermal Model

B.1 Thermal Model Overview

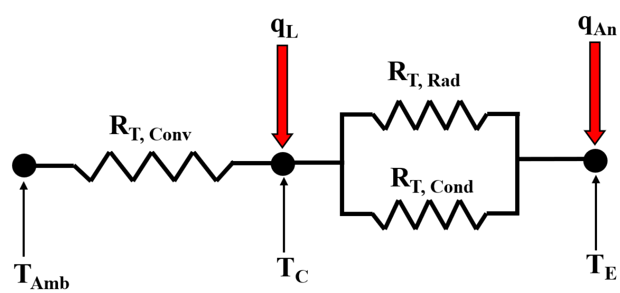

Figure B.1: *This thermal model was used to predict DM cooling and annealing power.*

Figure B.1 show a thermal model of the Dragonfly GRS. Nodes represent temperatures: T_E is the crystal encapsulation, T_C is the cryostat, and T_{Amb} refers to Titan's ambient conditions. Red arrows represent heat input. q_L is heat flow from the lander and q_{An} represents heat input from an onboard anneal heater.

Analysis of the DM begins with creating a control volume around the cryostat and a energy flow balance:

$$\frac{dE_{stored}}{dt} = \dot{E_{in}} - \dot{E_{out}} + \dot{E_{gen}} \tag{B.1}$$

By replacing energy rate terms with heat flows and energy storage with heat capacity, Equation B.2 can be used

$$m_C * c_C \frac{dT_C}{dt} = [q_E + q_L] - [q_{Amb}] \tag{B.2}$$

where q_E is heat flow from the encapsulation to the cryostat, q_L is heat flow from the lander, and q_{Amb} is heat flow from the cryostat to Titan's atmosphere. Other variables are listed in Table 2.1. Using a electrical analogy heat transfer method discussed in[47], one can write heat flows (q) as functions of thermal resistance (R_{th}) and temperature drop (ΔT), as shown in Equation B.3.

$$\Delta T = q * R_{th} \tag{B.3}$$

This allows for Equation B.2 to be rewritten as:

$$m_C * c_C * \frac{dT_C}{dt} = \left[\frac{T_E - T_C}{(R_{th,Rad}^{-1} + R_{th,Cond}^{-1})^{-1}} + q_L\right] - \left[\frac{T_C - T_{Amb}}{R_{th,Conv}}\right] \tag{B.4}$$

Heat transfer at the crystal encapsulation can be analyzed similarly. Analysis of heat flow at a control volume encompassing crystal encapsulation results in Equation B.5.

$$m_E * c_E \frac{dT_E}{dt} = [q_A] - [q_C] \tag{B.5}$$

q_A represents heat inflow from the anneal heater and q_C is heat outflow to the cryostat. Using Equation B.3, the Equation B.6 can be written.

$$m_E * c_E * \frac{dT_E}{dt} = q_{An} - \left[\frac{T_E - T_C}{(R_{th,Rad}^{-1} + R_{th,Cond}^{-1})^{-1}}\right] \tag{B.6}$$

Equations B.4 and B.6 are coupled differential equations that must be solved simultaneously to model DM temperature. These equations were solved using a Python iterative differential equation solver.

The analysis presented here assumes that that there is no significant temperature gradient across the cryostat or crystal encapsulation. That is, each component is assumed to have uniform temperature at any instant of transient heating or cooling. This assumption simplifies thermal modeling, but its validity needs to be verified[47]. This can be done by calculating a dimensionless parameter called Biot number (Bi), which is the ratio of a component's internal thermal resistance to the thermal resistance of heat flowing into or out of the component. If Bi is less than 10^{-1}, the error associated with the uniform temperature assumption is small and the uniform-temperature assumption is valid. Bi calculations for the cryostat and encapsulation are discussed in Section B.5.

B.2 Thermal Resistance Calculations

Thermal resistances (inverse of thermal conductance) are used to quantify a materials resistance to heat flow. There are three thermal resistances considered for the Dragonfly DM: convective thermal resistance between the GRS and Titan's atmosphere, radiative thermal resistance between the encapsulated detector and the outer cryostat, and conductive thermal resistance between the encapsulated detector and the outer cryostat. Thermal resistance is calculated using Equation B.3. Figure B.2 illustrates the thermal resistances considered in the thermal model.

Convective thermal resistance between the outer cryostat and Titan ambient conditions can be calculated using Equation B.7[47]

$$R_{th,Conv} = \frac{1}{h * A_{surf}} \tag{B.7}$$

where h is the convective heat transfer coefficient on Titan's surface ($2.7\frac{W}{m^2*K}$[46]) and A_{surf} is outer surface area of the cryostat.

Radiative thermal resistance was calculated by modeling the encapsulation and cryostat as concentric cylinders. Heat transfer between concentric cylinders was is calculated by Howell

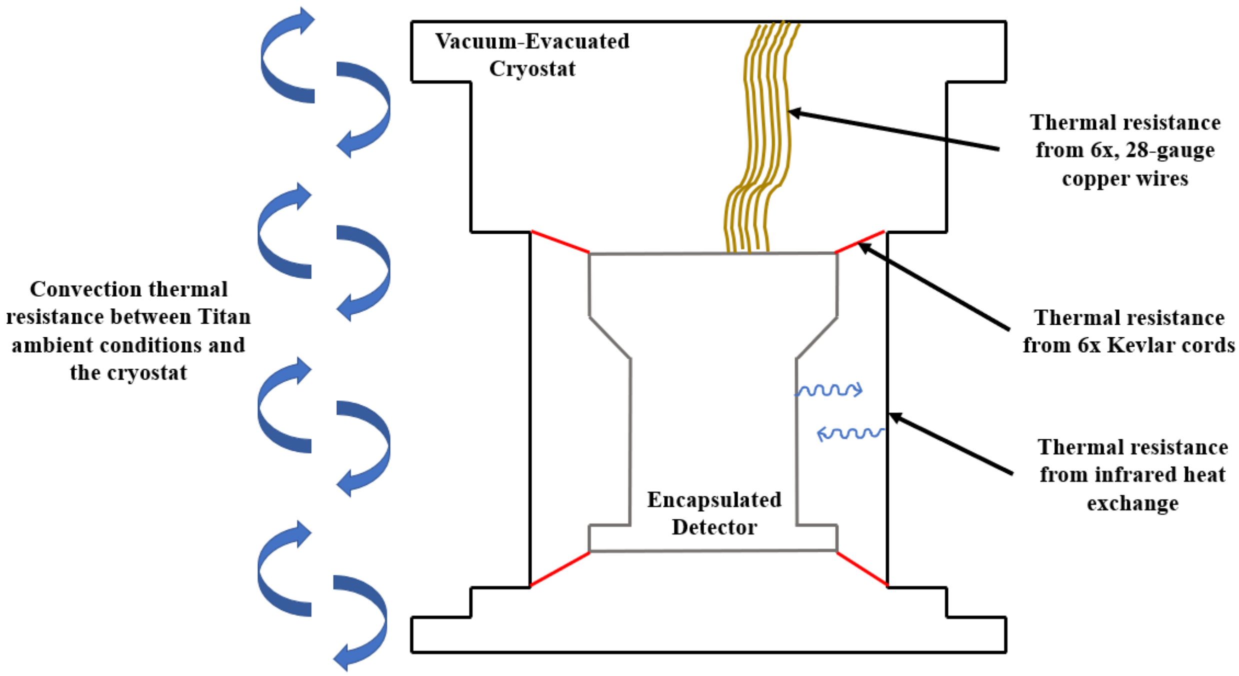

Figure B.2: *Thermal resistances control heat flow in the thermal model. The encapsulated detector is thermally connected to the cryostat via a conductive thermal resistance comprised of wires and Kevlar cords and a radiative thermal resistance. The cryostat is convectively connected to Titan's atmosphere through a convective thermal resistance.*

et al. and is shown in Equation B.8. Derivation of this formula is located in[13].

$$q_{Rad} = \frac{A_1 * \sigma * (T_1^4 - T_2^4)}{\frac{1}{\epsilon_1} + \frac{A_1}{A_2} * (\frac{1}{\epsilon_2} - 1)} \tag{B.8}$$

Subscripts 1 and 2 indicate the inner and outer cylinders, ϵ is surface emissivity, and A is cylindrical surface area.

By Equation B.3, Radiative thermal resistance is calculated by dividing temperature difference (T_1-T_2) by Equation B.8. Radiative thermal resistance for the DM is shown in Equation B.9.

$$R_{th,Rad} = \frac{\frac{1}{\epsilon_E} + \frac{A_E}{A_C} * (\frac{1}{\epsilon_C} - 1)}{A_E * \sigma * (T_E^2 + T_C^2) * (T_E + T_C)} \tag{B.9}$$

Subscripts 1 and 2 were replaced with E and C, respectively, to indicate which variables are associated with the encapsulation and cryostat. Both the encapsulation and cryostat were fabricated clean, low-surface roughness ($\leq$0.8 μ m Ra) aluminum. Hence, a emissivity value of 0.05 was used for both components. This is consistent with lightly-polished metal[47]. Equation B.9 is applicable for diffuse, gray surfaces, i.e. it is assumed that photons are emitted uniformly in all directions and emissivity and absorptivity are independent of wavelength.

Conductive thermal resistance considers heat flow through solids that span between the encapsulation and cryostat and is comprised of two parallel components: Kevlar and wires. Kevlar thermal resistance is shown in Equation B.10

$$R_{th,Kevlar} = \frac{L_{Kevlar}}{k_{Kevlar} * A_{Kevlar} * N_{Kevlar}} \tag{B.10}$$

where L_{Kevlar} is the length of the Kevlar spanning between the cryostat and crystal encapsulation, k_{Kevlar} is the thermal conductivity of Kevlar 49 (see Section B.3), A_{Kevlar} is the cross sectional area of the Kevlar, and N_{Kevlar} is the number of Kevlar strands connecting the cryostat and encapsulation.

Wire thermal resistance is calculated by Equation B.11

$$R_{th,Wire} = \frac{L_{Wire}}{k_{Wire} * A_{Wire} * N_{Wire}} \tag{B.11}$$

where L_{Wire} is the length of the wire spanning between the cryostat and crystal encapsulation, k_{Wire} is the thermal conductivity of the wire (see Section B.3), A_{Wire} is the cross sectional area of the wire, and N_{Wire} is the number of wires used.

The total conductive thermal resistance between the cryostat and encapsulation is calculated by Equation B.12.

$$R_{th,Cond} = (R_{th,Kevlar}^{-1} + R_{th,Wire}^{-1})^{-1} \tag{B.12}$$

B.3 Temperature Dependent Thermal Properties

Kevlar thermal conductivity is shown in Equation B.13[77]

$$k_{Kevlar} = 5.03 * 5.07 * \exp\left(-0.00487 * T\right) \tag{B.13}$$

where T is temperature in Kelvin and k_{Kevlar} is calculated in units of $\frac{W}{m*K}$. Note that the Kevlar cords span between two components (the crystal encapsulation and the cryostat) that are at different temperatures. This means that the Kevlar will not be isothermal. To account for this, Kevlar thermal conductivity was calculated using the average of the crystal encapsulation and cryostat temperatures.

Thermal conductivity of the copper wires used with the DM was calculated using Equation B.14[78]

$$k_{Wires} = 10^{\frac{a+c*T^{0.5}+e*T+g*T^{1.5}+i*T^{2}}{1+b*T^{0.5}+d*T+f*T^{1.5}+h*T^{2}}} \tag{B.14}$$

where a-i are shown in Table B.1. Similar to Kevlar thermal conductivity, wire thermal conductivity calculations used an average temperature.

Temperature dependent heat capacity of 6061-T6 aluminum is shown in Equation B.3[79]

$$c_{Al} = 10^{a+b*log_{10}(T)+c*(log_{10}(T))^2+d*(log_{10}(T))^3+e*(log_{10}(T))^4 +f*(log_{10}(T))^5+g*(log_{10}(T))^6+h*(log_{10}(T))^7+i*(log_{10}(T))^8}$$

where variables a-i are listed in Table B.1.

Temperature dependent specific heat capacity of germanium is shown in Figure B.3.

B.4 Thermal Model Thermal Resistances

Figure B.4 shows thermal resistance values corresponding to a predicted passive cool down on Titan's surface. This simulation assumes that the GRS was at a steady-state temperature of 273 K at time = 0, after which it was exposed to Titans atmosphere (94 K, $2.7\frac{W}{m^2*K}$).

Table B.1: *NIST Conductivity and Specific Heat Parameters*

Variable Name	Equation B.14	Equation B.3
a	1.8743	46.6467
b	-0.41538	-314.292
c	-0.6018	866.662
d	0.13294	-1298.3
e	0.26426	1162.27
f	-0.0219	-637.795
g	-0.051276	210.351
h	0.0014871	-38.3094
i	0.003723	2.96344

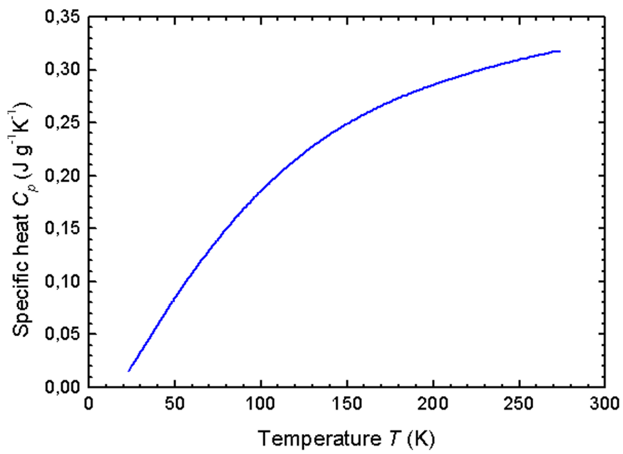

Figure B.3: *Temperature dependent germanium heat capacity*[12]

B.5 Biot Number Calculation

Biot number for the cryostat was calculated using Equation B.15[47]

$$Bi = \frac{R_{cond}}{R_{conv}} = \frac{h * L_c}{k} \tag{B.15}$$

where h is the heat transfer coefficient and k is the thermal conductivity of the solid material. L_c is the characteristic length of the system and can be calculated by Equation B.16

$$L_c = \frac{V}{A_s} \tag{B.16}$$

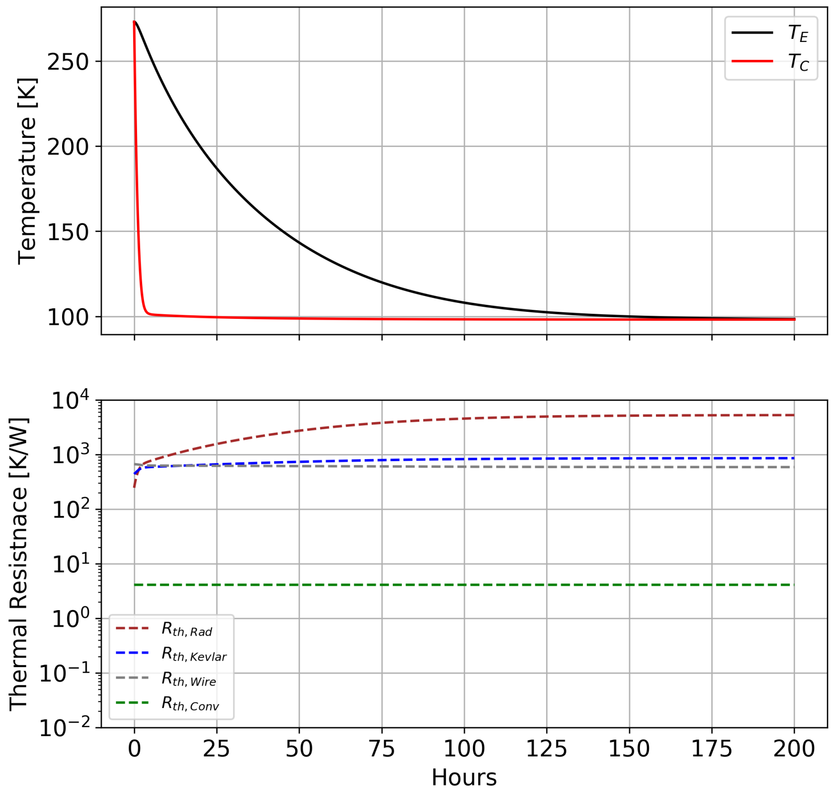

Figure B.4: *Thermal model predicted passive cooling and thermal resistances.* ***Top:*** *Simulated crystal encapsulation and cryostat temperatures during passive cooling are shown in the solid black and red lines, respectively.* ***Bottom:*** *As GRS temperature changes, so do thermal resistances. Radiative thermal resistance is shown by the dashed brown line, conductive thermal resistance from the Kevlar and copper wires are shown in the dashed blue and gray lines, respectively, and convective thermal resistance is shown by the dashed green line.*

where V is the component volume and A_s is the area of the cryostat that interacts with the convective boundary.

Cryostat Biot number was calculated to be 10^{-4} at a cryostat temperature of 273 K. This indicates that the uniform temperature assumption was valid.

Evaluating the temperature gradient of the crystal encapsulation is more difficult. This is because encapsulation internal design is proprietary to the manufacturer. Hence, it is not possible to calculate internal thermal resistance. Discussions with the manufacturer indicate that the crystal is thermally connected to the aluminum encapsulation via large area soft metal contacts. This means that the the crystal is heat sunk to to the crystal encapsulation. Additionally, both germanium and aluminum have high thermal conductivity (both over 100 $\frac{W}{m*K}$ at 273 K). This indicates that encapsulation internal thermal resistance should be low. Heat transfer out of the encapsulation (to the cryostat) was designed to be small to facilitate low-power annealing on Titan's surface. Therefore, it is reasonable to claim that the temperature gradient across the crystal encapsulation should be small in comparison to the temperature difference between the encapsulation and cryostat.

B.6 Gas Thermal Conduction

This section relates cryostat pressure to steady-state gas conduction heat transfer for the Dragonfly DM. The following assumption were made:

- The Dragonfly DM was be modeled as two concentric cylinders, separated by a 1 cm gap. The inner cylinder represents the crystal encapsulation and the outer cylinder represents the cryostat.
- Both cylinders were assumed to have uniform temperature
- The gas was assumed to be 100% nitrogen

Gas conduction depends on flow regime. Three types are possible: continuum, mixed, free molecular flow. In continuum flow, the mean free path, or average distance a molecule travels before interacting with other molecules, is much shorter than enclosure dimensions. Hence, heat is transferred between molecule-molecule interactions. The mean free path (MFP) in free molecular flow regime (FMF) is much longer than chamber dimensions. This means that gas heat transfer is dominated by molecule-enclosure interactions. Lastly, mixed flow occurs when MFP is similar to enclosure dimensions.

Flow regimes in a system can be determined by calculating the Knudsen number, as shown in Equation B.17

$$K_n = \frac{MFP}{L_E} \tag{B.17}$$

where $\mathrm{K_n}$ is the Knudsen number and $\mathrm{L_e}$ is the characteristic length of a system. Characteristic length is calculated in Equation B.18.

$$L_e = \frac{4 * V}{A_s} \tag{B.18}$$

For concentric cylinders, V is the gas volume between the cylinders and $\mathrm{A_s}$ is the cylinder surface area. Table B.2 shows ranges of Knudsen numbers for each flow regime.

MFP can be calculated using Equation B.19[49]

$$MFP = \frac{2.33 * 10^{-20}}{p * D_m} \tag{B.19}$$

where p and D_m are the pressure and the molecular diameter of the gas.

Table B.2: *Knudsen Numbers for Flow Regimes*[13]

Flow Regime	K_n
Continuum	$K_n < 10^{-2}$
Mixed	$10^{-2} < K_n < 3\times10^{-1}$
Free Molecular Flow	$K_n > 3\times10^{-1}$

Gas conduction in the molecular state is proportional to pressure[13]. Hence, high quality vacuum is needed to reduce gas conduction to a negligible amount. FMF heat transfer between concentric cylinders can be calculated using a method published by Barron et al. This process will be briefly overviewed here, but it is recommended that the reader consult[13] for in-depth analysis.

Heat transfer by gas in the molecular flow regime can be calculated by Equation B.20.

$$Q = \frac{F_a * G * p * (T_2 - T_1)}{A_1} \tag{B.20}$$

Q refers to net heat transferred between surfaces. Subscripts 1 and 2 refer to the inner and outer cylinders, respectively, p is pressure, T is surface temperature, and A is surface area. The accommodation coefficient factor, F_a for concentric cylinders is calculated in Equation B.21. It relates molecule-surface heat transfer to geometry and gas properties.

$$F_a = \left(\frac{1}{a_1} + \frac{A_1}{A_2} * \left(\frac{1}{a_2} - 1\right)\right)^{-1} \tag{B.21}$$

An accommodation coefficient (a) is the ratio of the actual energy transferred by a molecule-wall interaction to the the maximum possible energy transfer. It is dependent on gas species and surface condition.

G is calculated by Equation B.22

$$G = \left(\frac{\gamma + 1}{\gamma - 1} * \left(\frac{R}{8 * \pi * T} \right)^{0.5} \right) \tag{B.22}$$

Equation B.17 was used to determine that flow in the DM is in the free molecular region for pressures lower than 10^{-2} mbar. Equation B.20 was used to estimate DM gas heat transfer at multiple pressures. Note that the surface anneal case was considered, where the crystal encapsulation (inner cylinder) will be held at 378 K and the cryostat will be approximately 94K. This represents worst-case heat transfer, as the temperature difference between the surfaces is maximized. Figures B.6 and B.5 show the results of these calculation.

Table B.3 lists variables used for calculations performed in this section.

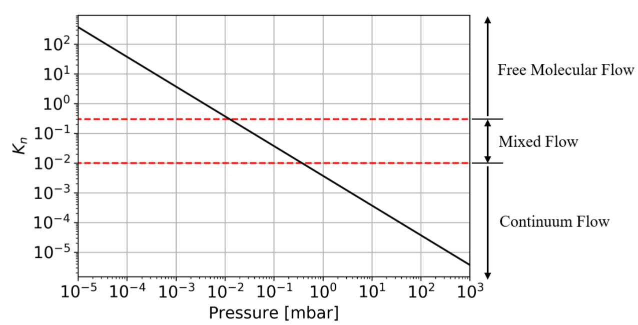

Figure B.5: *The Knudsen number was calculated for the DM. This calculation indicates when FMF heat transfer calculations are applicable.*

Table B.3: *FMF Heat Transfer and K_n Variables*

Variable	Symbol	Value
Inner cyl. temperature	T_1	378 K
Outer cyl. Temperature	T_2	94 K
Inner cyl. surface area	A_1	2.5×10^{-2} m^2
Outer cyl. surface area	A_2	4.0×10^{-2} m^2
Gas volume	V	3.2×10^{-4} m^3
Spec. heat ratio	γ	1.4
Accommodation Coefficient	a	0.9[13]

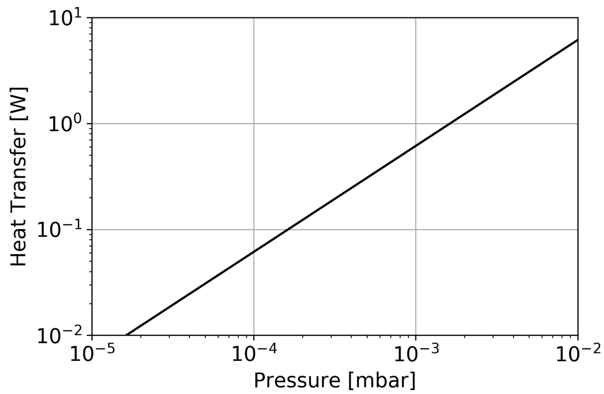

Figure B.6: *This plot shows estimated gas heat transfer for the DM in the FMF regime.*

Appendix C

Neutron-Induced Gamma-ray Measurements

Table C.1: *DM Cf-252 Measurement*

Energy [keV]	Interaction	Red. Chi^2	FWHM [keV]	Net Area [CPS]
8579	Cl-35(n,γ)	1.25	6.74 +/- 1.16 $\times 10^{-1}$	1.637 $\times 10^{-3}$ +/- 5.40 $\times 10^{-5}$
7790	Cl-35(n,γ)	1.47	5.76 +/- 5.58 $\times 10^{-2}$	5.122 $\times 10^{-3}$ +/- 9.55 $\times 10^{-5}$
6977	Cl-35(n,γ)	1.45	5.27 +/- 1.50 $\times 10^{-1}$	1.923 $\times 10^{-3}$ +/- 5.853 $\times 10^{-5}$
5713	Cl-35(n,γ)	0.566	4.91 +/- 7.26 $\times 10^{-2}$	5.903 $\times 10^{-3}$ +/- 1.026 $\times 10^{-4}$
4978	Cl-35(n,γ)	1.21	4.39 +/- 8.30 $\times 10^{-2}$	4.523 $\times 10^{-3}$ +/- 8.977 $\times 10^{-5}$
3061	Cl-35(n,γ)	1.08	3.55 +/- 5.01 $\times 10^{-2}$	7.550 $\times 10^{-3}$ +/- 1.160 $\times 10^{-4}$
2614	Background	1.49	3.42 +/- 1.90 $\times 10^{-2}$	2.694 $\times 10^{-2}$ +/- 2.191 $\times 10^{-4}$
2223	H-1(n,γ)	3.83	3.15 +/- 5.00 $\times 10^{-3}$	1.673 $\times 10^{-1}$ +/- 5.460 $\times 10^{-4}$
1461	Background	2.82	2.83 +/- 7.88 $\times 10^{-3}$	1.042 $\times 10^{-1}$ +/- 4.309 $\times 10^{-4}$
1165	Cl-35(n,γ)	3.47	2.74 +/- 8.06 $\times 10^{-3}$	1.103 $\times 10^{-1}$ +/- 4.433 $\times 10^{-4}$

Appendix D

Photopeak Fits for Radiation Damage/Annealing Experiment

Three functions were used to fit data measured during the radiation damage and annealing experiment: Gaussian, exponentially-modified Gaussian, and step functions. Equation D.1 shows the formula for the Gaussian component of the data fit.

$$F(x, a_g, \mu_g, \sigma_g) = a_g * exp\left(\frac{-(x-\mu_g)^2}{2*\sigma_g^2}\right) \tag{D.1}$$

a_g, μ_g, and ${\sigma_g}^2$ are the amplitude, mean energy, and variance of the Gaussian function. Equation D.2 is the exponentially-modified Gaussian (EMG) function used for fitting.

$$\begin{aligned} &F(x, a_{EMG}, \mu_{EMG}, \sigma_{EMG}, \tau) = a_{EMG} * exp\left(\left(\tfrac{1}{2*\tau} * \left(2*x - 2*\mu_{EMG} + \tfrac{\sigma_{EMG}^2}{\tau}\right)\right)\right) \\ &*erfc\left(\tfrac{x-\mu_{EMG})+\frac{\sigma_{EMG}^2}{\tau}}{\sqrt{2}*\sigma_{EMG}}\right) \end{aligned} \tag{D.2}$$

where a_{EMG} is the amplitude, and μ_{EMG} and ${\sigma_{EMG}}^2$ are the mean energy and variance of the Gaussian component of the EMF function, respectively. τ indicates the severity of low-energy tailing in the EMF function.

Equation D.3 is a step function used to subtract background contributions to the photopeak.

$$F(E_H, S, \mu_{step}, \sigma) = \frac{S}{2} * erfc\left(\frac{x - \mu_{step}}{\sqrt{2} * \sigma}\right) + E_H \tag{D.3}$$

E_H is the gamma-ray continuum level on the high-energy side of the photopeak, S is the difference between continuum on the low-energy side of the photopeak and E_H, and μ_{step} is the mean of the step function.

The sum of Equations D.1, D.2, and D.3 were used to fit the 1333 keV Co-60 photopeak measured during the radiation damage and annealing experiments. The Python fitting code iminuit[80] was used to fit the data. Note that the variable σ_{EMG} was constrained to be greater than 0.7 to make fitting stable.

Fit parameters for the measurements listed in Table 3.2 are shown in Table D.1. These fits correspond to the experiment in which detector energy resolution was measured at various neutron fluences. Plots of raw data and fits are shown in Figure D.1.

Fit parameters for the measurements listed in Table 3.3 are shown in Table D.2. These fits correspond to the experiment in which the radiation-damaged detector's Co-60 energy resolution and photopeak efficiency were measured as a function of anneal time.

Table D.1: *Radiation Damage Experiment 1333 keV Photopeak Fit Parameters*

Meas.	a_g	μ_g [keV]	σ_g [keV]	a_{EMG} [keV]	μ_{EMG} [keV]	σ_{EMG} [keV]	τ [keV]	μ_{step} [keV]	E_H	S	Live Time [s]	Red. Chi^2
1	1.212×10^{3}	1.3328×10^{3}	8.03×10^{-1}	9.999×10^{-2}	1.3300×10^{3}	7.00×10^{-1}	1.00×10^{-1}	1.3331×10^{3}	1.60×10^{0}	3.60×10^{0}	300	1.32
2	1.194×10^{3}	1.3320×10^{3}	8.27×10^{-1}	4.991×10^{2}	1.3303×10^{3}	7.00×10^{-1}	8.61×10^{-2}	1.3321×10^{3}	1.83×10^{0}	4.12×10^{0}	300	1.07
3	1.028×10^{3}	1.3316×10^{3}	8.39×10^{-1}	2.378×10^{2}	1.3307×10^{3}	7.00×10^{-1}	9.04×10^{-1}	1.3313×10^{3}	2.48×10^{0}	2.85×10^{0}	300	1.14
4	9.422×10^{2}	1.3313×10^{3}	8.89×10^{-1}	1.923×10^{2}	1.3304×10^{3}	7.00×10^{-1}	1.27×10^{0}	1.3311×10^{3}	2.16×10^{0}	3.03×10^{0}	300	1.32
5	7.156×10^{2}	1.3310×10^{3}	8.91×10^{-1}	3.118×10^{2}	1.3303×10^{3}	7.00×10^{-1}	1.51×10^{0}	1.3309×10^{3}	2.36×10^{0}	3.26×10^{0}	300	1.31
6	4.687×10^{2}	1.3305×10^{3}	9.11×10^{-1}	3.104×10^{2}	1.3296×10^{3}	7.00×10^{-1}	2.46×10^{0}	1.3308×10^{3}	2.73×10^{0}	2.43×10^{0}	300	1.34
7	4.875×10^{2}	1.3303×10^{3}	1.04×10^{0}	2.273×10^{2}	1.3291×10^{3}	7.00×10^{-1}	2.86×10^{0}	1.3301×10^{3}	2.62×10^{0}	2.59×10^{0}	300	1.43
https://www.overleaf.com/project/6282bea7b47bba6552b982fd 8	3.663×10^{2}	1.3303×10^{3}	9.68×10^{-1}	2.472×10^{2}	1.3293×10^{3}	8.02×10^{-1}	3.25×10^{0}	1.3300×10^{3}	2.65×10^{0}	3.17×10^{0}	300	1.36
9	3.557×10^{2}	1.3299×10^{3}	1.03×10^{0}	2.177×10^{2}	1.3286×10^{3}	9.67×10^{-1}	3.65×10^{0}	1.3305×10^{3}	2.43×10^{0}	3.71×10^{0}	300	1.15
10	9.414×10^{1}	1.3277×10^{3}	1.73×10^{0}	2.741×10^{2}	1.3300×10^{3}	7.00×10^{-1}	5.81×10^{0}	1.3305×10^{3}	5.61×10^{0}	2.59×10^{1}	600	1.02
11	1.337×10^{2}	1.3279×10^{3}	1.59×10^{0}	2.457×10^{2}	1.3300×10^{3}	7.79×10^{-1}	6.26×10^{0}	1.3280×10^{3}	5.81×10^{0}	2.39×10^{1}	600	1.10
12	9.200×10^{1}	1.3275×10^{3}	1.82×10^{0}	2.501×10^{2}	1.3297×10^{3}	7.87×10^{-1}	5.78×10^{0}	1.3277×10^{3}	5.93×10^{0}	2.41×10^{1}	600	0.958
13	3.130×10^{2}	1.3285×10^{3}	9.95×10^{-1}	2.116×10^{2}	1.3277×10^{3}	7.22×10^{-1}	5.03×10^{0}	1.3266×10^{3}	6.42×10^{0}	2.15×10^{1}	600	1.18

Table D.2: *Annealing Experiment 1333 keV Photopeak Fit Parameters*

Meas.	a_g	μ_g [keV]	σ_g [keV]	a_{EMG} [keV]	μ_{EMG} [keV]	σ_{EMG} [keV]	τ [keV]	μ_{step} [keV]	E_H	S	Live Time [s]	Red. Chi^2
1A	7.982×10^{3}	1.3271×10^{3}	8.71×10^{-1}	9.549×10^{3}	1.3263×10^{3}	1.13×10^{0}	8.60×10^{-1}	1.3241×10^{3}	6.12×10^{0}	6.76×10^{1}	4400	1.90
2A	5.432×10^{4}	1.3233×10^{3}	7.66×10^{-1}	2.324×10^{4}	1.3227×10^{3}	7.00×10^{-1}	3.83×10^{-1}	1.3215×10^{3}	2.08×10^{1}	2.58×10^{2}	16014	1.14
3A	1.592×10^{4}	1.3188×10^{3}	7.47×10^{-1}	1.344×10^{3}	1.3185×10^{3}	7.00×10^{-1}	5.19×10^{-1}	1.3165×10^{3}	3.37×10^{0}	6.98×10^{1}	4200	1.21
4A	4.171×10^{4}	1.3142×10^{3}	7.57×10^{-1}	3.962×10^{3}	1.3136×10^{3}	7.00×10^{-1}	4.09×10^{-1}	1.3125×10^{3}	6.97×10^{0}	1.92×10^{2}	11400	1.13
5A	6.254×10^{4}	1.3089×10^{3}	7.43×10^{-1}	1.370×10^{4}	1.3085×10^{3}	7.00×10^{-1}	3.53×10^{-1}	1.3090×10^{3}	1.31×10^{1}	3.00×10^{2}	18000	1.37

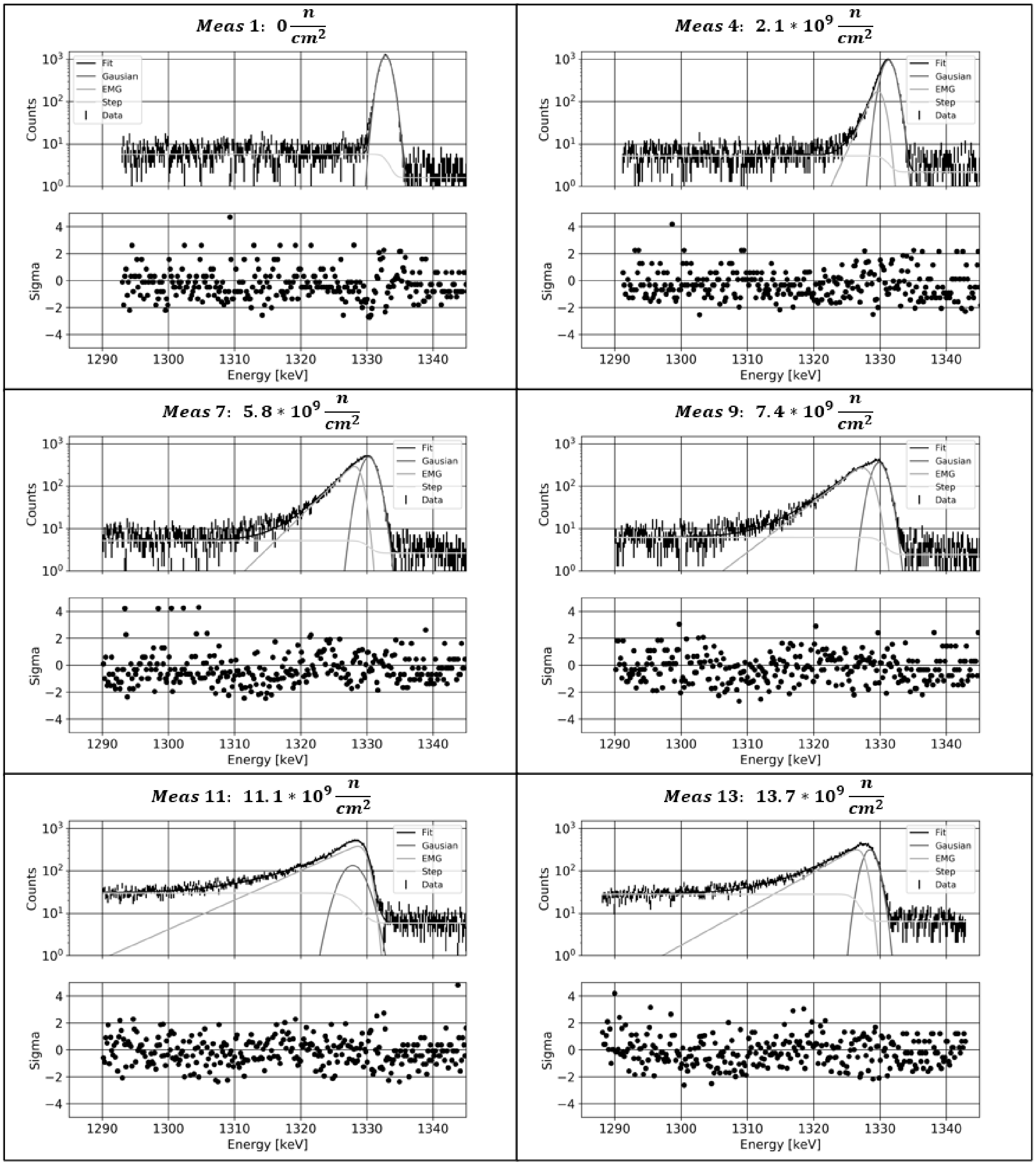

Figure D.1: *Radiation-damaged detector 1333 keV photopeak measurement with fits. Six photopeak measurements are shown that correspond to different exposures to fast neutron fluence. Each plot shows measured data (black markers), total fit function (black line), Gaussian component of the fit (dark gray line), EMG component of the fit (gray line), and the step function used to subtract background (light gray line). Fit residuals, or the ratio of the deviation between the fit and measured data to measurement error are shown below each photopeak.*